Fall 12-2019

Measurement of the production cross section of four top quarks in proton-proton collisions at 13 TeV

Caleb Fangmeier
University of Nebraska-Lincoln, cfangmeier2@huskers.unl.edu

MEASUREMENT OF THE PRODUCTION CROSS SECTION OF FOUR TOP QUARKS IN PROTON-PROTON COLLISIONS AT 13 TEV

by

Caleb Fangmeier

A DISSERTATION

Presented to the Faculty of

The Graduate College at the University of Nebraska

In Partial Fulfilment of Requirements

For the Degree of Doctor of Philosophy

Major: Physics and Astronomy

Under the Supervision of Frank Golf

Lincoln, Nebraska

December, 2019

MEASUREMENT OF THE PRODUCTION CROSS SECTION OF FOUR TOP QUARKS IN PROTON-PROTON COLLISIONS AT 13 TEV

Caleb Fangmeier, Ph.D.

University of Nebraska, 2019

Adviser: Professor Frank Golf

The field of particle physics involves not only searches for new particles and measurements of their interactions, but also the design and construction of advanced particle detectors.

This thesis presents the measurement of the production cross section of four top quarks in proton-proton collisions at a center-of-mass energy of 13 TeV using 137 fb^{-1} of integrated luminosity recorded by the CMS experiment at the LHC. This analysis considers events in the final state of a same-sign pair of leptons, notable for being a final state with relatively few Standard Model background events. A boosted decision tree is utilized to discriminate four top quark events from background events. The four top quark production cross section is measured to be $12.6^{+5.8}_{-5.2}$ fb, consistent with the Standard Model prediction. This measurement is used to constrain the top quark's Yukawa coupling as well as various theories beyond the Standard Model.

This thesis also describes the construction and testing of silicon pixel detector modules used in the Phase I upgrade of the CMS pixel detector, and optimization of electron reconstruction methods using the new detector. The role of automated module assembly and quality assurance will be discussed, as well as work towards the construction of a high precision silicon strip detector based telescope.

DEDICATION

For mom, who taught me to finish what I start.

ACKNOWLEDGMENTS

I would like to begin by recognizing my fellow grad students, especially Joaquin Siado Castaneda, Jose Monroy Montañez, Rami Kamalieddin, and Paulo Costa, without whose camaraderie and collaboration on coursework and research, I would have surely lost my mind at some point during the trials of grad school. I would also like to recognize current and past HEP faculty at UNL: Ken Bloom, Dan Claes, Aaron Dominguez, Frank Golf, Peisi Huang, Ilya Kravchenko, and Greg Snow, as well as the post-docs that helped make the Phase I upgrade project a success: Frank Meier and Rachel Bartek and the technicians in the electronics shop: Bob Kelty, Brian Farleigh, and Anatoly Miranov. Finally, I need to thank my family and friends, including the Slazoom Crew and our loyal listener, for their reliable support and efforts to keep me grounded.

Table of Contents

Chapter 1

Introduction

Humanity has long sought to understand more fully the nature of the world around it. This journey has led to an ever increasing knowledge of the constituents of matter and how these constituents interact, knowledge that has enabled engineers and inventors to create all of the tools and gadgets that define modern society. Particle physics exists at the frontier of our understanding of the universe and this thesis describes work to push that frontier just a little bit further.

The observation of the Higgs boson by the ATLAS and CMS experiments in 2012 was a tremendous discovery and achieved one of the primary goals of the Large Hadron Collider (LHC). However, since then searches at the LHC for particles predicted by the most promising theories beyond the Standard Model have ended with null results. This leaves physicists with questions about many unexplained phenomena. These questions include: Why is there so much more matter than antimatter in the universe? What is dark matter? Why are the fundamental particle masses what they are? Particle physics still does not have answers to these questions. Despite the recent dearth of discoveries, searches at collider experiments remain one of the best tools for discovering new phenomena. There are two obvious directions for collider physics to go in the future: higher energy, and more data. Creating beams of higher energy creates the conditions for the potential creation of more massive particles. It is possible that

there is a new particle whose discovery would blow the doors open on the study of new phenomena, and its mass is simply too large to create at our current particle colliders. This strategy has the obvious problems of technical challenge and cost since the maximum energy of a beam is limited by the diameter of the ring (making larger colliders financially challenging), and the strength of the bending magnets, which are limited by current magnet technology. The second approach is to collect more data at a lower energy. The precision of many measurements is limited by the amount of data collected. This is especially true for rare processes, such as the production of four top quarks. These rare processes are enhanced by many exotic theories, and the only way to rule out these theories is by collecting sufficient data to make accurate measurements of these rare processes.

To that end, experiments at the LHC regularly upgrade their detecting equipment to handle higher and higher rates of data collection. From roughly 2012 to 2016, the UNL Silicon Lab participated in one of these upgrades for the CMS pixel detector, and there is now ongoing work to aid in the design and construction of detectors that will be installed as part of the Phase II upgrade of CMS.

This thesis describes the measurement of the four top quark production cross section, but just as importantly, documents some of the technical work that goes into building modern particle detectors. Following this introduction, I will describe in Chapter 2 the current most accepted theory of particle physics, the Standard Model. Chapter 3 will describe the LHC and the Compact Muon Solenoid (CMS) detector. Chapter 4 contains the methods of event simulation and reconstruction that are employed in CMS, as well as my particular contribution to the reconstruction of electrons using the very detector assembled at UNL. Chapter 5 will discuss a measurement that was done of the $t\bar{t}t\bar{t}$ production cross section, as well as interpretations of that measurement. In chapter 6 I will present the Phase I CMS Pixel Detector Upgrade project, highlighting

my contributions to that work. Chapter 7 contains some closing remarks and an outlook for future work.

Chapter 2

Brief Review of the Standard Model

The Standard Model of Particle Physics (SM) stands as one of the most predictive and insightful scientific theories ever written. It is the culmination of a hundred years of intense theoretical exploration and experimental tests. It can successfully explain phenomena ranging from nuclear decay and the structure of atoms to the behavior of cosmic ray showers. Included in the theory are three fundamental forces. The first and most familiar is the electromagnetic force which is mediated by the photon in which all particles with electric charge participate. The second is the strong nuclear force. The strong force is mediated by the gluon which controls the interaction between all particles possessing color charge. It is this force that is responsible for binding quarks together into mesons and baryons, as well as binding protons and neutrons together into atomic nuclei. Finally, the weak nuclear force, which is mediated by the W and Z bosons, and is responsible for nuclear β-decay as well as more exotic processes such as interactions with the ghostly neutrino particle and the decay of the heavy flavor quarks.

Notably, the Standard Model is completely unable to explain why apples fall from trees or why the earth orbits the sun since it does not incorporate the gravitational force. The current most complete theory of gravity is General Relativity. However, despite large and ongoing efforts to unite General Relativity with the Standard Model,

no resulting theories have had the necessary self-consistency and predictive power to be accepted. Luckily for those working on collider experiments, the effect of gravity is so overwhelmed by the other three fundamental forces that it can be largely ignored. The constituent particles of the SM are shown in fig. 2.1.

2.1 Fundamental Particles

The *fermions* are characterized by their half-integer spin of $\frac{1}{2}\hbar$ and are split between the leptons and the quarks. They are fundamentally defined as Dirac spinor fields, ψ, which in the case of non-interacting massive particles are described by the Lagrangian

$$\mathcal{L} = \bar{\psi}\left(i\partial\!\!\!/ - m\right)\psi \tag{2.1}$$

in natural units, $\hbar = c = 1$. The $\partial\!\!\!/$ operator is defined as $\gamma^\mu\partial_\mu$ in Einstein notation where γ^μ are the 4x4 γ-matrices that satisfy the anti-commutation relations $\{\gamma^\mu, \gamma^\nu\} = 2\eta^{\mu\nu}$ and $\eta^{\mu\nu}$ is the Minkowski metric. Other fermions and interactions can be added to the theory with additional terms, as will be discussed in subsequent sections.

The leptons come in three generations with each generation having an electrically charged member and a neutral member. The charged members are the electron, muon, and tauon (or simply tau), while the neutral members are corresponding neutrinos. The electrically charged leptons participate in the electromagnetic and weak interactions, while the neutrinos only participate in the weak interaction. Another feature of the leptons is that while the charged leptons have non-trivial masses(m_e = 511 keV, m_μ = 106 MeV, m_τ = 1.78 GeV), the neutrinos are nearly massless. In fact, they were originally believed to be massless, until the observation of neutrino-mixing implied that at least two of them must have mass. The quarks also come in three generations with two members in each generation. In contrast with the leptons, however, the

quarks all carry electric charge. The "up-type" quarks carry charge $+2/3$ while the "down-type" quarks carry charge $-1/3$. The quarks are also *colored* which means that in addition to participating in the electromagnetic and weak interactions, they also interact via the strong nuclear force. Each of the six quarks has non-trivial mass, but they are wildly different, running from 2.4 MeV/c^2 for the up quark all the way to 171 GeV/c^2 for the top quark, the heaviest fundamental particle in the SM.

The remaining particles are the bosons: four force-mediators and the Higgs. These will be discussed in the following sections in context with their respective forces and contributions to the SM.

2.2 Quantum Electrodynamics

One of the early triumphs of quantum field theory (QFT) was the description of electromagnetism developed by Tomonaga[2], Schwinger[3], Feynman[4], and Dyson[5] and eventually coming to be known as quantum electrodynamics (QED). This theory describes the interaction of electrically charged particles with photons. In QED photons are described by a 4-vector field, A^μ, which is used to define the field strength tensor $F^{\mu\nu} = \partial^\mu A^\nu - \partial^\nu A^\mu$. This field, in the absence of charged particles, is governed by the Maxwell Lagrangian

$$\mathcal{L}_{\text{Max}} = -\frac{1}{4} F^{\mu\nu} F_{\mu\nu}$$

Interactions of the field with a fermion of charge q can be added to eq. 2.1, which gives

$$\mathcal{L}_{\text{Int}} = \bar{\psi} \left(i \not{D} - m \right) \psi + \text{h.c.}$$

where $\not{D} \equiv \gamma^\mu \left(\partial_\mu + i q A_\mu \right)$ and h.c. is just the hermitian conjugate of the previous

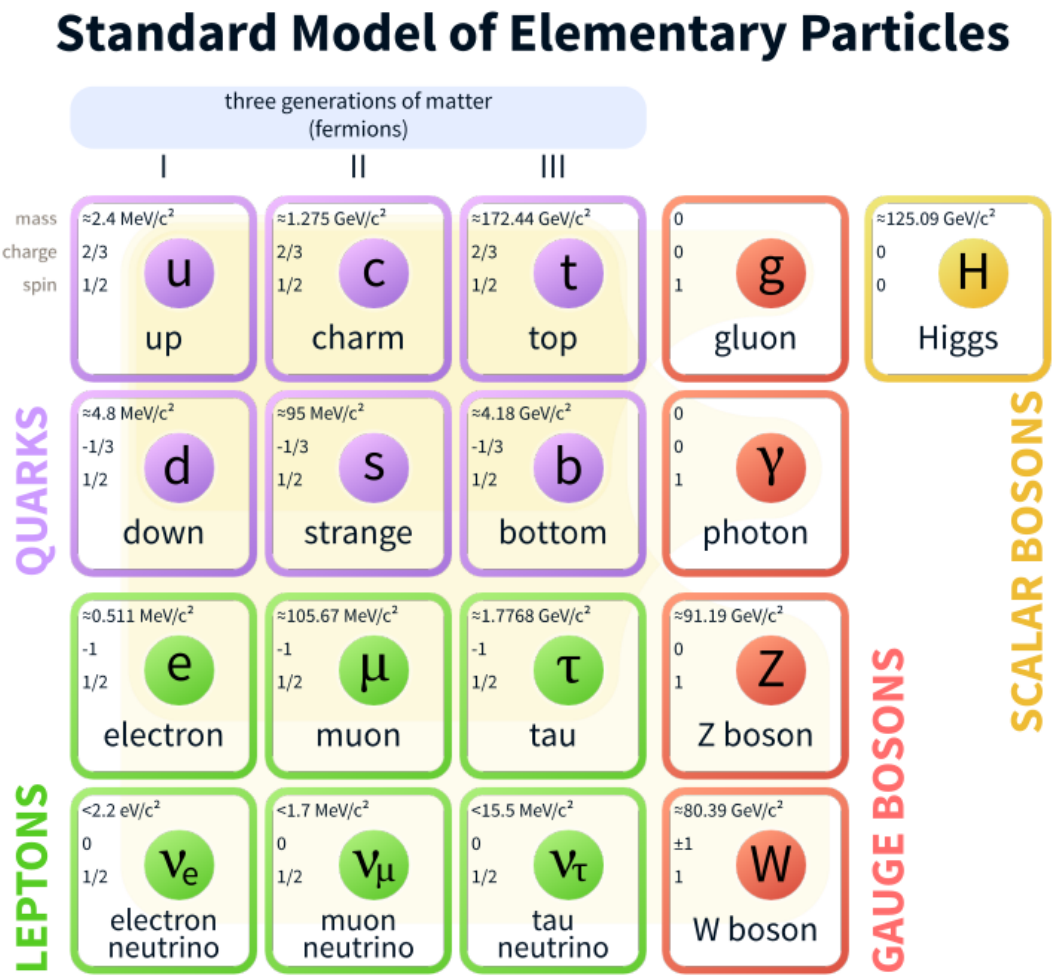

Figure 2.1: The particles of the SM.[1]

term. Putting these together yields the QED Lagrangian:

$$\mathcal{L}_{\text{QED}} = i\bar{\psi}\gamma^{\mu}\partial_{\mu}\psi - q\bar{\psi}\gamma^{\mu}A_{\mu}\psi - \frac{1}{4}F^{\mu\nu}F_{\mu\nu} - m_e\bar{\psi}\psi$$

QED is a gauge theory. This comes from the assumption that the observable is not the potential A^{μ}, but only the physical fields it defines, which leads one to ask what transformations can be applied to A^{μ} that leave these fields invariant. The transformations that possess this feature are called *gauge transformations*, and these

define symmetries of the theory. In the language of group theory, QED obeys $U(1)$ symmetry. The transformation associated with this symmetry that leaves $\mathcal{L}_{\text{QED}}$ unchanged is:

$$A^\mu \rightarrow A^\mu + \partial^\mu \chi, \psi \rightarrow e^{-iq\chi}\psi$$

where χ is a constant for a global gauge symmetry, but varies arbitrarily over space-time for a local gauge symmetry. The symmetries in the SM are local gauge symmetries.

Enforcing a local gauge symmetry upon a Lagrangian severely limits the form of the terms that can appear. For example, a mass term for the photon field of the form $m_\gamma A^\mu A_\mu$ is forbidden. This is acceptable in QED since the photon is massless, but will prove to be an issue for the massive bosons that come with the weak force, as will be discussed shortly.

2.2.1 Feynman Diagrams and Cross Sections

Observables in QFTs, especially in theories as complex as the SM, are rarely possible to calculate exactly using analytical methods. The solution to this issue is to look for approximate solutions of the field equations using small perturbations about the vacuum. This approach requires a small parameter to use in the perturbative expansion. For QED this is, in natural units, the positron charge $e = \sqrt{4\pi\alpha} \approx 0.3$. This perturbative expansion results in many terms, each of which can be represented graphically as a Feynman diagram. These are graphs that encode the interactions of particles in an intuitive way. A illustrative example is Compton scattering. In this process, a photon is incident on a charged fermion. Experimentally, this is normally an X-ray or gamma ray incident upon an electron in some atomic orbital. The electron absorbs the photon and then re-emits it with a smaller momentum (longer wavelength) than it started with. It is technically possible for the photon to be re-emitted with a

larger momentum, but this is referred to as anti-Compton scattering. In any case, the process can be represented by the two diagrams in fig. 2.2. There is a formalism for translating these diagrams into a precise calculation that can be performed analytically for simple cases, but often require the assistance of numerical methods. A description of the full formalism is beyond the scope of this discussion, but briefly:

- Each *vertex* in the graph contributes a factor proportional to the electromagnetic coupling constant, $\sqrt{4\pi\alpha}$.
- Photons and fermions contribute individual *propagators* that involve their momenta and, in the case of the fermions, their masses.
- Performing the calculation gives the *amplitude* of that diagram, which is a complex-valued function of the incoming and outgoing particles' momenta and spins. The next step is to add together the amplitudes of all of the diagrams under consideration, and then take the absolute square of the sum.
- The detectors used in collider experiments are typically not sensitive to spin and the beams, especially for hadron colliders, are not polarized, so an extra step involves averaging over the initial spin states and summing over the final spin states.

The precise rules are derived from the Lagrangian describing the system using the tools of QFT. The result of this full calculation is the *differential cross section*. This can be interpreted as a probability distribution where, given some initial state particles, it can predict the momentum distributions of the final state particles. Integrating the differential cross section over all initial and final states gives the *total cross section*, or just *cross section*. The diagrams of fig. 2.2 are just the two *leading order* (LO) diagrams, meaning that of all possible diagrams, these have the smallest possible number of vertices. Since each vertex contributes additional factors of the coupling

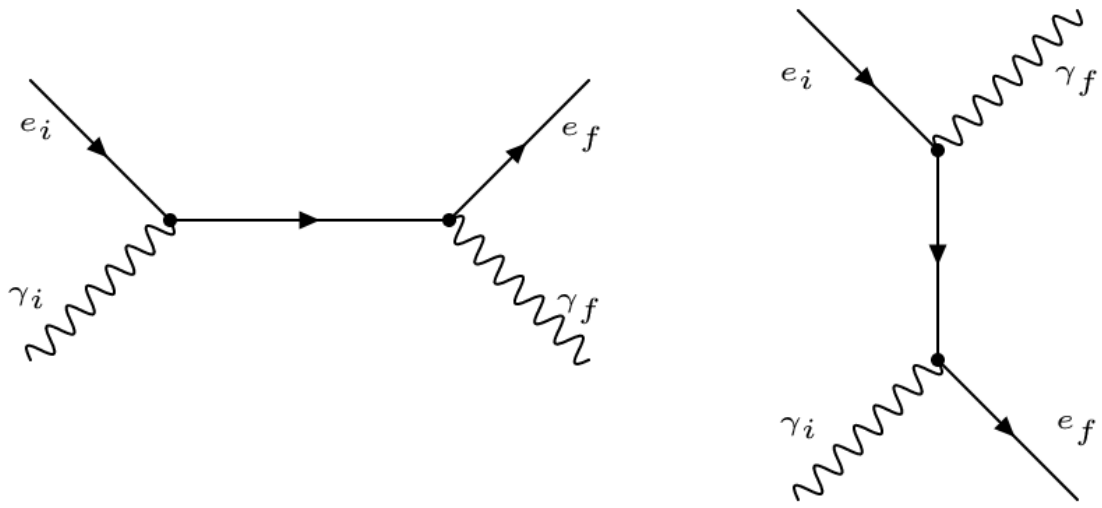

Figure 2.2: Leading order Feynman diagrams for Compton scattering. The topology of the left diagram is conventionally referred to as "s-channel" while the right's is called "t-channel". Initial particles are on the left of each diagram, and final state particles are on the right.

constant $g_e \equiv \sqrt{4\pi\alpha}$, diagrams with additional vertices give smaller and smaller individual contributions to the total cross section. However, the issue is complicated by the fact that the total number of diagrams at each order of g_e increases, and the manner of interference between the diagrams is often not clear without doing the full calculation. This is why precise predictions require the explicit inclusion of more complicated diagrams. The set of diagrams that include the next fewest number of vertices are referred to as *next-to-leading order* (NLO), and beyond that are the *next-to-next-to-leading order* (NNLO) diagrams which are sometimes included for very precise calculations. The order to which calculations are performed is generally motivated by the related experimental precision. NLO calculations are most often satisfactory for collider based measurements.

The cross section of any particular process depends upon the conditions facilitating that process. In hadron colliders, the (anti)protons that are collided are composite

particles with three valence quarks as well as "sea" quarks and gluons that are continuously created and annihilated. When a high energy collision occurs, it is best understood as an interaction not between two protons, but of two of these constituent particles, or *partons*. Each of these partons carries a fraction of the proton's total energy, however this fraction is random and its probability distribution is different for each type of particle. These probability distributions are called the hadron's *parton distribution functions* (PDFs). Fig. 2.3 shows the PDFs for protons at different momentum transfer scales.

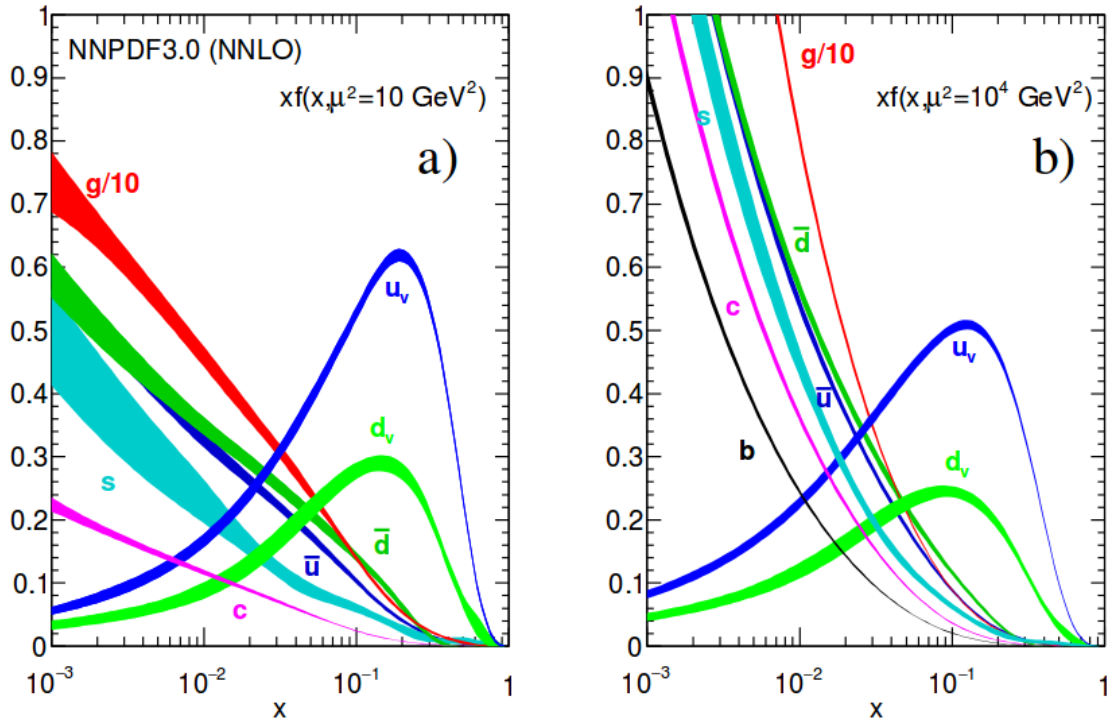

Figure 2.3: Parton distribution functions for two values of momentum transfer, μ. The u_v and d_v refer to the proton's valence up and down quarks. Other quark flavors exist through the temporary splitting of gluons into quark-antiquark pairs.[6]

2.3 Quantum Chromodynamics

The theory describing the interaction of particles with color charge is quantum chromodynamics (QCD). The colored fermions, quarks, were first proposed by Gell-Mann[7] and Zweig[8] in 1964 to aid in the classification of hadrons, and were first observed four years later at SLAC[9]. In contrast with QED, QCD obeys the non-Abelian SU(3) symmetry, and just as A^μ was used to define a field strength tensor in QED, the eight *gluon* fields each define their field strength tensor as

$$G^a_{\mu\nu} = \partial_\mu G^a_\nu - \partial_\nu G^a_\mu - g_s f_{abc} G^b_\mu G^c_\nu$$

where g_s is the strong coupling constant and the f_{abc} are the structure constants of the symmetry group defined by the commutation relations

$$\left[\frac{\lambda_a}{2}, \frac{\lambda_b}{2}\right] = i f_{abc} \frac{\lambda_c}{2}$$

where λ_a are the Gell-Mann matrices. The quarks, similar to the fermions in QED, are represented as spinor fields governed by the Lagrangian

$$\mathcal{L}_q = \bar{q_f} \left(i\gamma^\mu \partial_\mu - m\right) q_f$$

for a single quark. In $\mathcal{L}_q$, $q_f = (\psi_1, \psi_2, \psi_3)$ where each ψ represents a color component and there is an implied sum over all three. Interactions between the quarks and the gluons are introduced by adding the covariant derivative D_μ into $\mathcal{L}_q$ in place of ∂_μ where

$$D_\mu = \partial_\mu + i g_s \frac{\lambda_a}{2} G^a_\mu.$$

Doing this yields the QCD Lagrangian.

$$\mathcal{L}_{\text{QCD}} = \sum_f \bar{q}_f \left(i\gamma^\mu \partial_\mu - m\right) q_f - \frac{1}{4} G_a^{\mu\nu} G^a_{mu\nu} - g_s \bar{q}_f \gamma^\mu \frac{\lambda_a}{2} q_f G^1_\mu$$

Coupling constants are generally only constant at a particular energy scale. Considering more or less energetic processes can affect the coupling constant. This effect is described by the interaction's beta function, $\beta(\alpha) = \partial\alpha / \partial \log(\mu)$ where μ is some energy scale. The beta function for QCD in the Standard Model is

$$\beta(\alpha_s) = -\frac{7\alpha_s^2}{2\pi}$$

where $\alpha_s \equiv g_s^2/4\pi$. The fact that the beta function is negative implies that the coupling decreases with energy scale, or equivalently, increases with larger length scales. This leads to the property of asymptotic freedom, which simply refers to the shrinking coupling as interaction length scales shorten. The coupling constant being small at high energies also means that one can successfully apply perturbation theory as one would in QED in that context. However, at low energies, such as those of most bound states, perturbative approaches fail and other approaches, such as *Lattice QCD* are applied instead. Quarks and gluons are also subject to color confinement, which means that any observable particle must be color neutral, and since individual quarks and gluons carry color charge they cannot be observed in isolation. Instead, this color neutrality is achieved through collections of these particles that together possess equal quantities of the three colors, conventionally called red, blue, and green. Such is the case for *baryons*, with three quarks carrying one of each color charge. Color neutrality can also be achieved via a quark-antiquark pair possessing the same color, e.g. a green quark and an green anti-quark together make up a colorless *meson*.

Colorless combinations of more than three quarks are theoretically possible, but not normally encountered. Colorless pairings of gluons, or *glueballs*, are also possible in theory, but have not been observed experimentally.

A consequence of these properties is the hadronization and fragmentation of high energy quarks and gluons into *jets*. Fragmentation is the process by which an energetic quark or gluon, generally resulting from a hard collision, radiates a cascade of less energetic particles, and hadronization is the process where these particles become bound together into a jet of hadrons. However, this process does not occur for the top quark for reasons that will be explored in the next section.

2.4 The Electroweak Interaction

In 1934, Fermi proposed an explanation for nuclear beta decay, $n \rightarrow pe^{-}\bar{\nu_e}$[10]. The explanation involved a new interaction that would come to be identified as the weak nuclear force. This was initially proposed to be a direct interaction involving all incoming and outgoing particles sharing a single vertex. However, over the next few decades experiments at higher energies would show that this was just a low energy approximation. In reality this process is mediated by a new force mediator, the W boson. The W boson is one of the mediating bosons of the weak force, a new fundamental interaction with a peculiar feature, parity violation.

In 1956 Yang and Lee suggested that parity is not conserved in weak interactions, based on their examination of kaon decays[11]. The next year, this was confirmed in studies of nuclear beta decays by Wu[12]. Conservation of parity, roughly speaking, means that physical systems that are unchanged by a reflection about some plane will continue to remain unchanged by the reflection as the system evolves. This property holds for QED and QCD, but not for weak interactions.

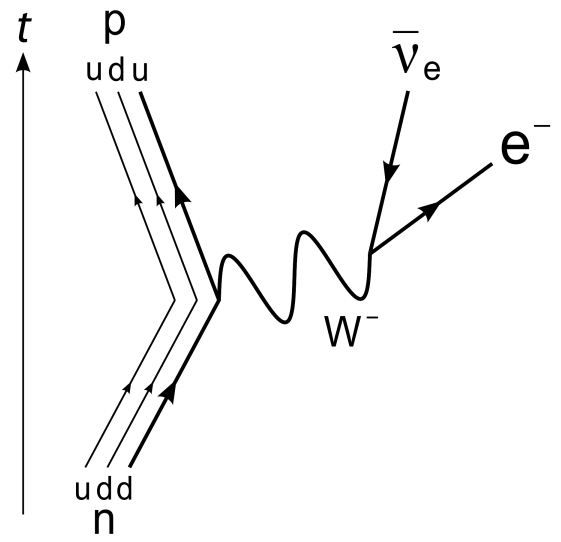

Figure 2.4: Leading order Feynman diagram for nuclear β decay

Fundamentally, this follows from the fact that the weak force acts differently on particles of different *chiralities*. Chirality is a Lorentz invariant quantity that corresponds to eigenvalues of the operator $\gamma^5 = i\gamma^0\gamma^1\gamma^2\gamma^3$. Any field can be divided into chiral states with eigenvalues of +1, known as right-handed, and -1, known as left-handed. Chirality is related to the more familiar quantity of *helicity*. Helicity is the projection of a particle's spin along the direction of its momentum. Helicity, however, is not a Lorentz invariant quantity because a change of reference frame, or *boost*, can reverse the direction of the momentum, and with it the sign of the helicity. However, for massless particles one cannot reverse the momentum with a boost and the helicity and chirality are equivalent.

In the 1960's, work by Glashow[13], Salam, Ward[14], and Weinberg[15] showed that within the unified framework of their *electroweak* theory, a new spin-1 electrically charged particle should exist to mediate the weak force. This new particle, the W boson, was discovered at CERN in 1983 by the UA1[16] and UA2[17] experiments. Its mass is currently measured to be $M_W = 80.379 \pm 0.012$ GeV/c^2[18]. The fields

associated with the W boson, $W_\mu^\pm$ couple only to the left components of fermion fields, implying that only left-handed particles and right-handed anti-particles can interact with the $W^\pm$ bosons. The symmetry group obeyed by this electroweak theory that generates these properties is $SU(2)_L \otimes U(1)_Y$.

The weak interaction does not directly couple to the fermions in their mass eigenstates, but rather superpositions of them. This mixing is described by the CKM (Cabibbo-Kobayashi-Maskawa) matrix for quarks and the PMNS (Pontecorvo-Maki-Nakagawa-Sakata) matrix for the leptons. The top quark, in particular, due to being heavier than the W boson, can decay weakly to an on-shell[1] W boson and a bottom quark. This process happens on the timescale of 10^{-25} s which is smaller than the timescale necessary for top-flavored hadrons or $t\bar{t}$-quarkonium bound states to form[19]. In addition, because $|V_{tb}| \gg |V_{ts}|, |V_{td}|$ in the CKM matrix, the top quark will predominantly decay into a W with a bottom quark, rather than with a strange or down quark.

The bottom quark will fragment and form a bottom-flavored hadron. Because the bottom quark's transition rate to lower mass quarks is relatively small, it will typically survive long enough to travel a few millimeters before decaying and forming a jet with its origin displaced relative to the primary interaction. The W will immediately decay into either a pair of quarks, resulting in two jets, or a charged lepton and a neutrino.

The electroweak theory also predicts the existence of an electrically neutral spin-1 particle. This particle, called the Z boson, was also observed by the UA1[20] and UA2[21] experiments at CERN, and its mass is currently measured to be 91.1876 ± 0.0021[18].

[1] A particle is allowed to exist virtually (as an interior line in a Feynman diagram) with a "mass" different from its normal mass. Such particles are said to be *off-shell*, while particles which are created at their normal mass are *on-shell*. All observable particles are on-shell.

2.5 Electroweak symmetry breaking and the Higgs field

As mentioned previously, massive bosons are incompatible with local gauge invariance, which is clearly at odds with the observation of the W and Z bosons. A potential solution to this was proposed by Higgs[22], Brout, Englert[23], and Guralnik, Hagen, and Kibble[24] in 1964. Their solution was to employ the concept of *spontaneous symmetry breaking*.

The solution begins by introducing a doublet of complex scalar fields, known as the Higgs field.

$$\phi = \begin{pmatrix} \phi^+ \\ \phi^0 \end{pmatrix} = \begin{pmatrix} \frac{1}{\sqrt{2}}\left(\phi_1 + i\phi_2\right) \\ \frac{1}{\sqrt{2}}\left(\phi_3 + i\phi_4\right) \end{pmatrix}$$

Here, the ϕ_i's are real scalar fields. The Lagrangian that governs the evolution of these fields is

$$\mathcal{L}_\phi = \left(D_\mu \phi\right)^\dagger \left(D^\mu \phi\right) - V\left(\phi\right)$$

where the covariant derivative D_μ is here defined as

$$D_\mu = \partial_\mu + i g_w W_\mu^i \frac{\sigma_i}{2} + i g_Y B_\mu \frac{Y}{2}$$

and the potential, $V\left(\phi\right)$ is

$$V\left(\phi\right) = \mu^2 \phi^\dagger \phi + \lambda |\phi|^2, \left(\mu^2 < 0, \lambda > 0\right)$$

In the above equations, B_μ, and W_i are the original electroweak fields, from which the photon, W, and Z boson fields are composed, and g_Y is the coupling constant associated with the weak hypercharge. The weak hypercharge is related to the electric

charge, q, and the third component of the weak isospin via $Y = 2(q - I_z)$. The parameters μ and λ are free parameters that characterize the Higgs field.

Critically, because $\mu^2 < 0$ the ground state is not at $\phi = 0$, but instead has to satisfy $|\phi|^2 = -\frac{\mu^2}{2\lambda} \equiv \frac{v^2}{2}$. This is satisfied by an infinite number of ground states. Picking one breaks the $SU(2)_L \otimes U(1)_Y$ symmetry obeyed by the original Lagrangian, $\mathcal{L}_\phi$. Fig. 2.5 shows an analogue of this symmetry breaking in a familiar mechanical system. The particular ground state can be chosen freely, but a convenient choice is

$$\phi_{gnd} = \begin{pmatrix} 0 \\ \frac{v}{\sqrt{2}} \end{pmatrix}$$

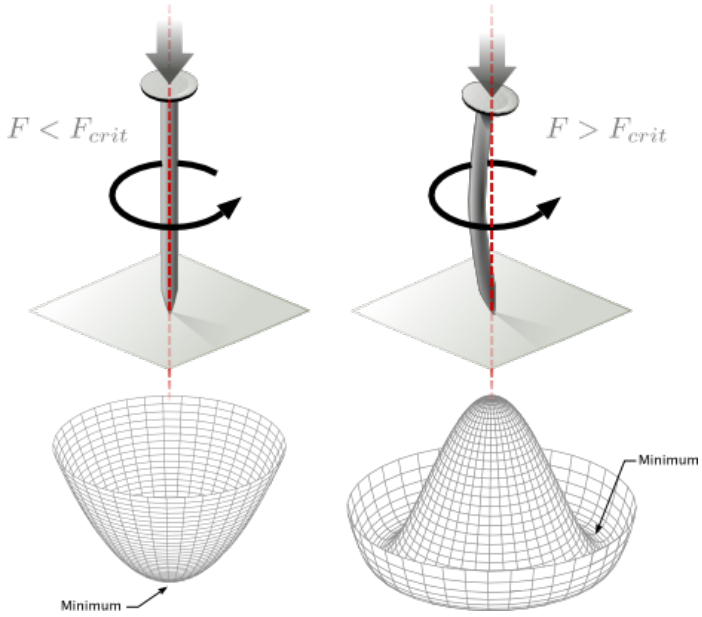

Figure 2.5: Illustration of the spontaneous symmetry breaking mechanism. The nail, when subjected to a small force, keeps its rotational symmetry, but if the force grows too large it buckles under the strain. The *spontaneous* bend in the nail has broken rotational symmetry. This can also be understood in terms of the nail finding its potential minimum, a minimum that shifts from a single point to a circular collection of points as the force passes its critical value.[25]

Combining $\mathcal{L}_\phi$ with the symmetry-broken electroweak Lagrangian and performing

some simplification, we are left with:

$$
\begin{aligned}
\mathcal{L} =& \frac{1}{2}\partial_\mu h \partial^\mu h - |\mu|^2 h^2 \\
& -\frac{1}{2}\left(W^-_{\mu\nu}\right)^\dagger W^{-\mu\nu} + \frac{1}{2}\left(\frac{g_w v}{2}\right)^2 \left(W^-_\mu\right)^\dagger W^{-\mu} \\
& -\frac{1}{4}\left(W^+_{\mu\nu}\right)^\dagger W^{+\mu\nu} + \frac{1}{2}\left(\frac{g_w v}{2}\right)^2 \left(W^+\mu^-\right)^\dagger W^{+\mu} \\
& -\frac{1}{4} Z_{\mu\nu} Z^{\mu\nu} + \frac{1}{2}\left(\frac{g_w v}{2\cos\theta_W}\right)^2 Z_\mu Z^\mu \\
& -\frac{1}{4} A_{\mu\nu} A^{\mu\nu} \\
& +\frac{g_w^2 v}{2} h W^-_\mu W^{+\mu} + \frac{g_w^2}{4} h^2 W^-_\mu W^{+\mu} + \frac{g_w^2 v}{4\cos^2\theta_W} h Z_\mu Z^\mu + \frac{g_w^2}{8\cos^2\theta_W} h^2 Z_\mu Z^\mu \\
& +\frac{\mu^2}{v} h^3 + \frac{\mu^2}{4v^2} h^4
\end{aligned}
$$

In the above equation, $V_{\mu\nu} \equiv \partial_\mu V_\nu - \partial_\nu V_\mu$ for the W and Z vector bosons. This is best understood by looking through the terms line by line. The first line describes a spin-0 field, h, associated with a particle of mass $m_h = \sqrt{2}|\mu|$. This particle is the *Higgs boson*.

Lines 2-4 describe the spin-1 fields $W^\pm_\mu$ and Z_μ. These fields are associated with the *massive* W and Z bosons that have been previously discussed. Their masses are related to fundamental constants as

$$
m_{W^\pm} = \frac{g_w v}{2} \quad \text{and} \quad m_Z = \frac{m_{W^\pm}}{\cos\theta_W}
$$

where θ_W is the Weinberg angle or *weak mixing angle*. It defines the spontaneous symmetry breaking angle that rotates the original neutral fields to obtain the Z boson and the photon. It is also relates the coupling strengths of the two electroweak sub-interactions

$$e = g_w \sin\theta_W = g_Y \cos\theta_W$$

Line 5 describes the massless spin-1 field associated with the photon. Line 6 encapsulates the interaction between the vector bosons and the Higgs, and finally line 7 describes the Higgs self-interaction.

The Higgs mechanism itself only directly accounts for the masses of the vector bosons. While a significant victory, the masses of the fermions are still not included in the theory. This can be remedied by introducing *Yukawa* couplings between the fermions and the Higgs field. After spontaneous symmetry breaking, these contributions take the form

$$\mathcal{L}_{\text{yukawa}} = \sum -m_f \bar{\psi}\psi - \frac{m_f}{v}\bar{\psi}\psi h$$

The masses in the above equation are related to the Yukawa coupling which is unique for each particle and represents how strongly that particle interacts with the Higgs field. This relation is simply

$$m_f = \frac{y_f}{2} v.$$

For most fermions, this coupling, y_f, is very small. For electrons it is roughly 2×10^{-6}, for example. However, the top quark is unique in that its Yukawa coupling, y_t, is ~1 in the SM. This makes processes that involve interactions between the top quark and the Higgs boson interesting candidates for studying Higgs physics. In particular, the production cross section of four top quarks depends upon the value of the top Yukawa coupling. This is explored more deeply in chapter 5.

Chapter 3

The LHC and CMS Detector

Lying buried beneath Geneve, Switzerland and stretching across the border into France is the largest machine ever constructed by mankind. This marvel of physics and engineering is operated by CERN, the European Organization for Nuclear Research[1]. This machine, the Large Hadron Collider is a circular particle accelerator with a circumference of 28 km that is capable of creating proton-proton collisions with up to 13 TeV of energy in the center-of-mass frame. CERN itself is a huge organization, comprising roughly thirteen thousand people with diverse backgrounds and disciplines. The goal of the LHC and associated experiments is to increase humanity's fundamental understanding of the nature of the Universe. It accomplishes this by studying the unique properties of matter in the extreme conditions created in very high energy particle collisions. These properties are examined by analyzing the data collected by sophisticated particle detectors at several designated points around the LHC ring. The detectors are marvels unto themselves, often designed and operated by collaborations of thousands of physicists and engineers from across the world. The principle detectors on the LHC ring are ALICE, ATLAS, CMS, and LHCb. ATLAS and CMS are general purpose detectors, facilitating a wide range of physics measurements. ALICE specializes in exploring the physics of heavy-ion collisions, exploring the dynamics of

[1]Acronym derived from the original French: *"Conseil Européen pour la Recherche Nucléaire"*

the quark-gluon plasma created during collisions of lead or gold ions. LHCb is another specialized detector that focuses on phenomena related to the bottom quark.

3.1 The LHC

After initial setbacks in 2008[26], the LHC began supplying collisions for physics research in 2010 with collision energies of 7 TeV. It operated successfully over the next few years, delivering sufficient high energy collisions to allow for the joint discovery in 2012 by CMS and ATLAS of a new particle with a mass of 125 GeV identified as the Higgs boson[27, 28], as well as a multitude of measurements of SM processes and exclusions of vast swaths of BSM theories. It then underwent an upgrade to increase the center-of-mass energy to 13 TeV, and went on to successfully deliver collisions to CMS over a span of three years from 2016 to 2018.

The LHC complex is shown in fig. 3.1. Before entering the LHC, protons are collected, bunched, accelerated by several steps. The protons originate as hydrogen atoms that have been ionized by a strong electric field. The H^+ ions (i.e. protons) are then accelerated to 50 MeV by the LINAC2 linear accelerator. They are then transferred to the Proton Synchrotron (PS) which further accelerates the protons to 26 GeV. Next, they are injected into the Super Proton Synchrotron (SPS) which pushes their energy to 450 GeV before finally entering the LHC and being pushed to 6.5 TeV. There are two separate injection pathways for injecting protons into the clockwise and the counterclockwise beam channels.

The acceleration of the protons is done with superconducting radio-frequency (RF) cavities (fig. 3.2). The LHC has a system of 16 of these cavities concentrated at a single location along the ring. To bend the proton beam around the LHC ring, superconducting dipole magnets are used. Fig. 3.3 demonstrates how these magnets

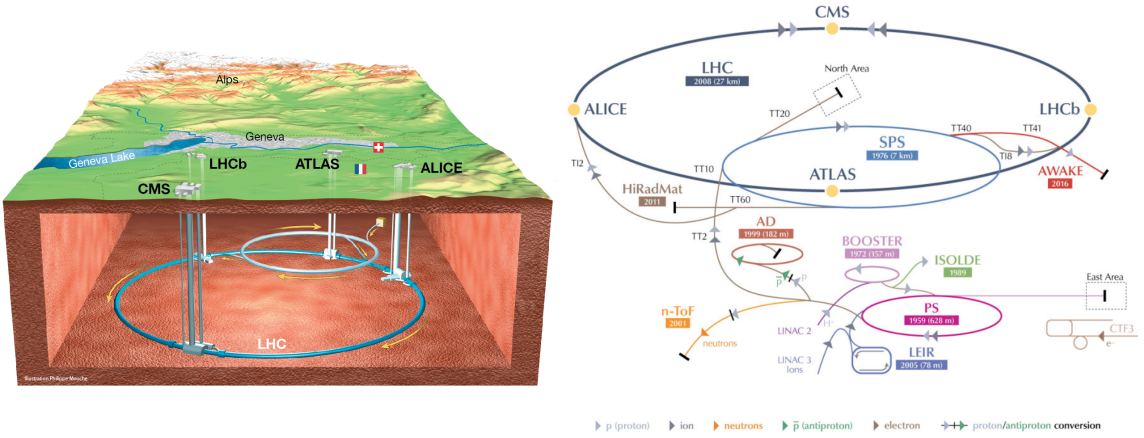

Figure 3.1: Left: Overview of the LHC.[29]. Right: Schematic of the LHC Complex.[30]

act to steer the beam. The LHC has 1232 such magnets distributed around eight curved sections of the ring, the curved sections being 2.45 km long each and separated by 545 m long straight sections containing the RF acceleration system, beam dump, and detector halls.

The beams of protons are not continuous, but are grouped into *bunches* of roughly 100 billion protons each. Each bunch has a transverse diameter of roughly 1 mm and is approximately 7.5 cm long. The bunches of protons will inevitably have some spread in momentum transverse to the beam direction, exacerbated by the repulsive Coulomb force amongst the protons in each bunch. To account for this, sextupole magnets are employed to condition the beam. As the beam approaches each of the interaction points, quadrupole magnets are used to focus the beam down to having a width of just 16 μm in order to increase the average number of collisions as the opposing beams cross. The number of interactions that occur during each bunch-crossing is tuned to balance maximizing the total number of collisions with what the detector can effectively handle. If there are too many simultaneous interactions in a single bunch crossing, the detector's electronics are at risk of buffer overflows, leading to data loss.

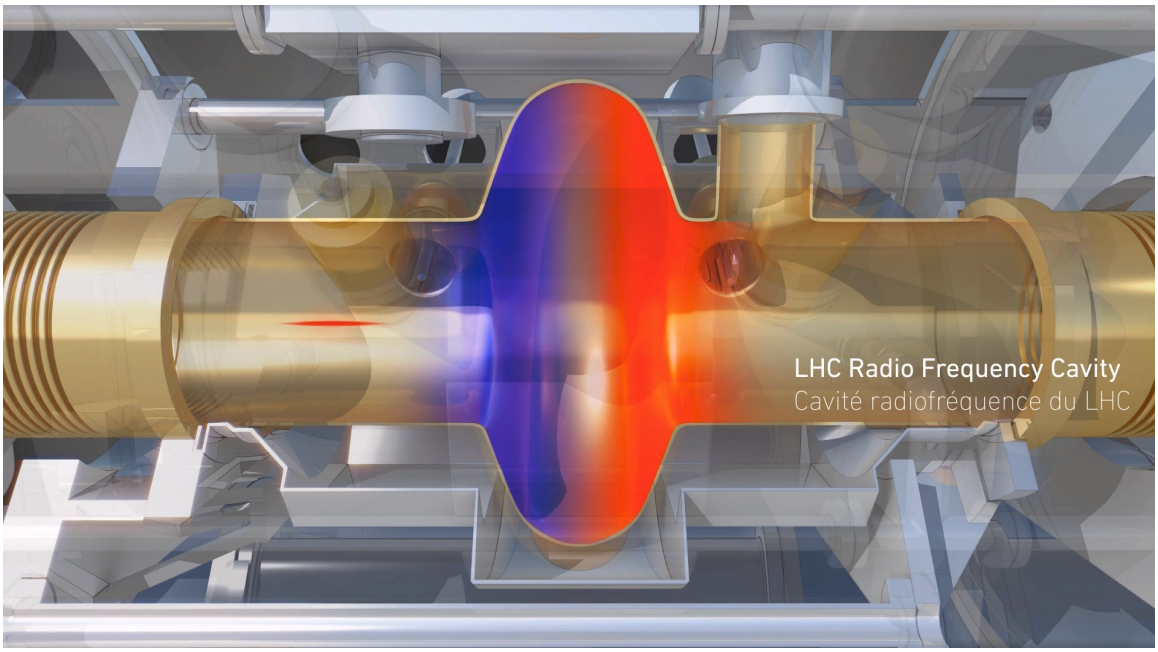

Figure 3.2: Diagram of an LHC RF cavity[31]. The blue shade shows a deceleration zone and the orange an acceleration zone. Bunches of protons(red) travel through this from left to right. The electric field inside the cavity is pulsed in time with the beam such that the field magnitude is small when a proton bunch enters, avoiding deceleration, but becomes large as the bunch is exiting, thus accelerating the bunch. The LHC RF cavities are tuned to oscillate at 400 MHz, and are operated in a superconducting state at 4.5 K.

It also increases, potentially dramatically, the amount of computing resources that are required to reconstruct each event. The reconstruction of charged particle paths through the detector, or tracks, in particular can become prohibitively expensive as the number of interactions grows. The *instantaneous luminosity*, directly related to the number of interactions per bunch-crossing, can be calculated using

$$L = fn\frac{N^2}{4\pi\sigma^2} \tag{3.1}$$

In the above equation, f is the orbit frequency of bunches around the LHC ring, n is the number of bunches per beam. So, $2fn$ is effectively the bunch-crossing

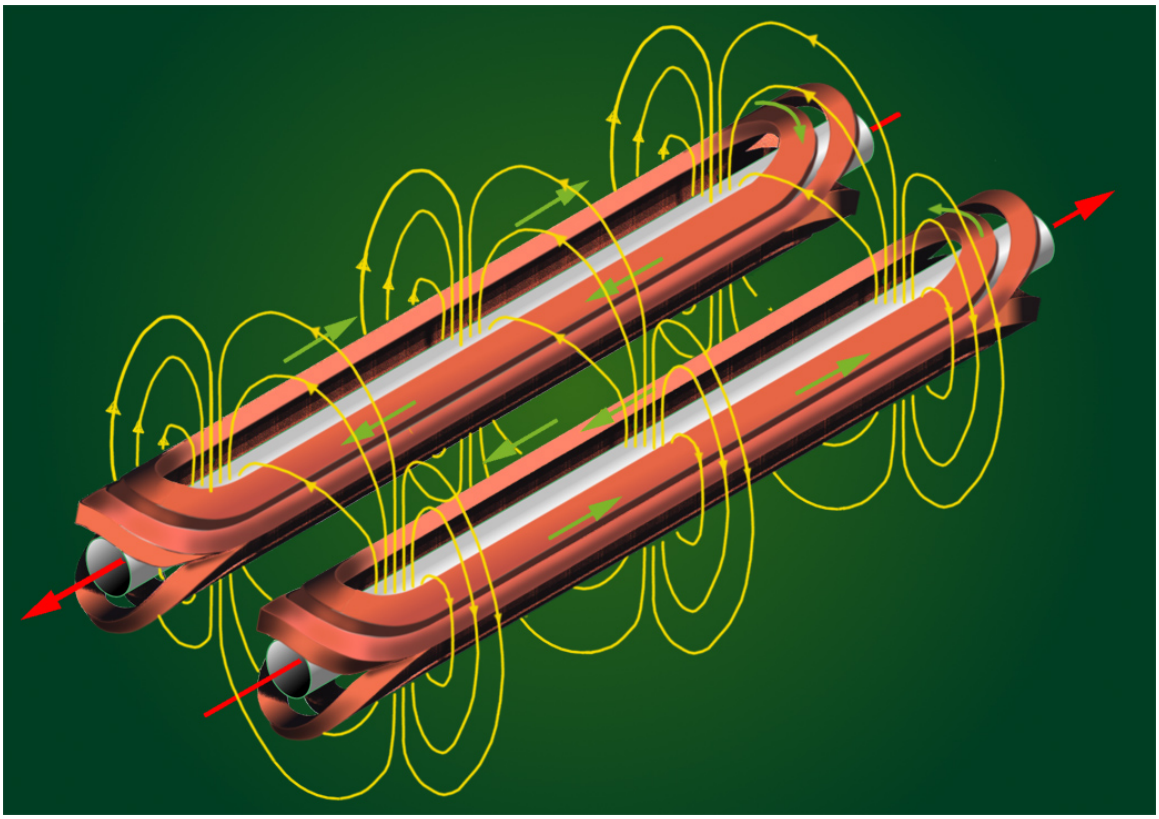

Figure 3.3: Visualization of the dipole magnetic field used to curve the beam at the LHC[32]. Note how the field lines pass through each beam in opposite directions, causing each beam to bend towards the LHC center.

frequency[2]. N is the number of protons per bunch and σ is the Gaussian width of the beam, assuming the beam is cylindrically symmetric. In 2018, CMS would typically receive peak instantaneous luminosities of roughly 20 nb^{-1}/s[33]. Integrating the instantaneous luminosity against time yields, unsurprisingly, the *integrated luminosity*. This, together with the collision energy, largely dictate what sort of physics one can expect to study at a collider experiment. The integrated luminosity delivered and recorded by CMS in 2018 is shown in fig. 3.4.

[2]Twice fn due to two beams orbiting in opposite directions.

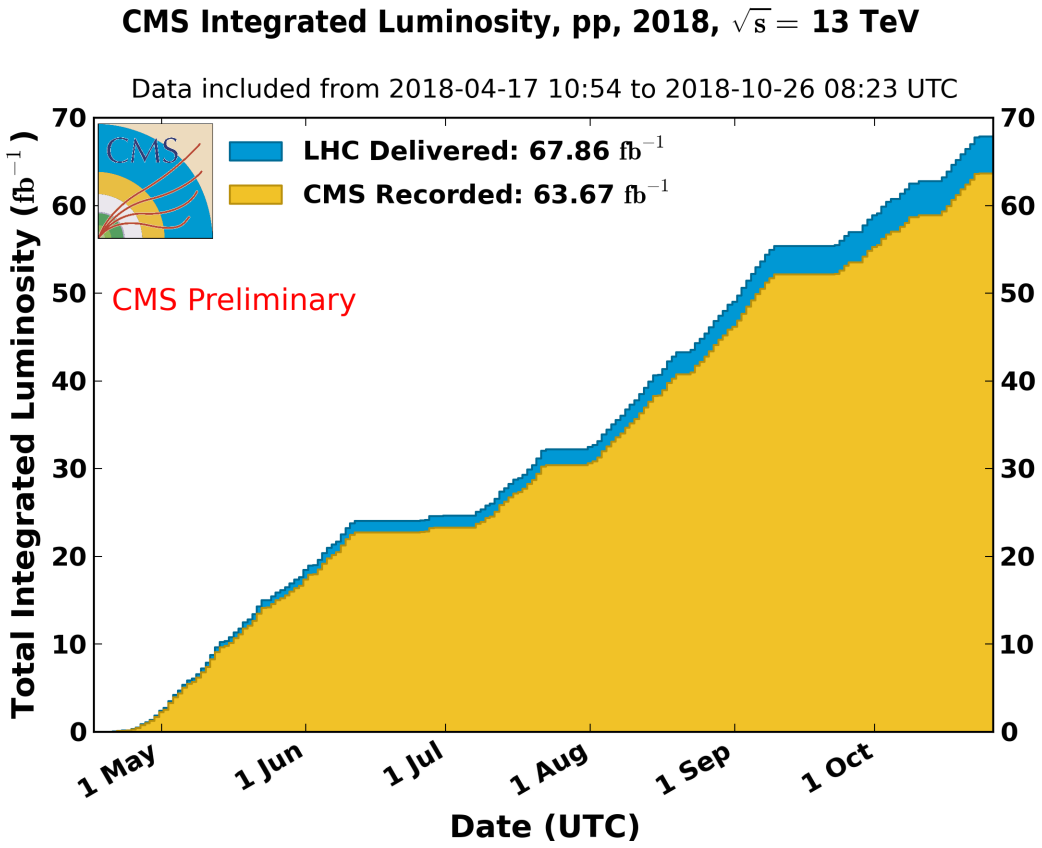

Figure 3.4: The CMS Integrated luminosity for 2018[33].

3.2 The CMS Detector

Of the several sophisticated detectors arrayed around the LHC ring, this thesis focuses on the Compact Muon Solenoid (CMS) detector. CMS is composed of several subdetector systems:

- Silicon trackers
- Crystal electromagnetic calorimeter (ECAL) and preshower detector
- Hadron calorimeter (HCAL)
- Superconducting solenoid magnet
- Muon chambers

Fig. 3.5 shows how these subdetectors are assembled together, and each of these will be discussed in the following sections.

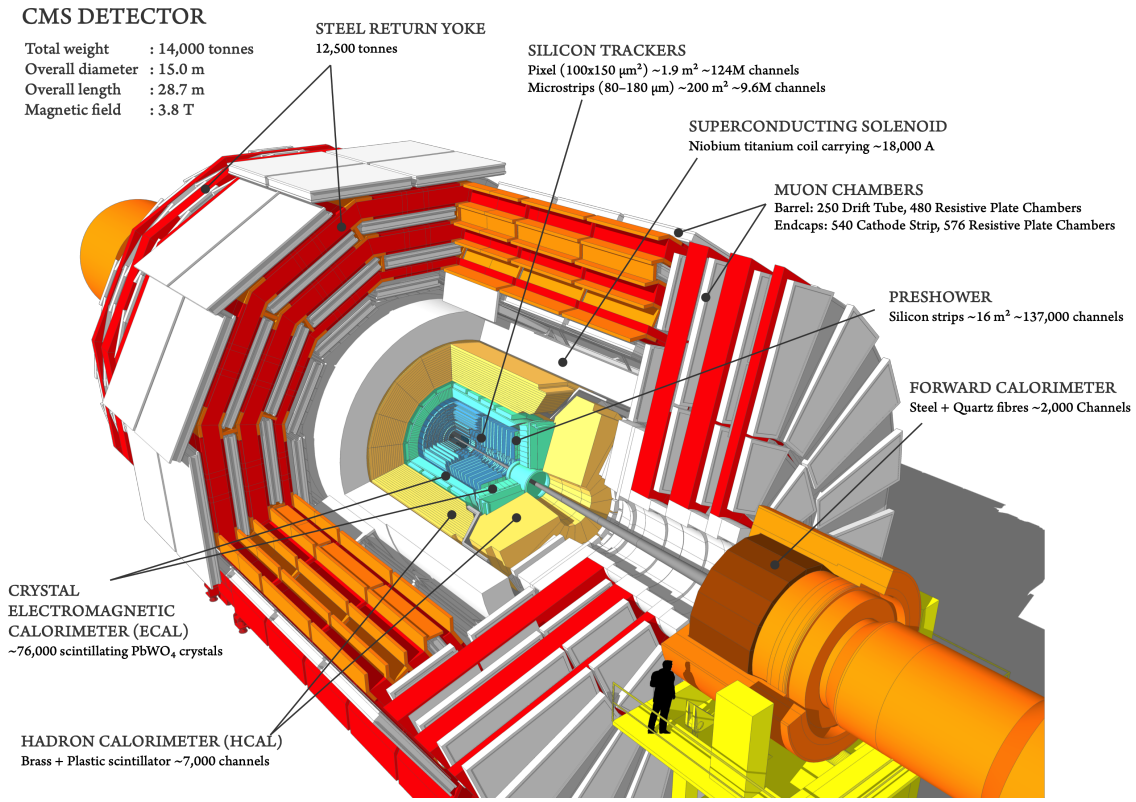

Figure 3.5: Cutout view of the CMS detector. Note the nested design with a distinct cylindrical "barrel" region and two planar endcap or "forward" regions.

The CMS coordinate system (fig. 3.6) has its origin at the geometrical center of the detector. The Cartesian ordinals are:

- *x-axis*: pointing toward center of LHC ring
- *y-axis*: pointing vertically upward
- *z-axis*: pointing along the beam axis

A cylindrical coordinate system is also commonly used due to the overall cylindrical geometry of the detector. It uses the standard cylindrical definitions, $R = \sqrt{x^2 + y^2}, \phi = \tan^{-1} \frac{y}{x}$.

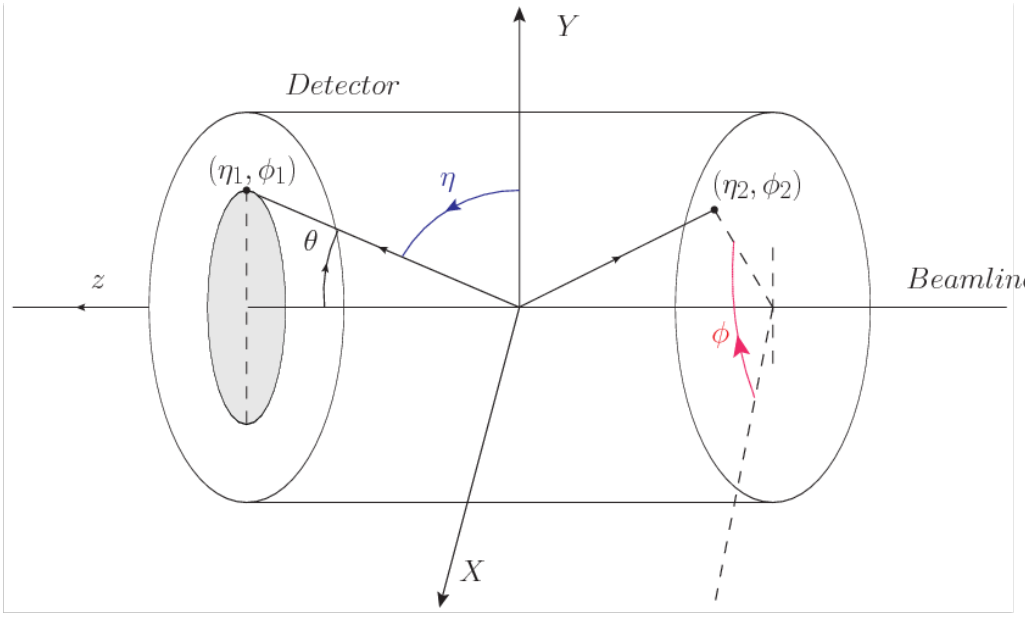

Figure 3.6: CMS detector coordinate system.

Other useful quantities in hadron colliders are the kinematic quantity known as rapidity, y, and a related geometrical quantity, pseudorapidity, η.

$$y = \frac{1}{2}\ln\frac{E + p_z}{E - p_z} \quad \eta = -\ln\left(\frac{\theta}{2}\right)$$

Rapidity is a useful observable because it is Lorentz invariant for boosts along the beam axis, meaning that it is not dependent upon the particular rest frame of the two interacting partons in the event. However, rapidity is difficult to measure so the alternative, purely geometric quantity, pseudorapidity is used which approximates the rapidity as

$$y \approx \eta - \frac{p_L}{2|\mathbf{p}|}\left(\frac{m}{p_T}\right)^2$$

In the ultra-relativistic limit $\left(\frac{m}{p_T} \to 0\right)$ or for massless particles the approximation becomes exact.

Finally, the azimuthal angle, ϕ, and the pseudorapidity are used to define the angular separation between particles as

$$\Delta R = \sqrt{(\Delta\phi)^2 + (\Delta\eta)^2}$$

3.2.1 Silicon Tracking System

The silicon tracker consists of many layers of silicon pixel and strip detectors that record where charged particles pass through each individual layer. Sophisticated tracking software is then used to link together individual "hits" in the layers to form a coherent track describing the real path of the particle.

Both pixel and strip silicon detectors operate on the same principle. A sheet of silicon, typically a few hundred microns thick, is fabricated with a p-n junction running through it. Electrically it is little more than an diode. A typical diode used in electronics preferentially allows current to flow through it in one direction leading to a current vs voltage (IV) curve as shown on the left of fig. 3.7. As shown in the figure, a negative voltage above V_{br} reverse biases the diode. In this state, all mobile charge carriers have been evacuated from the bulk. However, if the reverse voltage continues to grow, external charge carriers will be able to jump across the junction, leading to "breakdown" and a large increase in current. During manufacturing, silicon for particle detectors goes through qualification that ensures its breakdown voltage is high enough to operate efficiently. The right plot in fig. 3.7 shows the current vs reverse voltage for several silicon detector sensors.

When a silicon sensor is reverse-biased, there is normally only a tiny "leakage" current that flows through it. However, when an energetic charged particle such as an electron, muon, proton, etc. passes through the sensor, it interacts with the atoms in the material to raise orbital electrons into the conduction band of the semiconductor.

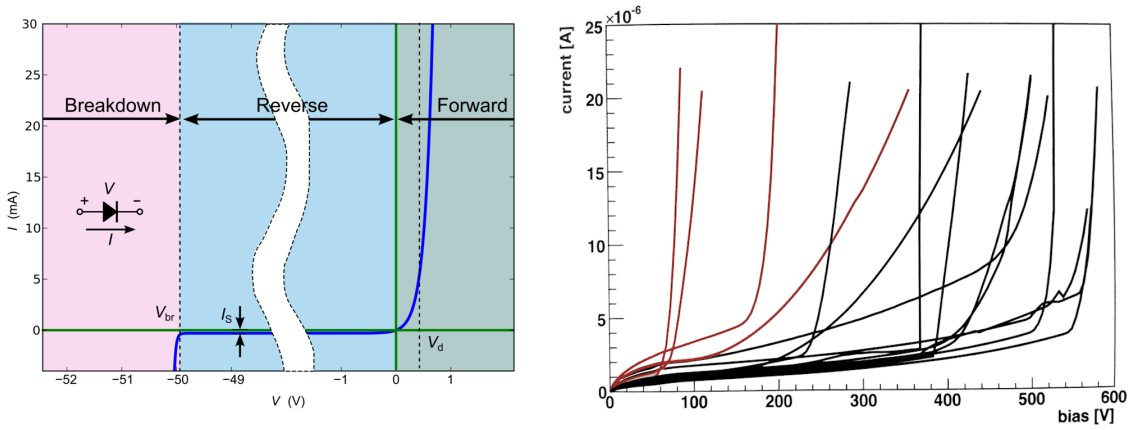

Figure 3.7: Left: illustrative IV curve for an electronic diode. Right: IV curves for sensors produced for the CMS tracker[34]. Black indicates a good sensor while Red indicates the sensor failed quality control for having insufficient breakdown voltage. In addition, this shows that even before breakdown, a small "leakage" current flows through the sensor.

This creates electron-hole pairs that drift apart due to the electric field resulting from the reverse bias voltage. Eventually, the electrons reach the surface where they are collected by conductive strips (strip detector) or bump bonds (pixel detectors) to be fed into a nearby readout chip. This is illustrated in fig. 3.8

The original CMS tracker had three layers of pixel detectors in the barrel region (BPIX) and two on each forward region (FPIX) (fig. 3.9). In 2017, an upgraded version of the pixel detector, the Phase-I upgrade, was installed that increased the number of layers to four in the barrel and three in each forward region. For both detectors, the pixels were 100 μm by 150 μm. More information on the upgrade project and the pixel detector can be found in chapter 6.

Surrounding the pixel detector is the silicon strip tracker. As shown in fig. 3.10, the strip tracker has four sections: the inner (TIB) and outer (TOB) barrel, the inner disks (TID), and the endcap (TEC). The pitch of the strips in the different sections has been tuned to balance reconstruction precision, occupancy, and construction practicality,

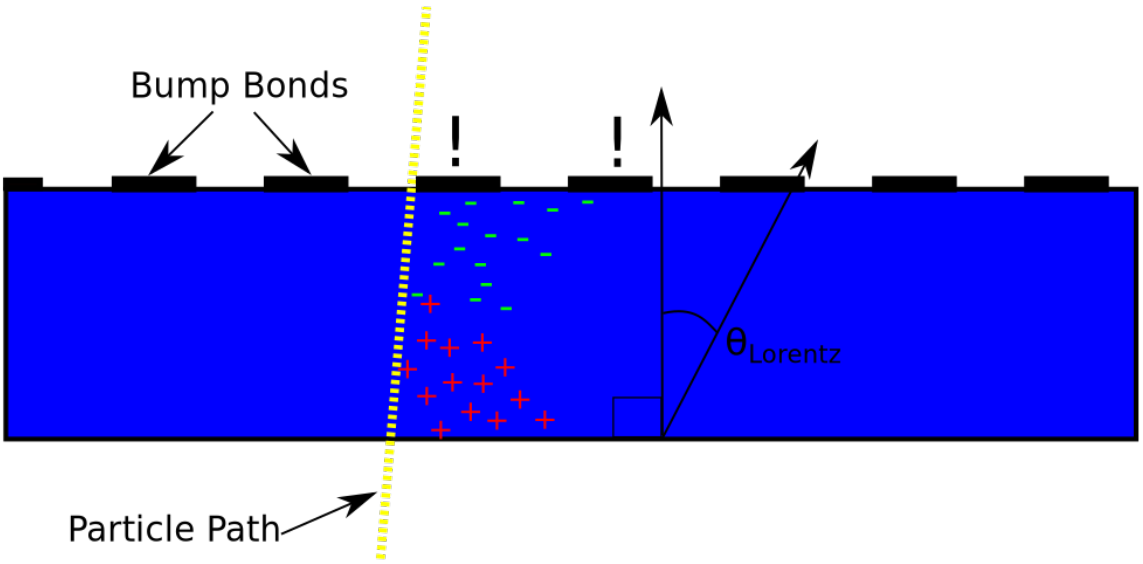

Figure 3.8: Illustration of a silicon sensor's principle of operation. This shows the drift of electrons and holes in the presence of a magnetic field pointing into the page and an electric field pointing down. The drift angle of the electrons due to the sum of the electric and magnetic forces on them is called θ_{Lorentz}. In this case, the drift of charge liberated by the energetic particle has spread enough to deposit charge in two pixels. This is typical, and this "charge sharing" is critial to achieving sub-pixel precision of the original particle's path.

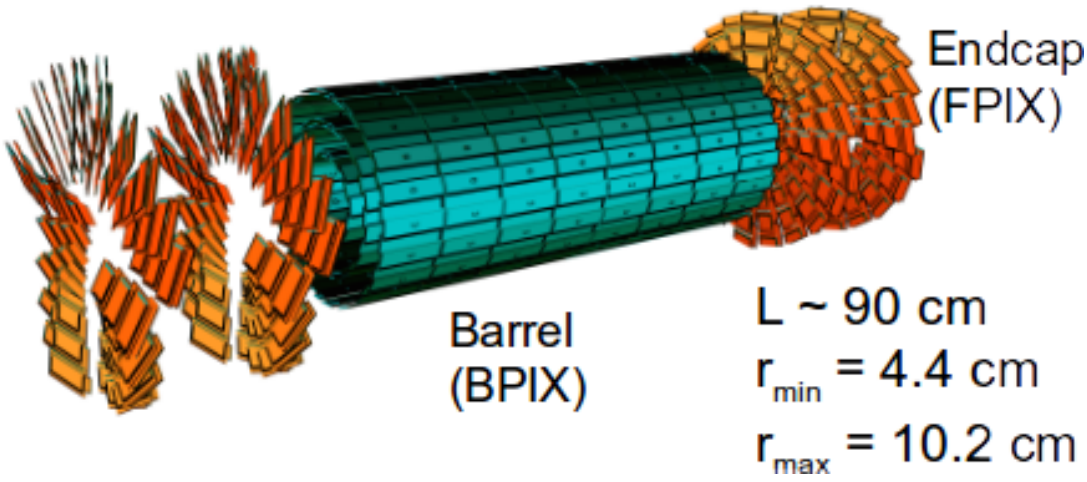

Figure 3.9: The original CMS pixel detector.[35]

resulting in strips ranging in width from as small as 80 μm in the TIB to 180 μm in the outer layers of the TOB and TEC. The strips are oriented along the z-axis for the barrel and along the radial direction for the endcap layers. There are also two layers of double-sided strip detectors in the TOB with one side rotated 100 mrad relative to the other. Together, these two sides can give a 3D position measurement[36].

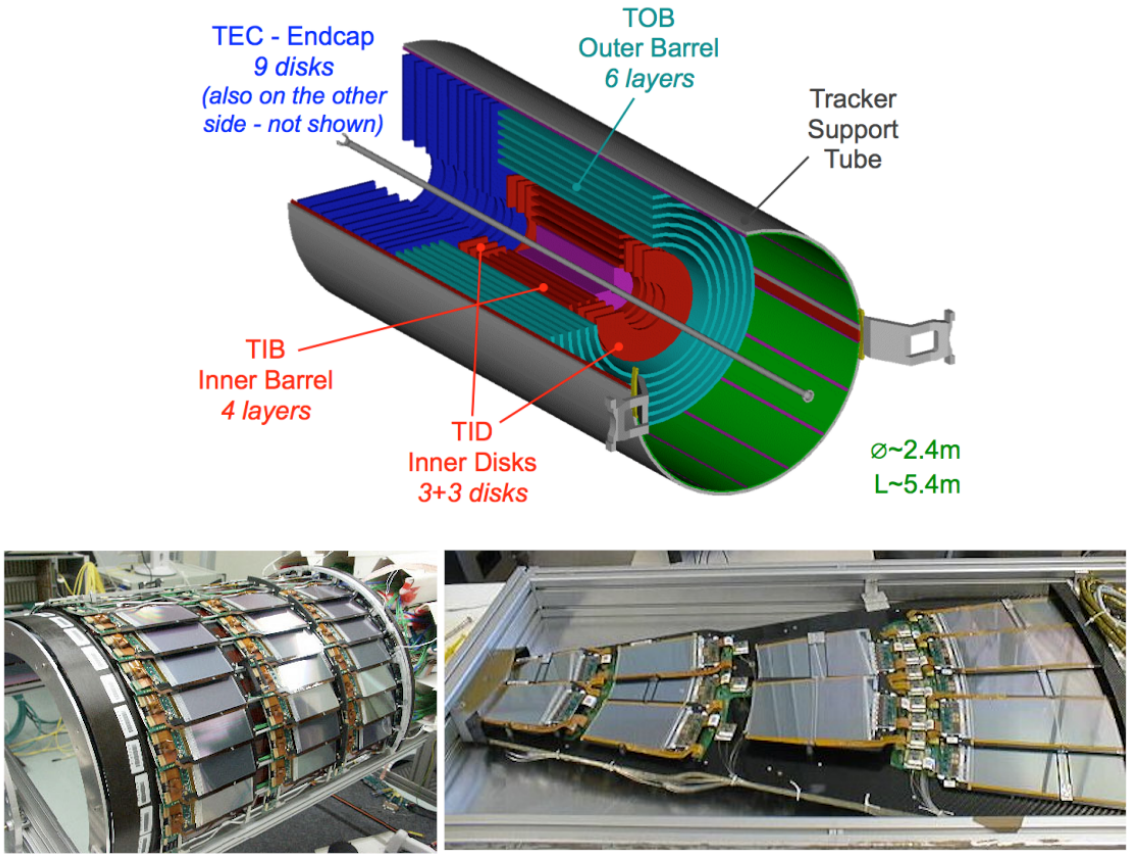

Figure 3.10: The CMS strip tracker.[37, 38]

3.2.2 Electromagnetic Calorimeter

After leaving the tracker, particles reach the ECAL. Electrons and photons interact with the material in the crystals to create an electromagnetic *shower*. The shower occurs when electrons interact with the atoms of the material to radiate bremsstrahlung,

or braking, photons. If the photons are energetic enough, they also interact with the material to produce electron-positron pairs which will continue the shower. This process continues until the particles no longer have enough energy to support the aforementioned processes. The deposition of energy from the shower into the ECAL crystals is used to help reconstruct photons and electrons in the original event.

The ECAL used by CMS is built with 75,848 lead tungstate ($PbWO_4$) crystals. Lead tungstate was chosen for its high density (8.3 g/cm^3), and short radiation length (X_0=0.89 cm). It it also desirable because it tends to produce well-collimated, narrow showers, having a Molière radius of 2.2 cm. The electromagnetic showers inside the ECAL crystals produce scintillation light which is captured and amplified by avalanche photodiodes (APDs).

To augment the ECAL, the preshower detector (ES) is installed just inside the forward ECAL. It addresses a peculiar issue resulting from neutral pions. These particles will commonly be produced with high enough momentum that when they decay ($\pi^0 \to \gamma\gamma$), the photons will be so narrowly separated that the ECAL is at risk of identifying them as a single very high energy photon. Because Higgs searches were an important driver in the design of CMS, and $H \to \gamma\gamma$ was a potential discovery channel, the ES was added to help reduce the number of π^0 misidentified as high energy photons. The ES is constructed with alternating layers of lead and silicon detector, the first to initiate a shower and the second to give a high precision measurement of the shower-in-progress. This gives sufficient granularity to identify the narrowly separated photons from π^0 and other di-photon resonances.

3.2.3 Hadron Calorimeter

Electrons and photons are effectively stopped in the ECAL. What remains are muons and hadrons. The muons continue largely unimpeded through the HCAL, but hadrons

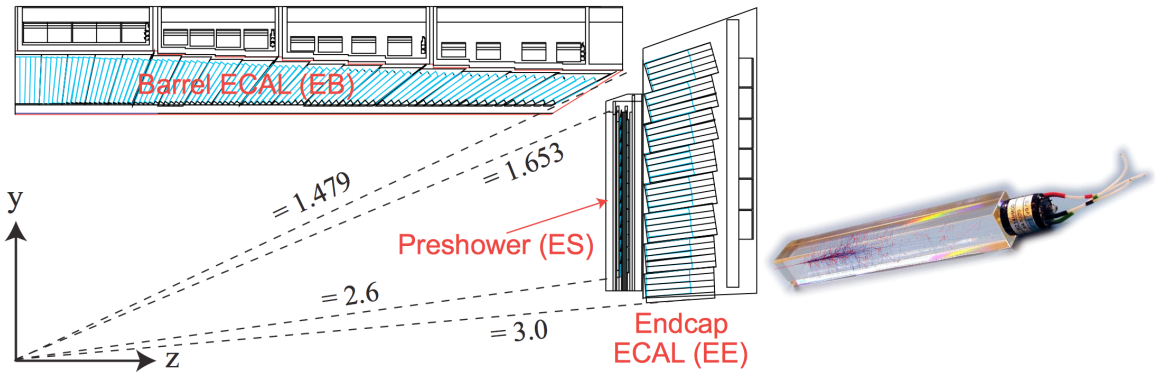

Figure 3.11: Left: A quarter-section of the CMS ECAL[39]. Right: A single ECAL crystal showing an artistic depiction of an electromagnetic shower.

are stopped by the dense layers of brass and scintillating plastic. The HCAL operates on a similar principle to the ECAL, except the initial reaction is mediated by the strong force as an incident hadron interacts with an atomic nucleus of material in the HCAL. The products of this reaction may go on to have additional nuclear interactions, if they are themselves hadrons, or start electromagnetic showers if they are photons or electrons. The brass layers serve as the absorber, the material chosen for being non-ferromagnetic and having a short interaction length ($\lambda_I = 16.42$ cm). Scintillators equipped with silicon photomultipliers (SiPM) sample the hadronic "shower" as it traverses a particular layer. These samples are then used to calculate the energy of the initial particle.

The HCAL is divided into a barrel region (HB) and endcaps (HE) in the forward regions that sit inside the solenoid coil. There is also an additional layer (HO) that sits outside the magnet to provide a cumulative 11 interaction lengths of material so the shower is completely captured within the calorimeter. The HCAL regions are themselves sectioned in ϕ/η into towers.

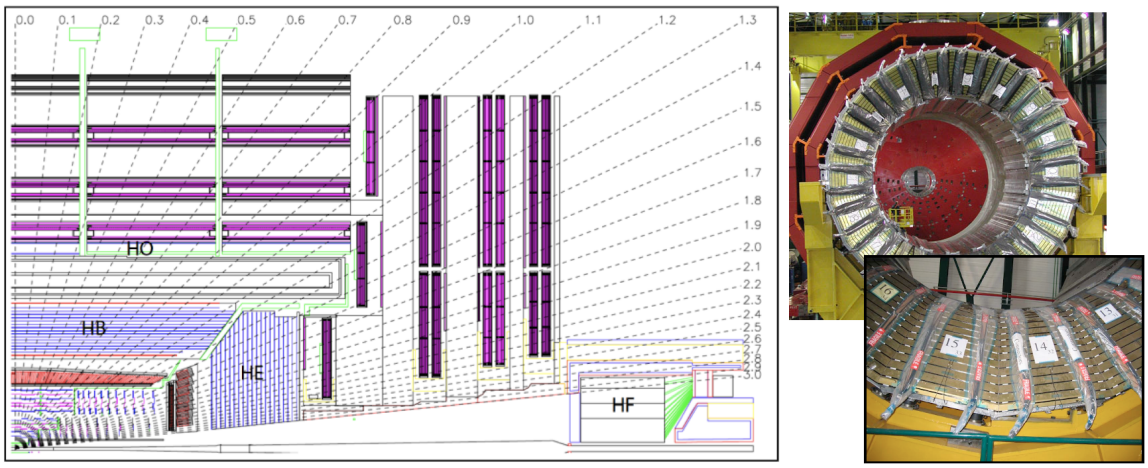

Figure 3.12: Left: A quarter-section of the CMS HCAL[35]. Right:A section of the HB. Right detail: A closer look at the HCAL sections, showing clearly the layers of brass and scintillator.

3.2.4 Superconducting Solenoid Magnet

A defining feature of the CMS experiment is its incorporation of a powerful superconducting solenoidal magnet (fig. 3.13). It measures 6.4 m in diameter and weighs 12,000 tonnes. It can produce a very uniform 3.8 T magnetic field throughout the interior of the solenoid. The coil wire is made of a Ni-Tb alloy and must be cooled to 4.7 K with a helium cryogenic to achieve superconductivity. Under normal operating conditions, the cable carries over 18000 amps of current. Magnetic field lines run in loops, which means that there will be a return field on the outside of the solenoid. The shape of the return field is controlled through the iron return yoke, which is seen painted red in figs. 3.13, 3.5.

3.2.5 Muon System

Interleaved with the iron return yoke mentioned in the previous section, and putting the *muon* in Compact Muon Solenoid is the muon system. Besides neutrinos, which are not directly detected by CMS, muons are the only particle that normally escape

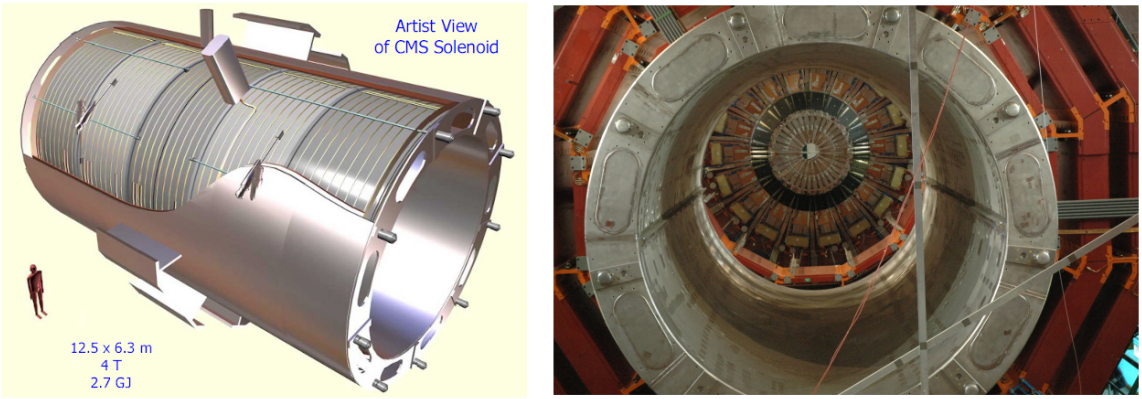

Figure 3.13: Left: 3D rendering of the CMS Solenoid magnet. Right: Photo showing the maget casing and a section of the iron return yoke[40].

the calorimeters and make it to the muon system. This makes identifying muons relatively trivial since any hits in the muon system must be from muons. Unlike the subsystems discussed so far, the muon system incorporates a diverse array of detector types into its design, as is shown in fig. 3.14. The barrel section of the muon system uses drift tubes (DT), fig. 3.15, interspersed with resistive plate chambers (RPC). The forward region uses cathode strip chambers (CSC) with resistive plate chambers as well. The motivation for employing different types of detectors stems from the different conditions in the barrel vs forward region. In the forward region, there is a more intense residual magnetic field making drift tubes inappropriate, thus leading to the use of CSCs. The RPCs were used to add redundancy to the system for use as in the muon trigger.

3.2.6 The Trigger System and Data Handling

Every event recorded by CMS consists of roughly 1MB of data. With bunch crossings occurring every 25 ns, that corresponds to a veritable flood of data that would be technologically infeasible to handle (3.5 Exabytes per day!). To solve this problem, a sophisticated trigger system was developed to only select a small subset of events

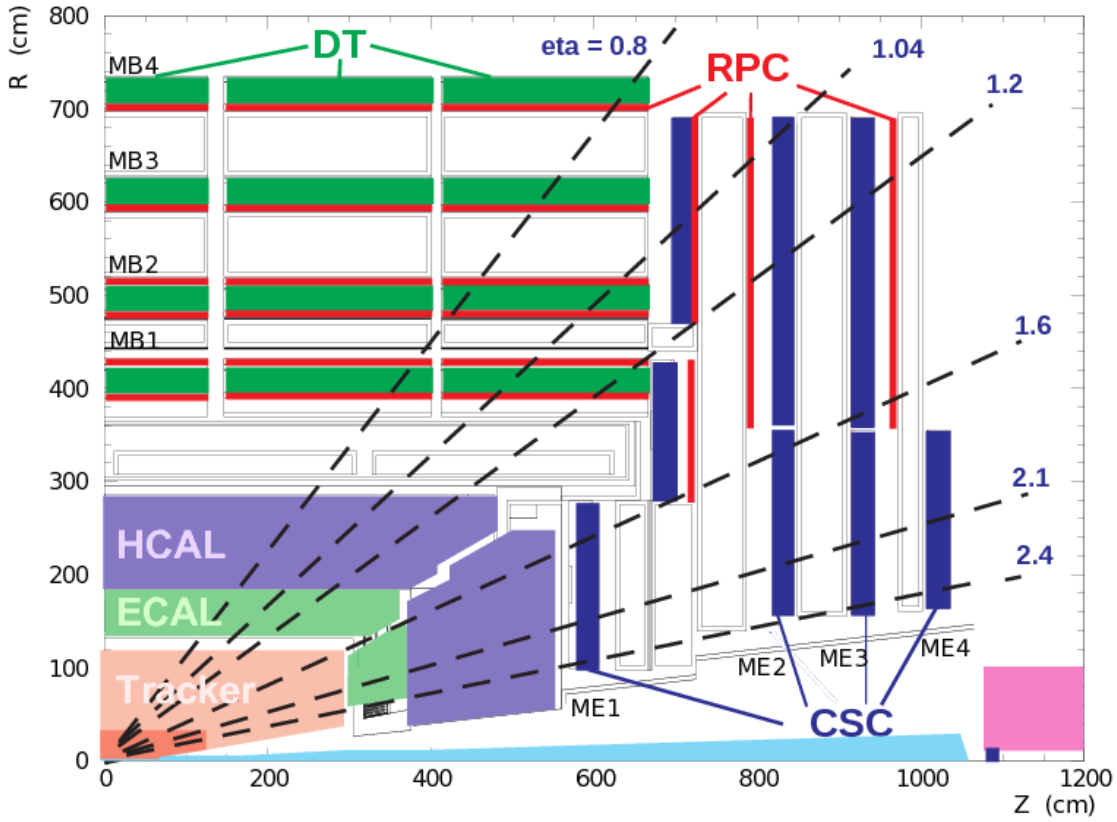

Figure 3.14: Schematic view of the CMS muon system.[41]

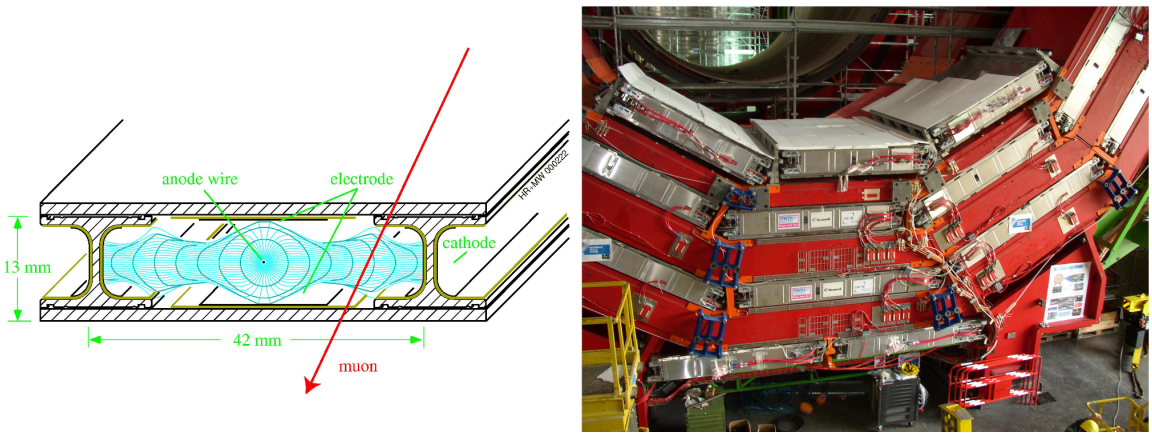

Figure 3.15: Left: Single drift tube cell. Right: Drift tube chambers (aluminum) sandwiched between steel plates of the yoke during installation[42]

for further processing and analysis. The trigger system is divided into two parts: the Level 1 (L1) trigger which triggers a readout of the entire detector, and the High Level Trigger (HLT) that decides if a newly acquired event is saved to disk for offline analysis.

The L1 trigger provides a rate reduction of three orders of magnitude, down to a rate of roughly 100 kHz. It does this by processing information from just the calorimeters and muon system on custom hardware consisting of both FPGA and ASIC processing units. Some of these processing units are embedded within the detector and others are located in the nearby counting room. The schema for how this information is processed is shown in fig. 3.16. The L1 trigger is designed to use information from just part of the detector to quickly (within 3.8 μs) identify particles with high momentum transverse to the beam axis. It uses these high transverse momentum particles to decide whether to trigger a readout of the rest of the detector.

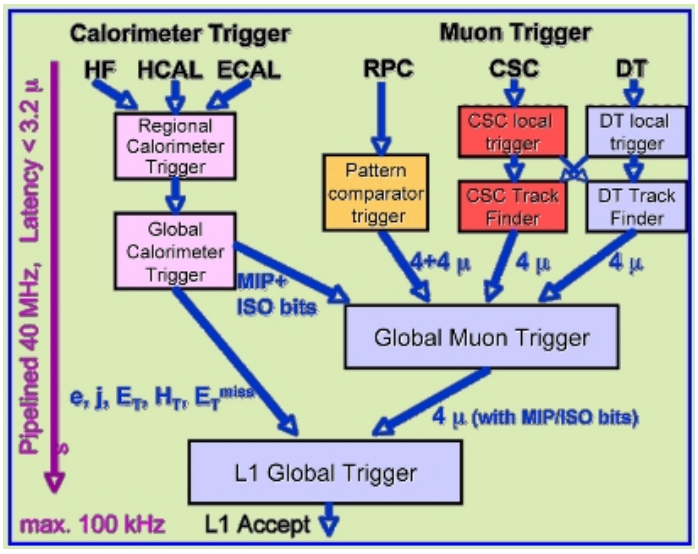

Figure 3.16: CMS L1 trigger scheme[43].

If an event passes the L1 trigger, it is further scrutinized by the HLT. The HLT runs on a dedicated server farm that does an initial reconstruction of the event. There

is a complex set of criteria that define many potential ways an event could pass the HLT. An example criteria could be a pair of electrons with very high momentum. Another could be a single very high energy muon. These different categories have been crafted to ensure that events having the signatures of interesting physics processes will be retained. To keep the total rate of events passing the HLT around 1000 Hz, some categories with naturally higher rates are *prescaled*, which means that a certain fraction of those events are discarded.

Events that pass the HLT are saved to disk, at which point the "Tier 0" computing cluster on the surface above the CMS cavern performs a full reconstruction. From that point, reconstructed events are collected into data sets based on which HLT paths they satisfied and when the events were collected. These data sets are then made available to the worldwide grid of computing resources for physicists to analyze.

The Worldwide LHC Computing Grid (WLCG) is responsible for providing physicists and other users access to the data collected at LHC experiments and processing resources to analyze that data. The organization is organized into four *tiers*, shown in fig. 3.17, each of which serves an important purpose.

- **Tier 0**: Physically split between two locations, CERN and the Wigner Institute computing center in Budapest, Hungary, the Tier 0 is responsible for the transformation of the raw data into a more compact form that can be distributed to the lower tiers, as well as providing quality control metrics that operators can use to monitor the accelerator and detector during operation.
- **Tier 1**: There are 13 Tier 1 sites. Normally hosted at large national computing centers, they are equipped with sufficient storage for LHC data sets and can handle large-scale reprocessing and safe-keeping of the corresponding output. They are also responsible for distributing data sets to Tier 2 facilities and storage

of simulated data sets generated at Tier 2s.

- **Tier 2**: There are 160 Tier 2 facilities on the Grid. They are typically housed at universities and other scientific institutions. They can store sufficient data and provide adequate compute resources for user analysis tasks.
- **Tier 3**: These are the machines that individual analysts access to perform their analysis tasks. They are typically associated with a specific Tier 2 facility, but can provide access to Grid resources around the globe.

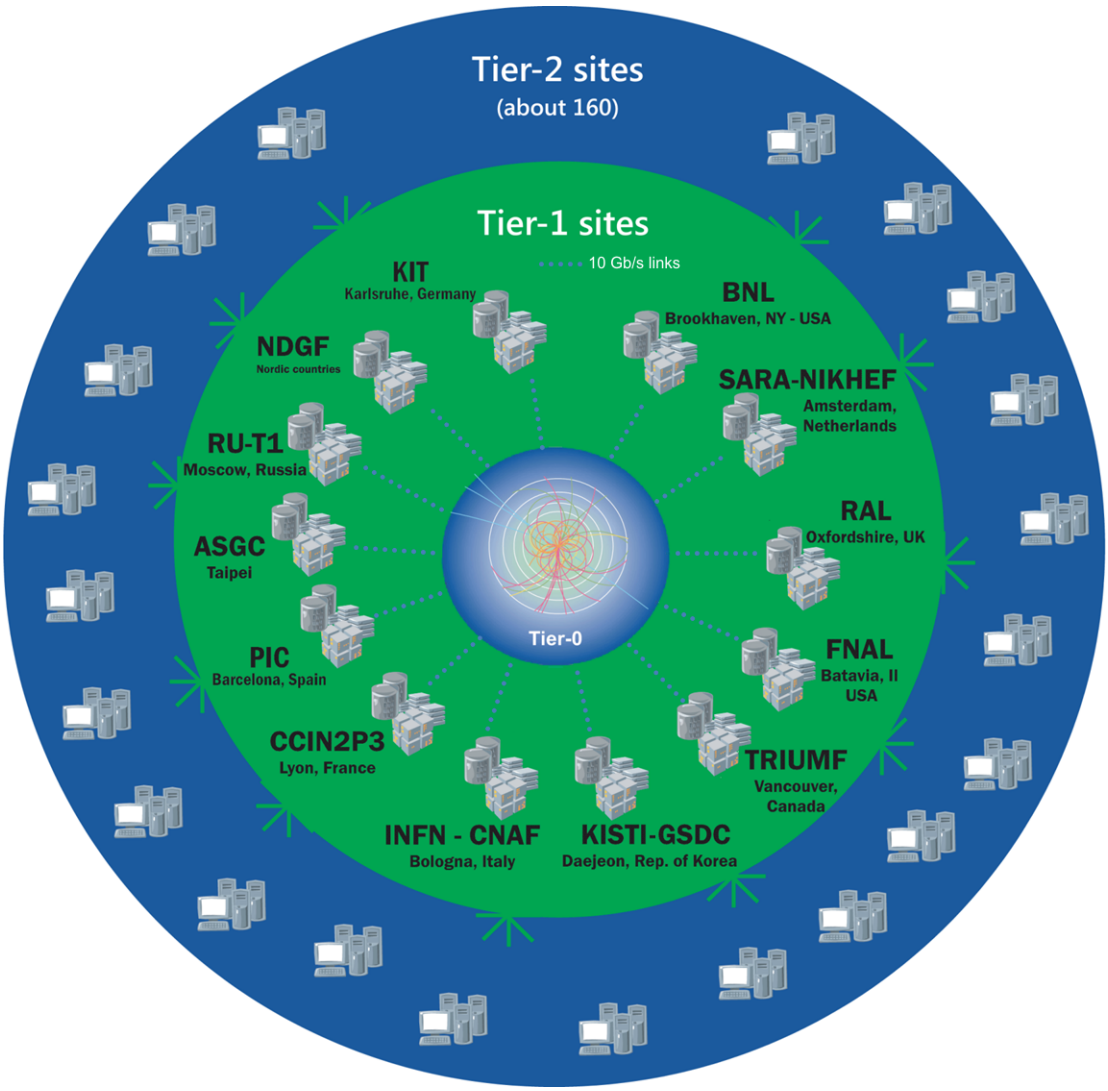

Figure 3.17: The WLCG structure. [44].

Chapter 4

Event Simulation and Reconstruction

An essential aspect of particle physics experiments is the ability to accurately infer the types of particles and their kinematic properties in each event from the raw detector readings. This process is called event reconstruction. To achieve this, sophisticated algorithms are developed to correlate readings within and across subdetectors. The development of these algorithms is guided by an accurate simulation of the detector response to simulated collisions. Simulation is also employed in the interpretation of physics measurements by providing predictions for the rate and kinematics of physics processes of interest. Disagreement between experimental observation and predictions made in this way can be an indication of new physics, but can also point out mis-modeling of the detector, the physics process, or simply bugs in any part of the software chain. Therefore, rigorous examination and crosschecks must be applied to instill confidence in the accuracy of the simulation.

4.1 Event Simulation

Event generator software is used to simulate the initial hard-scatter of partons from the colliding protons. The software used by LHC experiments implements sophisticated Monte-Carlo (MC) techniques to both calculate cross-sections for SM and certain

BSM processes, and to generate samples of events that can be compared with real data. The generation of events can be broken down into four distinct stages.

1. **Hard Scatter**: This step uses the *parton distribution functions* (PDFs). The PDFs are effectively the probability distributions of the proton's different constituent particles to carry a certain fraction of its energy. Then the rules of perturbative quantum field theory are applied to create a set of Feynman diagrams for the process under consideration (e.g. $gg \to t\bar{t}$). The integrals encoded by these diagrams are then calculated using Monte-Carlo methods to produce a cross section and set of events with the output particles having the correct angular and momenta distributions up to some order of perturbation theory.
2. **Hadronization and Fragmentation**: The particles produced by the hard scatter step are often not the particles that will be observed by the detector. For example, quarks will generally hadronize and form jets. Colored and charged particles can radiate gluons and photons, respectively. The partons of the interacting protons not directly involved in the hard scatter will generally also fragment and result in additional particles. These are referred to as the "underlying event".
3. **Mixing**: Each bunch-crossing has many additional, though generally with low momentum transfer, proton-proton interactions that also create particles. These extra collisions are referred to as "pileup interactions". Many of these events are simulated separately and then "mixed" with the hard scatter event to produce a realistic collision.
4. **Detector Response**: At this stage, the collection of particles in the event are the ones that will interact with the detector materials. A detailed model of CMS is used with GEANT4[45] to simulate interactions with detector materials.

This includes bremsstrahlung radiation, electromagnetic and hadronic showers, and decays of unstable hadrons in-flight. The result of this simulation is a set of readings in detector readout electronics that can then be fed into the same reconstruction algorithms that are used for real data.

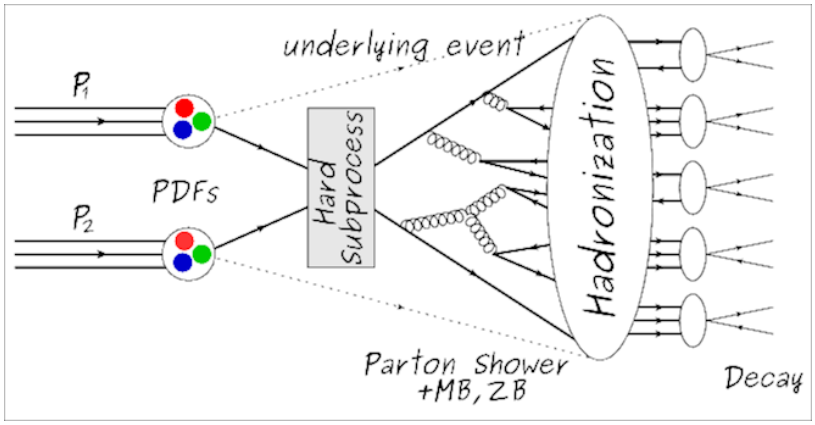

Figure 4.1: The event generation process. Shown is the process from PDF to hard scatter, to hadronization and fragmentation.[46]

4.2 Event Reconstruction

The strategy that CMS uses to reconstruct particles is referred to as "Particle Flow" (PF)[47]. PF attempts to identify every particle in the event. This approach requires a very highly granular detector to separate out nearby particles. High granularity becomes particularly important in the process of reconstructing jets which can consist of many closely spaced particles. The calorimetry system can be used to measure the jet energy, but in combination with the tracker to measure the momentum of the charged components of the jet, the precision of measurement can be improved dramatically. The key, then, to PF reconstruction is to be able to link together hits in the different subdetectors to increase reconstruction effectiveness, while at the same time avoiding assigning any particular detector signal to multiple particles.

Before the readings in individual subdetectors can be linked together, their raw hit data must be processed into higher level objects. For the tracker, the first step is to combine hits in adjacent pixels together into groups whose charges presumably originated from a single particle. This process is called clustering. The next step involves finding the sets of clusters across layers that that can be strung together to form the track of a particle. The generic algorithm for this is called Combinatorial Track Finding (CTF)[48]. The first step in CTF is finding pairs, triplets, or in the case of the Phase I upgrade, quadruplets, of clusters in the pixel detector that are consistent with a track originating from the luminous region of CMS. This gives an initial estimate of the particle's charge and momentum, along with associated uncertainties. A statistical model augmented with physical rules known as a Kalman Filter is employed to extrapolate this "seed" through the rest of the tracker, attaching more clusters as the extrapolation moves through the tracker. A helical best-fit is done on the final collection of clusters. The quality of this fit, along with other quality metrics such as the number of layers with missing clusters, is used to decide if this track is to be kept for further processing. This procedure is performed in several iterations, starting with very stringent matching requirements to identify the "easy" to reconstruct particles (generally isolated, with high momentum). Clusters from earlier iterations are removed so that subsequent iterations with looser matching requirements do not suffer from a prohibitively large number of combinations. This approach is also applied to the muon system to build muon tracks.

In the calorimeters, hits in individual ECAL crystals or HCAL towers are grouped to form clusters. This clustering is performed by first finding local maxima in the energy deposition across the calorimeter. These maxima are called seeds. Crystals/towers adjacent to the seeds with energy above a certain threshold are then grouped with the seed, forming a cluster. In a crowded event, it is possible for different clusters to

overlap. In this case, a specialized algorithm is employed to compute the sharing of energy between the clusters. An example event demonstrating this is shown in fig. 4.2.

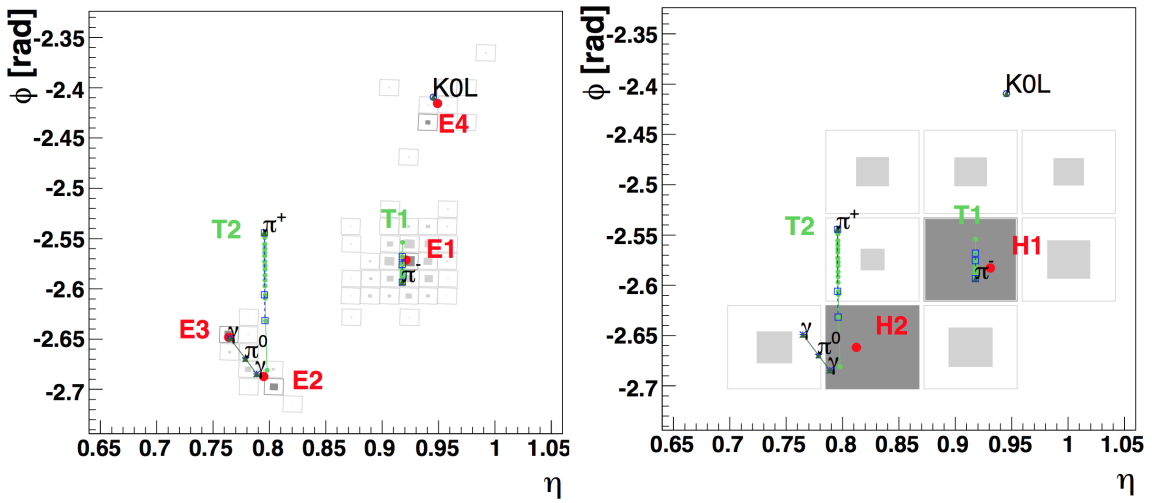

Figure 4.2: Event display for a single jet composed of a $\pi^+\pi^-$ pair, a $\pi^0 \to \gamma\gamma$, and a K_L^0 with energy deposits in the ECAL(left) and the HCAL(right). The jet results in four Particle-Flow clusters (E1-E4) which resulted from the π^-, the K_L^0, and the two photons. In the HCAL, only the charged pions deposit energy, resulting in two hadronic Particle-Flow clusters, H1-H2.[47]

The final step in the PF algorithm is to link together the building blocks from the four subdetectors: tracks from the tracker and muon system, and ECAL and HCAL clusters. Tracks from the tracker are matched with clusters by extrapolating the helical track to the depth in the calorimeter where the shower is expected to have started. If this position lies within a cluster, the track is linked with it. Bremsstrahlung photons from electrons are accounted for by looking for additional ECAL deposits that align with the tangent of the track at its intersection with each of the tracker layers. If such deposits exist, they are linked with the track also. Clusters in the ECAL and HCAL, as well as the ES and ECAL, can be linked if the ECAL(ES) cluster lies within the boundaries of an HCAL(ECAL) cluster in the $\eta - \phi$ plane. Finally, if a combined fit between a tracker track and a muon system track results in a sufficiently small χ^2,

the two tracks are linked together.

The PF particle collection is created from a set of linked blocks based on which subdetectors contributed hits to it. The options are:

- charged hadron: a tracker track and HCAL cluster
- neutral hadron: an HCAL cluster with no tracker track
- electron: a tracker track and ECAL cluster
- photon: an ECAL cluster with no tracker track
- muon: a tracker track matched with a muon system track

The output of the PF algorithm is a collection of reconstructed particles and their momenta. This information can then be fed into higher-level algorithms to reconstruct jets, including jet flavor, and transverse momentum imbalance.

4.2.1 Jet Reconstruction

As mentioned in chapter 2, highly energetic quarks produced in LHC collisions fragment to produce a spray of collimated particles referred to as a jet. Jets are constructed from PF particles using the anti-k_T clustering algorithm[49]. The anti-k_T algorithm works as follows. For each input object k and for each pair of objects (i, j), a beam-distance d_{kB} and a distance d_ij is calculated. They are defined as

$$d_{kB} = 1/\left(p_T^k\right)^2$$
$$d_{ij} = \min\left(\left(p_T^i\right)^2, \left(p_T^j\right)^2\right)\frac{\Delta R_{ij}^2}{R^2}$$

where R is a tunable parameter setting the granularity of the jet reconstruction, but has typical values are around 0.4-0.5. The smallest d_{ij} is compared to the smallest d_{kB}. If it smaller, the objects i and j are combined into a new object with momentum

$p = p_i + p_j$, otherwise the object k is considered as a jet and removed from the collection of objects. This procedure iterates until all objects have been removed. This algorithm leads to jets that have a circular shape as shown in fig. 4.3.

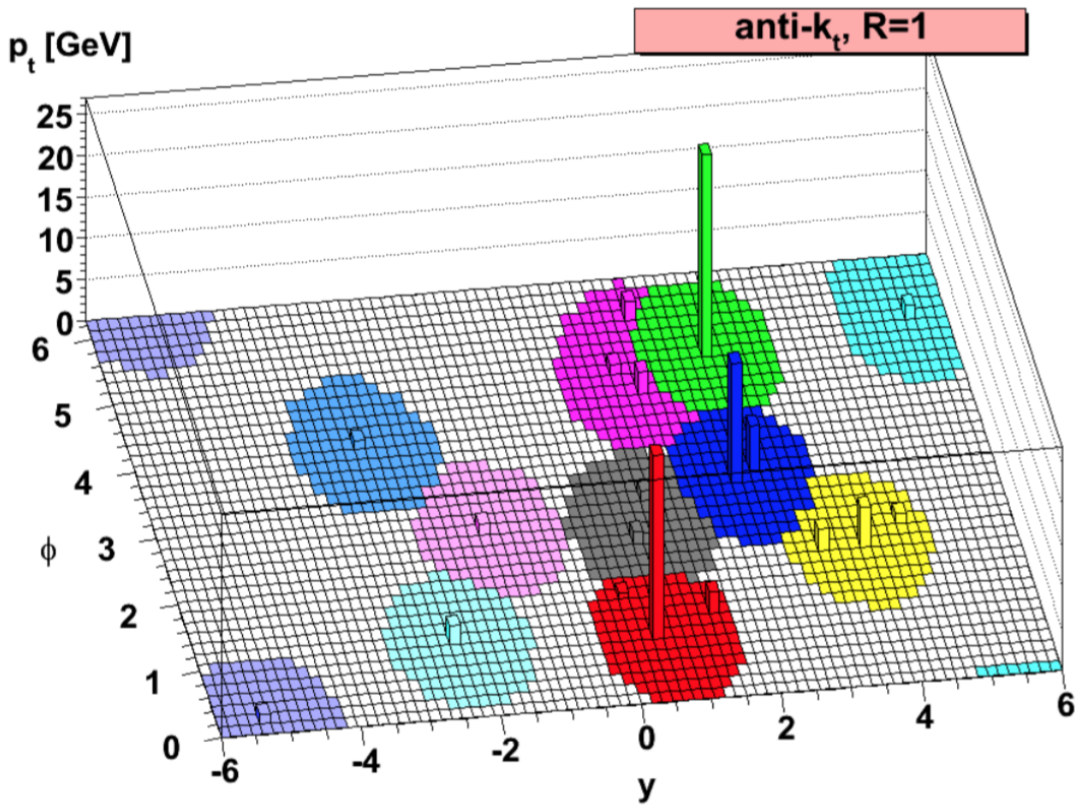

Figure 4.3: Jet clustered using the anti-k_T algorithm. Histogram entries are the initial particles from which the jets are formed and the magnitude of the entries are the p_T of those particles.[49]

4.2.2 Bottom Quark Jet Identification

Bottom quarks have very small CKM couplings to the other quarks which decreases their decay rate to lighter quarks. This leads to bottom flavored hadrons produced in collisions traveling a measurable distance, typically on the order of a few millimeters, from the primary interaction before decaying. The secondary vertex defined by this

decay point is a signature of bottom quarks. Jets resulting from bottom quarks also contain on average more particles than jets from lighter quarks due to the bottom quark's higher mass. CMS deploys a dedicated algorithm[50] to combine information related to these qualities from the particles reconstructed from PF to identify bottom quarks. This procedure is referred to as b-tagging.

4.2.3 Missing Transverse Momentum

In hadron collisions the longitudinal momentum of the colliding partons is unknown. However, the transverse momentum is zero[1]. This fact can be used to infer the presence of particles that are invisible to the CMS detector. In the SM these are neutrinos, but theories beyond the Standard Model predict other particles that will not be seen such as dark matter particles. The metric that is used to make this inference is the missing transverse momentum, $\not{p}_T$. This is calculated by taking the negative of the vector sum of the transverse momenta of all observed particles. For events that produce no undetected particles, this sum should be very close to zero, otherwise the undetected particle(s) will leave an imbalance. The magnitude of the missing transverse momentum is called the missing transverse energy, $\not{E}_T$.

4.3 Optimization of Electron Seed Production

Like the tracking algorithm described above, the reconstruction of electrons begins with the creation of *electron seeds*. Part of the research for this dissertation involved the tuning of the algorithm that builds these seeds. This section discusses that work.

The construction of electron seeds consists of linking together *tracker seeds* with ECAL Superclusters (SC). These tracker seeds originate through the same method as

[1]Technically the partons have some initial transverse momentum due to beam dispersion, and momenta of the parton within the rest-frame of the proton, but these are tiny.

the seeds used in PF tracking. They are collections of pixel clusters across layers in the pixel detector that are consistent with a particle originating in the luminous region. A SC is a set of nearby ECAL crystals whose energy distribution passes certain criteria to allow them to be grouped together. The procedure for matching tracker seeds with SCs is as follows:

1. Use the SC energy and position with the position of the beam-spot to make a track hypothesis for both positive and negative charge. Fig. 4.4 shows one possible charge hypothesis.
2. Project that track onto the layer of the innermost hit in the tracker seed under consideration. Require that the hit position and track projection are within a certain ($\delta\phi$, $\delta R/z$) window of each other. The orientation of the layers of the tracker dictates that z be used for BPIX and R for FPIX. Because the initial track hypothesis uses the beam spot, which is elongated several centimeters in z, this initial matching uses a large $\delta R/z$ window.
3. Create a new track hypothesis using the beam spot and the first hit position with the energy of the SC. The z coordinate of the beam spot position is calculated by projecting a line from the SC through the first matched hit to the point of closest approach with the z-axis.
4. Project the new track out onto the layers of successive hits in the tracker seed. Again, require that the projected position and the hit match within a certain window.
5. Quit either when a hit fails to match or when all hits have been matched.

If a tracker seed has enough matching hits it is paired with the SC, and they are passed together for full electron tracking. This involves the use of a modified Kalman Filter known as a Gaussian Sum Filter to propagate the initial track through the

rest of the tracker. These "GSF electrons" continue on to several more filters and corrections before they are used in physics analyses.

Electron seeds created through this procedure are referred to as "ECAL-driven". There are also "tracker-driven" electron seeds which are not matched with ECAL SCs, and proceed through the GSF tracking algorithm based on tracker information alone. After the track has been reconstructed, it may then be matched with a SC. The tracker-driven seeds help to compensate for inefficiencies coming from the ECAL-driven matching procedure. In the end, the ECAL-driven and tracker-driven electron collections are merged to produce a single collection of electron candidates.

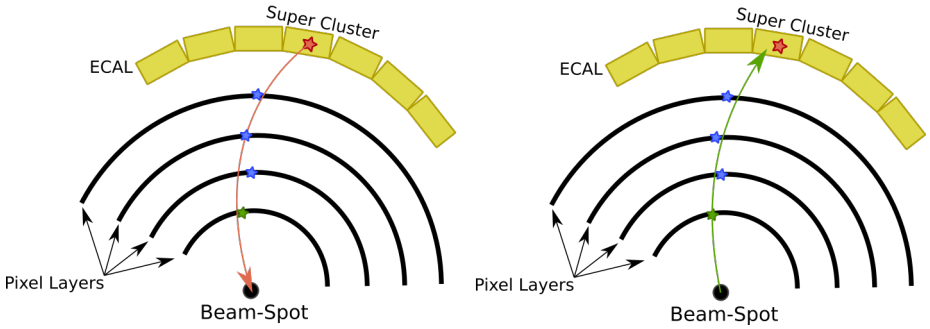

Figure 4.4: Seed-SC matching procedure. Left: The initial track hypothesis using the beam-spot with the SC position and energy. Right: The new track hypothesis using the beam-spot and first hit's positions with the SC energy. Note that the four layers shown here are representative of the Phase I upgrade of the pixel detector.

This general approach was developed during early CMS operation, but the installment of the Phase I pixel detector motivated a re-write of the underlying algorithm to handle the additional layers. The new implementation was designed to be more flexible, allowing for a variable requirement on the number of matched hits, a significant change from the previous algorithm which would only match two hits. Work was done to optimize this new hit-matching algorithm for the new pixel detector. In particular, the $\delta\phi$ and $\delta R/z^2$ windows were tuned to maximize efficiency while also keeping the

[2] R/z should be understood as either R or z based on whether hits in the barrel or endcap are being considered, not as a ratio.

number of spurious electron seeds at a minimum.

The size of these matching windows is defined parametrically in terms of the transverse energy(E_T) of the SC. The transverse energy is $E\cos\theta$, where E is the energy of the SC. The function for determining the window size is

$$\delta(E_T) = \begin{cases} E_T^{\text{high}}, & E_T > E_T^{\text{thresh}} \\ E_T^{\text{high}} + s(E_T - E_T^{\text{thresh}}), & \text{otherwise} \end{cases}$$

Normally, s is negative which means that the cut becomes tighter with higher E_T until E_T^{thresh} where it becomes a constant. So the optimization was to E_T^{high}, E_T^{thresh}, and s. The challenge to performing a rigorous optimization of these parameters is that they are individually defined for the first, second, and any additional matched hits and also separately for ϕ and in R/z, meaning that the optimization would have to be performed in many dimensions. In addition, the figure of merit for the optimization is difficult to clearly define since a balance must be struck between electron reconstruction efficiency and the purity of the set of reconstructed electrons. Given these challenges, a more ad-hoc approach was developed. The approach consisted of first acquiring two samples of simulated data: A simulated sample of $t\bar{t}$ events with many jets containing photons and charged hadrons capable of faking electrons, as well as genuine electrons from W boson decays, and a sample of simulated $Z \to e^+e^-$ events with many genuine electrons and relatively few electron faking objects. The next step is to define efficiency and purity metrics. Because this is simulated data, it is possible to perform truth-matching to determine if a reconstructed track originated from an electron or not. A reconstructed electron is considered truth-matched if there is a simulated electron in the event within a cone of $\Delta R < 0.2$ centered on the reconstructed electron. Efficiency is then defined as the proportion of simulated

electrons that get successfully reconstructed as ECAL-driven GSF tracks, and purity is the proportion of ECAL-driven GSF tracks that resulted from a simulated electron.

Hit residuals are the $\delta\phi$ and $\delta R/z$ between hits and the projected track in the matching procedure. Understanding the distribution of these residuals will guide the choice of matching windows. The simplest way to study the residuals is to run the hit-matching algorithm with very wide windows to avoid imposing an artificial cutoff on the distributions of the residuals. Fig. 4.5 shows the distributions of residuals of hits in the innermost barrel layer for truth-matched and non-truth-matched seeds. Also plotted are the contours where 90% or 99.5% of hits are to the left. The residual distributions are very different based on whether the seed was truth-matched or not. Recall that for the first hit, the luminous region is used for one end of the projected track, and since the luminous region is significantly elongated in z, the residuals can be quite large. However, the $\delta\phi$ residuals for truth-matched tracks tend to be tiny ($<.5°$), while non-truth-matched residuals tend to be larger, especially at low E_T.

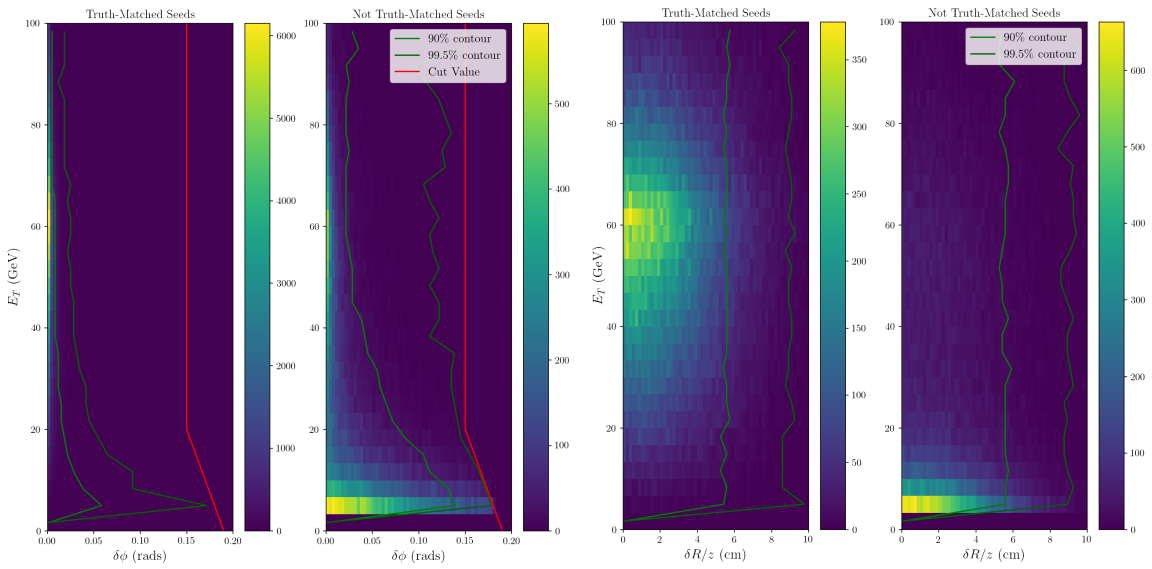

Figure 4.5: Residual distributions for BPIX Layer 1 hits in truth-matched and non-truth-matched seeds. Cut on δz is beyond the axis so omitted from plot.

Fig. 4.6 shows the residuals for the second matched hit for hits in the second barrel layer. After matching the first pixel hit, the projection of the track becomes much more precise, roughly a factor of 20 times smaller for $\delta\phi$ and over 200 times smaller for δz.

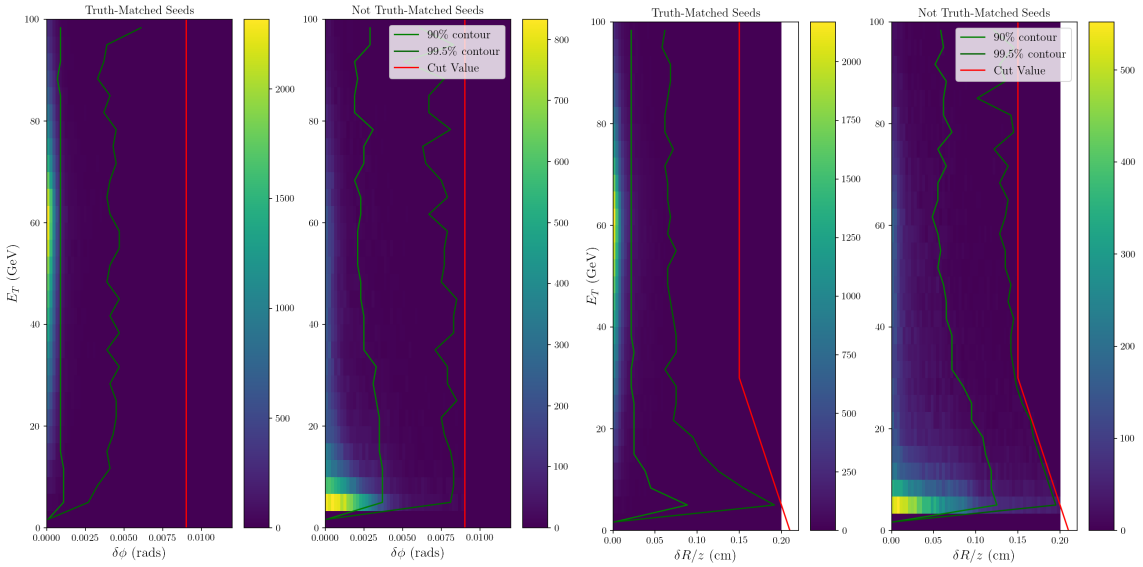

Figure 4.6: Residual distributions for BPIX Layer 2 hits in truth-matched and non-truth-matched seeds.

Guided by these distributions, four sets of windows were designed with varying degrees of restriction. The parameters for these windows are listed in table 4.1.

Table 4.1: Parameters for pixel-matching windows. The `narrow` window was developed for the HLT deployment of the algorithm, and will also be referred to as `default`, while the `extra-narrow`, `wide`, and `extra-wide` windows are the HLT settings scaled by 0.5, 2, and 3, respectively. Bold numbers indicate parameters that are modified across window settings.

		`extra-narrow`	`narrow`(default)	`wide`	`extra-wide`
Hit 1	$\delta\phi$: E_T^{high}	**0.025**	**0.05**	**0.1**	**0.15**
	$\delta\phi$: E_T^{thresh}	20.0	20.0	20.0	20.0
	$\delta\phi$: s	-0.002	-0.002	-0.002	-0.002

		`extra-narrow`	`narrow`(default)	`wide`	`extra-wide`
	$\delta R/z$: E_T^{high}	9999.0	9999.0	9999.0	9999.0
	$\delta R/z$: E_T^{thresh}	0.0	0.0	0.0	0.0
	$\delta R/z$: s	0.0	0.0	0.0	0.0
Hit 2	$\delta\phi$: E_T^{high}	**0.0015**	**0.003**	**0.006**	**0.009**
	$\delta\phi$: E_T^{thresh}	0.0	0.0	0.0	0.0
	$\delta\phi$: s	0.0	0.0	0.0	0.0
	$\delta R/z$: E_T^{high}	**0.025**	**0.05**	**0.1**	**0.15**
	$\delta R/z$: E_T^{thresh}	30.0	30.0	30.0	30.0
	$\delta R/z$: s	-0.002	-0.002	-0.002	-0.002
Hit 3+	$\delta\phi$: E_T^{high}	**0.0015**	**0.003**	**0.006**	**0.009**
	$\delta\phi$: E_T^{thresh}	0.0	0.0	0.0	0.0
	$\delta\phi$: s	0.0	0.0	0.0	0.0
	$\delta R/z$: E_T^{high}	**0.025**	**0.05**	**0.1**	**0.15**
	$\delta R/z$: E_T^{thresh}	30.0	30.0	30.0	30.0
	$\delta R/z$: s	-0.002	-0.002	-0.002	-0.002

The pixel-matching algorithm was run on simulated data and efficiency and purity were measured, as is plotted in fig. 4.7. Of the four working points, `extra-narrow` was discarded for its distinct drop in efficiency and the `extra-wide` working point was dropped for being negligibly different from the `wide` working point. The performance of the remaining two working points on electron candidates using simulated samples of $Z \to e^+e^-$ and $t\bar{t}$ events are shown in fig. 4.8. This figure shows efficiency and purity differentially in p_T[3], η, and ϕ of the GSF tracks that resulted from the pixel-matched

[3]We use p_T here instead of E_T because these are track kinematics, not SC quantities, although in practice they will be quite similar

seeds. The performance of the algorithm is demonstrated to be as good or better than the original implementation.

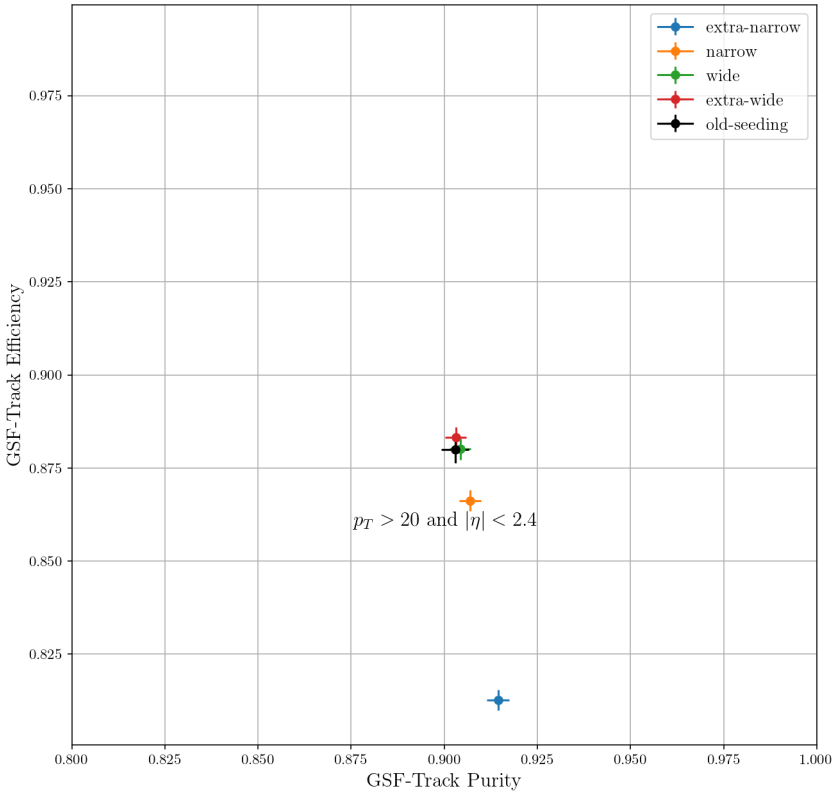

Figure 4.7: GSF tracking efficiency vs purity for tracks produced with pixel-matching at various working points measured in $Z \to e^+e^-$ events. For reference, the performance of the original implementation is also included.

Another feature of the new algorithm is that on average it produces fewer seeds. In the old algorithm, only pairs of hits are matched. However, the additional layers of the Phase I pixel tracker created tracker seeds with up to four hits making matching only two hits easier and resulting in more electron seeds. The additional seeds created computational issues for HLT, which motivated the rewrite. Fig. 4.9 shows how the number of seeds is reduced by the new algorithm.

An important feature of the initial implementation was that in the process of matching two hits in the tracker seed, it could skip hits. Hit skipping refers to a feature

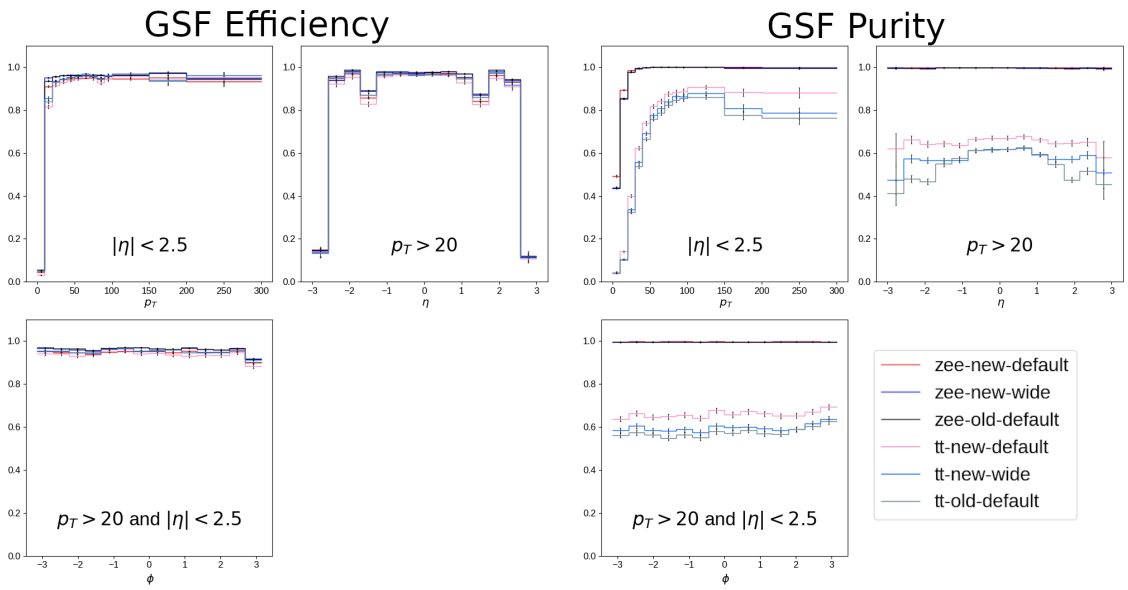

Figure 4.8: The efficiency and purity of different working points. The legend is to be interpreted as the sample ($t\bar{t}$ or $Z \to e^+e^-$), the algorithm (old or new), and the algorithm's working points.

of the matching algorithm such that if a hit fails to satisfy its prescribed matching criteria, it is skipped and that criteria is instead applied to the next hit in the tracker seed. As long as a sufficient number of hits match, the tracker seed is matched with the SC. The rewrite did not include this feature, and lack of hit-skipping can lead to a loss of efficiency because it is more selective about what seeds get matched with each SC. To avoid this inefficiency, a workaround was introduced.

To understand the workaround, one first has to understand how these tracker seeds are constructed. As mentioned previously, these seeds are normally created through several iterations, starting with quite stringent requirements. Hits that make it into these initial seeds are removed from consideration in subsequent iterations. By removing hits in each iteration, later iterations can have much less stringent requirements on matching hits across layers without creating an unnecessarily large number of tracker seeds. To demonstrate how this is related to hit-skipping, suppose

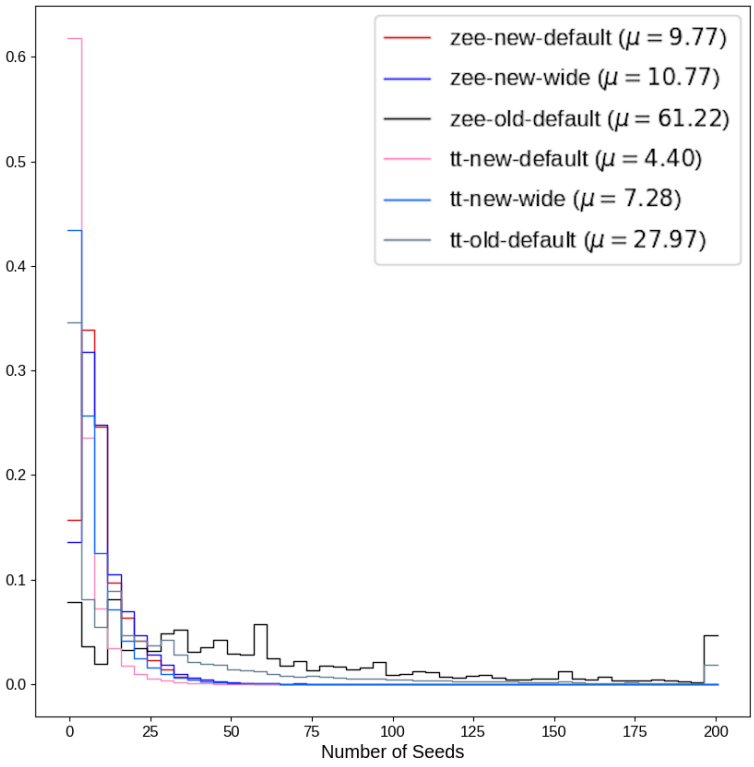

Figure 4.9: Number of ECAL-driven electron seeds produced by the old and new implementation. The new implementation is shown with the `default`(HLT) and `wide` working points. Distributions are normalized to unity, and overflow is grouped into the rightmost bin.

that seeds are generated in three iterations: First, look for quadruplets across four BPIX layers. Second, look for triplets across any combinations of three of the four layers. Finally, look for pairs across combinations of two of the four layers. Let us consider the case where the detector recorded one hit in each BPIX layer and all four hits can match with each other for the purposes of making tracker seeds. The top row of fig. 4.10 demonstrates how the seeding procedure would normally work. There would be a single quadruplet seed, and no pairs or triplets since all four hits have been removed from consideration in subsequent iterations. This quadruplet is then

compared with some SC to make an electron seed. We require that there be three matched hits for triplets and quadruplets, and just two for pairs. During the matching procedure, the hit in BPIX layer 3 (`BPIX3`) fails to match, however it can be skipped and hit 4 matches. Therefore, the tracker seed matches with the SC and proceeds through the rest of the reconstruction chain. However, if hit-skipping is disabled one gets the situation in the middle row of fig. 4.10 where the unmatched hit in layer 3 cannot be skipped and as a result only two hits are matched and no electron seed gets produced. The workaround to recover this seed is to disable the removal of hits between tracker seed construction iterations. As a result, many more seeds are created, as shown in the bottom row of fig. 4.10. However, the seed (now a triplet) of hits in the first, second, and fourth layers now matches and the electron seed is recovered.

From a computational standpoint, this situation is not ideal. Therefore, work was done to add the hit-skipping feature to the new implementation. Adding hit skipping to the new implementation and removing the workaround reduced the number of seeds in $t\bar{t}$ by 41% with the `narrow` matching window sizes and 36% for the `wide` windows. Compared to the original pixel-matching implementation, there were also far fewer seeds, dropping from 12.6 on average to 2.5 for the `narrow` windows and 4.6 for the `wide`. This is achieved without sacrificing performance in efficiency or purity.

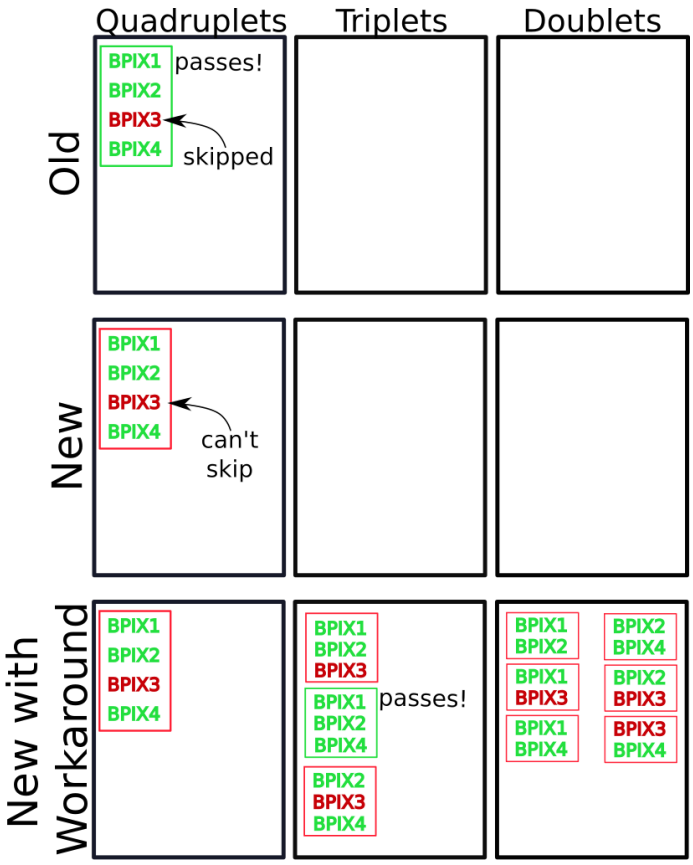

Figure 4.10: Demonstration of how the lack of hit-skipping can lead to the loss electron seeds. Top: Behavior of original matching code with hit skipping. Middle: New code without hit skipping. Bottom: New code with workaround that recovers the seed.

Chapter 5

Measurement of the $t\bar{t}t\bar{t}$ Production Cross Section at 13 TeV

With the discovery in 2012 of the last predicted elementary particle of the SM, the Higgs boson, particle physics has entered uncharted waters. On one hand, a new heavy particle, or particles, may still be produced and observed in one of the many signatures already being explored at the LHC. Alternatively, that new particle may be too heavy or have some other property that makes direct production and observation infeasible, but its existence influences the behavior of SM processes in ways that may be difficult to measure or are very rare. One such rare process is the production of four top quarks.

Featuring high jet multiplicity and up to four energetic leptons, four top quark production is among the most spectacular SM processes that can occur at the LHC. It has a production cross section of $12.0^{+2.2}_{-2.5}$ fb calculated at NLO at 13 TeV center of mass energy[51]. Previous analyses performed by ATLAS[52, 53] and CMS[54–56] have resulted in four top quark production cross section measurements of 28.5^{+12}_{-11} fb from ATLAS and 13^{+11}_{-9} fb from CMS. The goal of this analysis is to improve upon previous results by analyzing a larger data set and utilizing improved analysis methods. This more precise measurement will be used to constrain the top quark Yukawa coupling and masses of heavy mediators in a Two-Higgs Doublet Model.

5.1 Production Mechanisms of $t\bar{t}t\bar{t}$

The production of four top quarks can proceed through both strong and electroweak interactions. Fig. 5.1 shows a few representative Feynman diagrams. As discussed in chapter 2, perturbative calculations of cross sections are performed to a certain order of the relevant coupling constant. For example, processes that only involve the strong interaction can be calculated to $\mathcal{O}(\alpha_s)$, $\mathcal{O}(\alpha_s^2)$ and so on, where the exponent equates to the number of strong vertices in each Feynman diagram included in the calculation. However, one can also consider processes that involve different types of interactions. This leads to mixed order calculations where there are a certain number of QCD vertices, and a certain number of electroweak vertices.

At LHC energies, LO calculations are typically done up to $\mathcal{O}\left(\alpha_s^i \alpha^j\right)$, where i and j are the smallest integers that give a non-vanishing cross section, and α is the electroweak coupling constant. The NLO calculation can involve just adding an additional QCD vertex or external line, leading to $\mathcal{O}\left(\alpha_s^{i+1} \alpha^j\right)$. Doing this improves the accuracy of the total cross section substantially, but the precision of certain parts of the differential cross section will suffer, due to the missing electroweak NLO contribution which contribute preferentially in those areas. These missing contributions make the differential cross section, or rather simulated events based on it, inappropriate for comparison with recorded events. Therefore, significant theoretical work was done to arrive at the "full-NLO" prediction quoted at the beginning of this chapter. The diagrams in fig. 5.1 shows gluon initial state production, also referred to as gluon fusion. Approximately 90% of the $t\bar{t}t\bar{t}$ cross section is from this process, with the remainder accounted for by quark initial state diagrams, including both the up and down valence quarks and heavier sea quarks. The contribution to the total cross section from vector boson and Higgs boson mediated diagrams is small compared to

the QCD contribution. However, as will be discussed in section 5.10.1, the contribution from the Higgs boson mediated diagrams can become significant if the top quark Yukawa coupling is larger than its SM value.

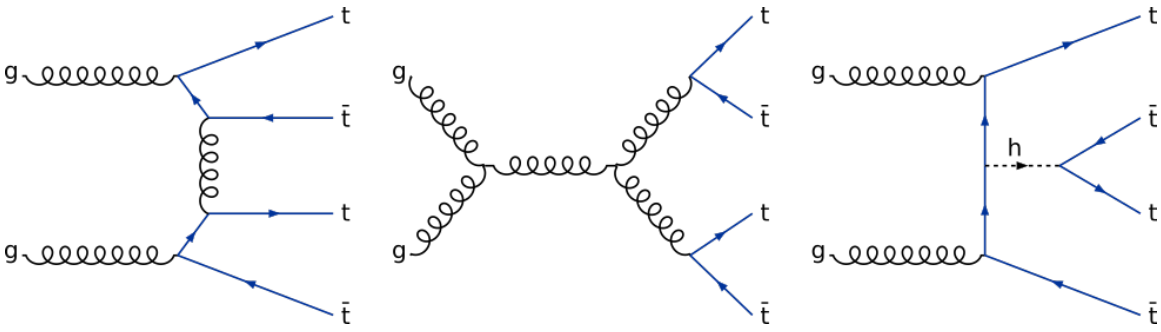

Figure 5.1: Representative leading order Feynman diagrams for four top quark production.

5.2 Decay of the $t\bar{t}t\bar{t}$ System

As discussed in chapter 2, top quarks almost always decay to an on-shell W boson and a bottom quark. Therefore, the final state particles of an event with top quarks are determined by the decay mode of the child W boson, since the bottom quark will always form a jet. Approximately 67% of W bosons decay to lighter flavor (i.e. not top) quark pairs, while the rest will decay to e, μ, and τ leptons in approximately equal probability, each accompanied by its matching flavor anti-neutrino. Electrons and muons can be observed directly while tauons will immediately decay to either a lighter charged lepton plus neutrino, or to hadrons.

For a single top quark, then, the potential final states are:

$$t \to W^+(\to e^+ + \nu_e) + b \quad (11\%)$$

$$t \to W^+(\to \mu^+ + \nu_\mu) + b \quad (11\%)$$

$$t \to W^+(\to \tau^+(\to e^+ + \nu_e + \bar{\nu}_\tau) + \nu_\tau) + b \quad (2\%)$$

$$t \to W^+(\to \tau^+(\to \mu^+ + \nu_\mu + \bar{\nu}_\tau) + \nu_\tau) + b \quad (2\%)$$

$$t \to W^+(\to \tau^+(\to \text{quarks} + \bar{\nu}_\tau) + \nu_\tau) + b \quad (7\%)$$

$$t \to W^+(\to q + \bar{q}') + b \quad (67\%)$$

where the number in parentheses indicates the relative abundance, or branching ratio, of each decay mode.

For four top quarks, the final states are conventionally defined in terms of the number and relative charges of final state leptons (including tauon decay products). This is summarized in fig. 5.2 with the coloring indicating three categories: fully hadronic, single lepton or opposite-sign dilepton[1], and same-sign dilepton or three or more leptons, where lepton here and henceforth should be taken to mean electron or muon unless otherwise noted.

5.3 Analysis Strategy

Four top quark searches for each of these final state categories demand unique analysis strategies due to different event content and vastly different SM backgrounds. In particular, the same-sign dilepton and three or more lepton category benefits from

[1]dilepton: a pair of leptons, here meaning a pair consisting of electrons and muons in any combination.

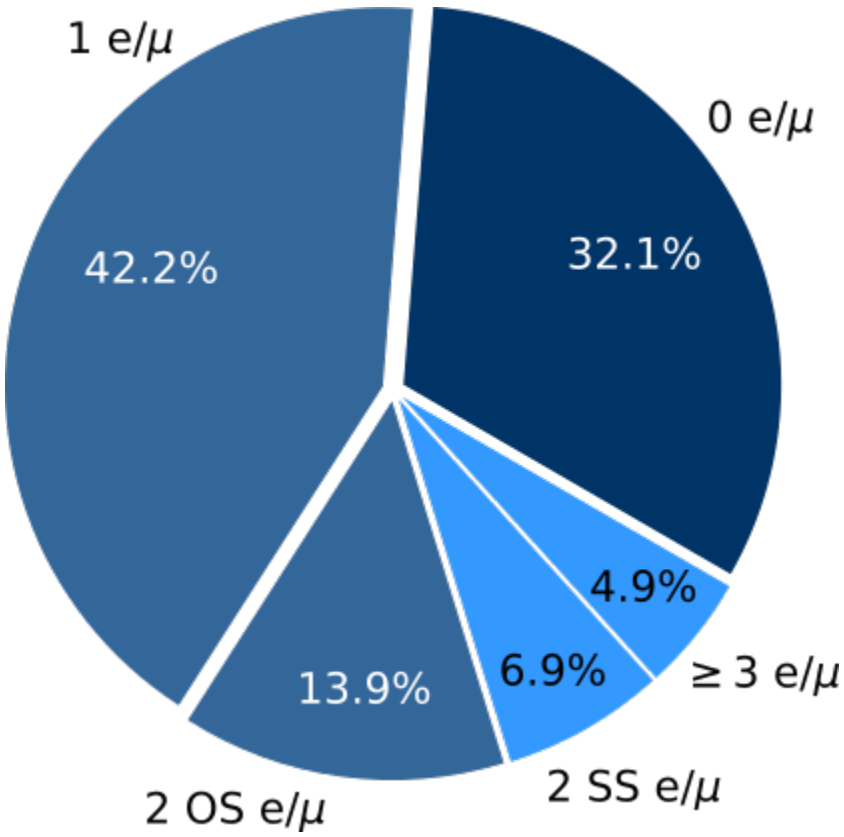

Figure 5.2: Four top final state proportions

a relatively small set of SM backgrounds at the expense of a rather small overall branching ratio. This is the category that is examined in this analysis[2].

The strategy of this analysis is to first craft a selection of events that are enriched in $t\bar{t}t\bar{t}$. This is done by making selections based on relatively simple event quantities such as the number and relative sign of leptons, number of jets, number of jets identified as originating from a bottom quark (b-jets), overall hadronic activity, and missing transverse momentum. A multivariate classifier(MVA) is trained on simulated events within this selection to distinguish $t\bar{t}t\bar{t}$ from background events. This MVA produces a discriminant value that tends towards one for $t\bar{t}t\bar{t}$-like events, and to zero for background-like events. The range of values that this discriminant can take is

[2]The analysis description in this document omits some details for the sake of clarity. However, the analysis documentation[57] contains all the technical details.

divided into several categories, or bins. Each event is placed within one of these bins based on its discriminant value. Finally, a maximum likelihood fit is performed on the distribution of events in the discriminant bins to extract the deviation of the measured distribution from the background-only hypotheses. A statistically significant (and positive) deviation can then be interpreted as evidence of $t\bar{t}t\bar{t}$ production, and can be further processed to find a cross section measurement.

5.4 Data Sets and Simulation

This measurement uses data collected from 2016-2018 with the CMS detector corresponding to a total integrated luminosity of 137.2 fb^{-1}. Events that pass the HLT are divided into roughly disjoint data sets. Of the many of these produced by CMS, this analysis uses:

- DoubleEG: Events that contain at least two energetic electrons
- DoubleMuon: Similar to DoubleEG, except requiring muons instead of electrons
- MuonEG: Crossed channel including events with one muon and one electron

Because the data sets are not completely disjoint, care has been taken to avoid double counting events that may occur in multiple data sets.

Monte Carlo simulation is used extensively to model background and signal processes relevant to this analysis. See chapter 4 for more details on the process of producing simulated events. Samples of simulated Standard Model processes are produced centrally by a dedicated group within the CMS collaboration. The primary samples used in this analysis are listed in table 5.1. Because detector conditions were changed year-to-year, this analysis uses three sets of samples, one for each year.

Table 5.1: Primary simulated samples used in this analyses. Each process is inclusive of all final states unless specified otherwise.

Process	Cross section (pb)
$t\bar{t}t\bar{t}$	0.01197
Drell-Yan: $q\bar{q} \to l^+l^-$, $10 < m_{ll} < 50$ GeV	18610
Drell-Yan: $q\bar{q} \to l^+l^-$, $m_{ll} > 50$ GeV	6020.85
W + jets	61334.9
$t\bar{t}$	831.762
$t\bar{t}W$, $W \to \ell\nu_\ell$	0.2043
$t\bar{t}Z$, $Z \to \ell^+\ell^-$ or $Z \to \nu_\ell\bar{\nu}_\ell$	0.2529
$t\bar{t}H$, $H \nrightarrow b\bar{t}$	0.2710
tZq, $Z \to \ell^+\ell^-$	0.0758
$tbq\gamma$	2.967
$t\bar{t}\gamma$	2.171
$W\gamma$, $W \to \ell\nu_\ell$	405.271
$Z\gamma$, $Z \to \ell^+\ell^-$	123.9
WZ, $Z \to \ell^+\ell^-$, $W \to \ell\nu_\ell$	4.4297
ZZ, $Z \to \ell^+\ell^-$ $\times 2$	1.256
ZZZ	0.01398
WZZ	0.05565
WWZ	0.1651
$WZ\gamma$	0.04123
$WW\gamma$	0.2147
WWW	0.2086

Process	Cross section (pb)
WW, $W \to \ell\nu_\ell$ $\times 2$	0.16975
$tW\ell^+\ell^-$	0.01123
W^+W^+	0.03711
ggH, $H \to ZZ$ $Z \to \ell^+\ell^-$ $\times 2$	0.01181
WH/ZH, $H \nrightarrow b\bar{t}$	0.9561
$t\bar{t}HH$	0.000757
$t\bar{t}ZH$	0.001535
$t\bar{t}ZZ$	0.001982
$t\bar{t}WZ$	0.003884
$t\bar{t}tW$	0.000788
$t\bar{t}tq$	0.000474
$t\bar{t}WH$	0.001582
$t\bar{t}WW$	0.01150

Because the number of jets, N_{jet}, is expected to be an important variable for separating $t\bar{t}t\bar{t}$ from background events, it is important to ensure that the spectrum of the number of jets originating from initial state and final state radiation (ISR/FSR) is accurately modeled. An ISR/FSR jet originates from a gluon that has been radiated from either one of the initial state partons or one of the final state colored particles. This is particularly true for the major background processes of $t\bar{t}W$ and $t\bar{t}Z$. The key observation to performing this correction is that a mismodeling of the distribution of the number of ISR/FSR jets by the event generator will be very similar between $t\bar{t}W/t\bar{t}Z$, and $t\bar{t}$. So by measuring the disparity between data and MC in a selection enriched in $t\bar{t}$, correction weights can be obtained and applied to simulated $t\bar{t}+X$

events.

This correction is obtained as follows. The number of ISR/FSR jets in data is obtained by selecting $t\bar{t}$ events where both child W bosons decayed to leptons and exactly two identified b-jets. Any other jets are assumed to be from ISR/FSR. The weights are then computed as the bin-by-bin ratio of the number of recorded events with a certain number of ISR/FSR jets to the number of simulated events with that number of truth-matched ISR/FSR jets. The results of this measurement for 2016 data and MC are shown in fig. 5.3. The correction is applied by reweighting simulated $t\bar{t}Z$ and $t\bar{t}W$ events with these weights based on the number of truth-matched ISR/FSR jets.

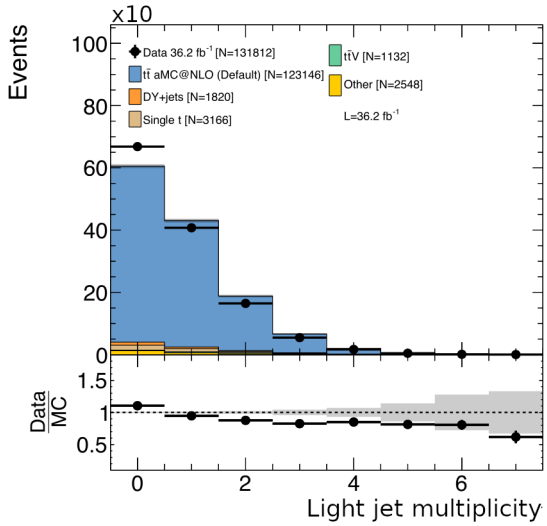

Figure 5.3: Distribution of the number of light jets in a dilepton $t\bar{t}$. The ratio of Data/MC gives a weight to apply to simulated $t\bar{t}W$ and $t\bar{t}Z$ events.

The number of b-tagged jets is also expected to be an important variable for selecting $t\bar{t}t\bar{t}$ events. Therefore, the flavor composition of additional jets in simulation should also be matched to data. Specifically, there has been an observed difference between data and simulation in the measurement of the $t\bar{t}b\bar{b}/t\bar{t}jj$ cross-section ratio[58]. To account for this, simulation is corrected to data by applying a scale factor of 1.7 to

simulated events with bottom quark pairs originating from ISR/FSR gluons. These events are also given a 40% systematic uncertainty on their weights to be consistent with the uncertainties on the ratio measurement.

5.5 Object Definitions

This section describes the basic event constituents, or objects, that are considered in this analysis. The choice of the type and quality of these objects is motivated by the final state content of $t\bar{t}t\bar{t}$ events. The objects are electrons, muons, jets, b-jets, and missing transverse momentum. Each of the objects has dedicated groups within the CMS collaboration that are responsible for developing accurate reconstruction and identification schemes for them. The Physics Object Groups (POGs) make identification criteria, or IDs, available for general use in the collaboration. Many analyses, including this one, incorporate these POG IDs into their own particular object definition and selection. This analysis applies additional criteria to define analysis objects. In the case of leptons, two categories are defined: tight and loose, where the former must satisfy more stringent selection criteria than the latter.

5.5.1 Electrons

Electrons are seen in two parts of the CMS detector: the tracker, and the electromagnetic calorimeter. After an electron candidate has been formed by matching an energy deposit in the ECAL with an appropriate track, it is evaluated in one of a variety of schemes to determine the probability that it is from a genuine electron vs a photon, a charged hadron, or simply just an accidental reconstruction from unrelated hits. For this analysis, only electrons with $|\eta| < 2.5$, i.e. within both the tracker and ECAL acceptance, are considered.

The particular scheme to determine the quality of an electron candidate employed for this analysis is the MVA ID[59–61] developed by the EGamma POG. The MVA uses shower-shape variables, track-ECAL matching variables, and track quality variables to produce a discriminant. Electron candidates are then required to have a discriminant value above a selection cutoff. Multiple cutoffs are provided with the MVA that define tight and loose working points(WPs).

Charge mismeasurement of leptons can result in an opposite-sign dilepton event appearing as a same-sign dilepton event. Because there are potentially large backgrounds with opposite-sign dileptons, steps are taken to remove events with likely charge mismeasurement. In CMS, there are three techniques for measuring electron charge [62]. These are:

1. The curvature of the GSF track
2. the curvature of the general track, obtained by matching the GSF track with general tracks as reconstructed for pions and muons, asking for at least one hit shared in the innermost part (pixels)
3. The SC charge, obtained by computing the sign of the ϕ difference between the vector joining the beam spot to the SC position and the one joining the beam spot to the first hit of the electron track.

A requirement for the highest quality, or "tight", category of electrons used in the analysis is that all three of these methods are required to agree.

The leptons that are desired for defining the event selection are the leptons from the decay of the various top quark's child W bosons. Other leptons, such as those originating in heavy quark decays as part of jets, or from photon pair production are referred to as non-prompt leptons. Photons will sometimes pass through one or more layers of the tracker before undergoing e^+e^- pair-production, resulting in "missing"

inner layer hits for the tracks of the child electrons. Tight electrons are therefore required to have exactly zero missing inner hits. Consistency with having originated from the correct p-p interaction is also considered by applying cuts on the *impact parameter*, or the vector offset between the primary vertex and the track's point of closest approach to it. In particular, there are cuts on d_0, the transverse component of the offset, d_z, the longitudinal component, and $SIP_{3\mathrm{D}}$, the length of the offset divided by the uncertainty of the vertex's position.

5.5.2 Muons

Muons are reconstructed in CMS by matching tracks produced from hits in the muon system to tracks in the tracker. The individual quality of the tracker and muon system tracks as well as the consistency between them are used to define IDs. The Muon POG defines two IDs that are used in this analysis: loose[63], and medium[64]. Only muons within the muon system acceptance $|\eta| < 2.4$ are considered, and the same impact parameter requirements are applied as for electrons. For muons, the probability of charge mismeasurement is reduced by applying a quality requirement on the track reconstruction in the form of a selection on the relative uncertainty of the track's transverse momentum: $\delta p_T(\mu)/p_T(\mu) < 0.2$.

5.5.3 Lepton Isolation

Lepton isolation is a measure of how well separated in ΔR a lepton is from other particles. It is a useful quantity for distinguishing leptons that originate from heavy resonance decays, such as those from W and Z bosons, from leptons that originate as part of a jet. Events from $t\bar{t}t\bar{t}$ and its main backgrounds ($t\bar{t}Z$, $t\bar{t}W$, $t\bar{t}H$) have an especially high number of jets relative to other processes that are typically studied

at the LHC. This prompted the development of a specialized isolation requirement, known as multi-isolation[65]. It is composed of three variables.

The first component is mini-isolation[66], I_{mini}. To understand the utility of I_{mini}, let us first consider the decay of a top quark where the child W boson decays to a lepton. Depending on the momentum of the top quark, the b-jet and the lepton will be more or less separated, with the separation becoming small at high momentum. Because of this, a constant ΔR isolation requirement on the lepton will be inefficient for highly energetic particles. Mini-isolation addresses this by utilizing variable cone size. The size of this cone is defined by

$$\Delta R_{\text{cone}} = \frac{10}{\min\left(\max\left(p_T(\ell), 50\right), 200\right)}$$

With this, I_{mini} is

$$I_{\text{mini}}\left(\ell\right) = \frac{p_T^{h\pm} + \max\left(0, p_T^{h0} + p_T^{\gamma} - \rho\mathcal{A}\left(\frac{\Delta R_{\text{cone}}}{0.3}\right)^2\right)}{p_T\left(\ell\right)}$$

where $p_T^{h\pm}$, p_T^{h0}, p_T^{γ} are the scalar sums of the transverse momenta of the charged hadrons, neutral hadrons, and photons, within the cone. Neutral particles from pileup interactions are difficult to separate entirely from neutral particles from the primary interaction. This leads to some residual energy deposition in the calorimeters. The final term in the numerator accounts for this. The ρ is the pileup energy density and $\mathcal{A}$ is the effective area. These are computed using a cone size of $\Delta R_{\text{cone}} = 0.3$ and are scaled by the formula appropriately to varying cone size.

The second variable used in the multi-isolation is ratio of the lepton p_T to the p_T

of a jet matched to the lepton.

$$p_T^{\text{ratio}} = \frac{p_T\left(\ell\right)}{p_T\left(\text{jet}\right)}$$

The matched jet is almost always the jet that contains the lepton, but if no such jet exists, the jet closest in ΔR to the lepton is chosen. The use of p_T^{ratio} is a simple approach to identifying leptons in very boosted topologies while not requiring any jet reclustering.

The third and final variable is the relative transverse momentum, p_T^{rel}. This is the magnitude of the matched lepton's momentum transverse to the matched jet's momentum and then normalized by the jet's momentum:

$$p_T^{\text{rel}} = \sqrt{|\vec{\ell_T}|^2 - \frac{\left(\vec{\ell_T} \cdot \vec{j_T}\right)^2}{|\vec{j_T}|^2}}$$

where $\vec{\ell_T}$ and $\vec{j_T}$ are the 2-component transverse momentum vectors for the lepton and jet, respectively. This helps recover leptons that are accidentally overlapping with unrelated jets.

The multi-isolation requirement is fulfilled when the following expression involving these three variables is true.

$$I_{\text{mini}} < I_1 \wedge \left(p_T^{\text{ratio}} > I_2 \vee p_T^{\text{rel}} > I_3\right)$$

The logic behind this combination is that by relaxing the mini-iso the efficiency of the prompt lepton selection can be improved. The increase in fakes that comes from the relaxation is compensated for by the requirement that the lepton carry the major part of the energy of the corresponding jet, or if not, the lepton may be considered

as accidentally overlapping with a jet. The three selection requirements, I_1, I_2, and I_3, are tuned individually for electrons and muons (table 5.2, table 5.3), since the probability of misidentifying a jet as a lepton is higher for electrons than muons[67]. After tuning, the selection efficiency for prompt leptons is 84-94% for electrons and 92-94% for muons, and the non-prompt efficiency is 8.1% for electrons and 2.1% for muons.

Table 5.2: Isolation requirements used for 2016

	loose ℓ	tight(e)	tight (μ)
I_1	0.4	0.16	0.12
I_2	0.0	0.76	0.80
I_3	0.0	7.2	7.2

Table 5.3: Isolation requirements used for 2017 and 2018

	loose ℓ	tight(e)	tight (μ)
I_1	0.4	0.11	0.07
I_2	0.0	0.74	0.78
I_3	0.0	6.8	8.0

The multi-isolation is used with other quality criteria to define two categories of each flavor of lepton, tight, and loose. The selections for each of these categories is detailed in table 5.4.

Table 5.4: Summary of lepton selection

	μ-loose	μ-tight	e-loose	e-tight
Identification	loose ID	medium ID	loose WP	tight WP
Isolation	loose WP	μ tight WP	loose WP	e tight WP
d_0 (cm)	0.05	0.05	0.05	0.05
d_z (cm)	0.1	0.1	0.1	0.1
SIP_{3D} (cm)	-	< 4	-	< 4
missing inner hits	-	-	≤ 1	$= 0$

5.5.4 Jets

As discussed in chapter 4, jets are reconstructed from particle flow candidates that were clustered with the anti-kt algorithm with a cone size of $\Delta R < 0.4$. To be considered for inclusion in analysis quantities like N_{jets}, jets must possess a transverse momentum $p_T > 40$ GeV and be within the tracker acceptance $|\eta| < 2.4$. To further suppress noise and mis-measured jets, additional criteria are enforced. For the 2016 data, jets are required to have

- neutral hadronic energy fraction < 0.99
- neutral electromagnetic energy fraction < 0.99
- charged hadron fraction > 0
- charged particle multiplicity > 0
- charged EM fraction < 0.99

For 2017 and 2018, an adjusted set of requirements were applied. These are

- neutral hadronic energy fraction < 0.9

- neutral electromagnetic energy fraction < 0.9
- charged hadron fraction > 0
- charged particle multiplicity > 0

From all jets that pass the stated criteria, a critical variable is calculated that will be used extensively in the analysis, $H_T \equiv \sum_{\text{jets}} p_T$.

5.5.5 B-Jets

Hadrons containing bottom quarks are unique in that they typically have a lifetime long enough to travel some macroscopic distance before decaying, but still much shorter than most light-flavor hadrons. This leads to bottom quarks producing jets not originating at the primary vertex but at a displaced vertex. The displaced vertex will typically be a few millimeters displaced from the primary vertex. One of the critical roles of the pixel detector is to enable such precise track reconstruction that the identification of these displaced vertices can be done reliably. This identification of *b-jets* is done by feeding details of the displaced vertex, and reconstructed jet quantities into a machine learning algorithm that distills all the information to a single discriminant. Different working points are established along the discriminant's domain to provide reference performance metrics. Generally, a loose, medium, and tight WP are defined which correspond to 10%, 1%, and .1% probabilities, respectively, to mis-tag jets from light quarks as bottom quark jets.

In this analysis, jets that pass all the criteria of the previous section, with the exception that the p_T threshold has been lowered to 25 GeV, can be promoted to b-jets. The `deepCSV` discriminator is used in this analysis at the medium working point[68].

The jet multiplicity, N_{jets}, and H_T both include b-jets along with standard jets, provided that they have $p_T > 40GeV$.

5.5.6 Missing Transverse Energy

As discussed in chapter 4, neutrinos escape CMS undetected and create an imbalance in the visible transverse momentum of the event. Four top quark events considered in this analysis will have at least two neutrinos which makes this imbalance a useful quantity to use in the event selection. The missing transverse energy is found by calculating the magnitude of the vector sum of the transverse component of the momenta of all PF particles. Corrections to this are made in accordance with the recommendations of the CMS MET working group[69].

5.6 Event Selection

Before defining the baseline selection of events, it is good to review what the $t\bar{t}t\bar{t}$ signature is in the same-sign lepton channel.

- Two same-sign leptons, including any combination of electrons and muons.
- Missing transverse momentum due to the two neutrinos associated with the aforementioned leptons through their parent W bosons
- Four b-jets, one from each top quark
- Four jets from two hadronic W decays

This analysis is also inclusive of the three and four lepton case. These are similar to the above except there are incrementally more leptons and neutrinos and fewer jets, although the number of b-jets remains constant. With that in mind, the baseline event selection is the following:

- a pair of tight same-sign leptons
- $N_{\text{jets}} \geq 2$
- $N_{\text{bjets}} \geq 2$
- $\not{E}_T > 50$ GeV
- $H_T > 300$ GeV
- $p_{T,\ell_1} \geq 25\text{GeV}, p_{T,\ell_2} \geq 20\text{GeV}$

In the listing, "ℓ_1" and "ℓ_2" refer to the tight leptons with the highest and second highest p_T, respectively. Additional tight leptons must also have $p_T \geq 20$ GeV to count towards N_{lep}.

Events that contain a third lepton passing the loose ID that makes a Z boson candidate with one of the two same-sign leptons are rejected. A Z-boson candidate is formed by an opposite-sign, same-flavor pair of leptons whose invariant mass lies within 15 GeV of the Z boson mass. Low mass resonances are also rejected by applying similar criteria except for the invariant mass being smaller than 12 GeV. However, if the third lepton passes the tight requirements and also creates a Z-boson candidate and has a transverse momentum larger than 5 GeV for muons or 7 GeV for electrons, then the event passes the "inverted Z-veto" and is instead placed into a dedicated $t\bar{t}Z$ control region called CRZ.

If additional tight leptons do not form a Z candidate and have transverse momentum of at least 20 GeV, then they contribute to the lepton count for the event, N_{lep}.

Events that pass the baseline selection and do not get discarded or placed into CRZ are divided into several *signal regions*. There are two approaches used in this analysis for defining these signal regions.

The first approach, called cut-based, is to categorize the events based on the number of leptons, jets, and b-jets. These regions are described in fig. 5.4. In the

cut-based analysis, an additional control region was employed to help constrain the contribution of $t\bar{t}W$ called CRW.

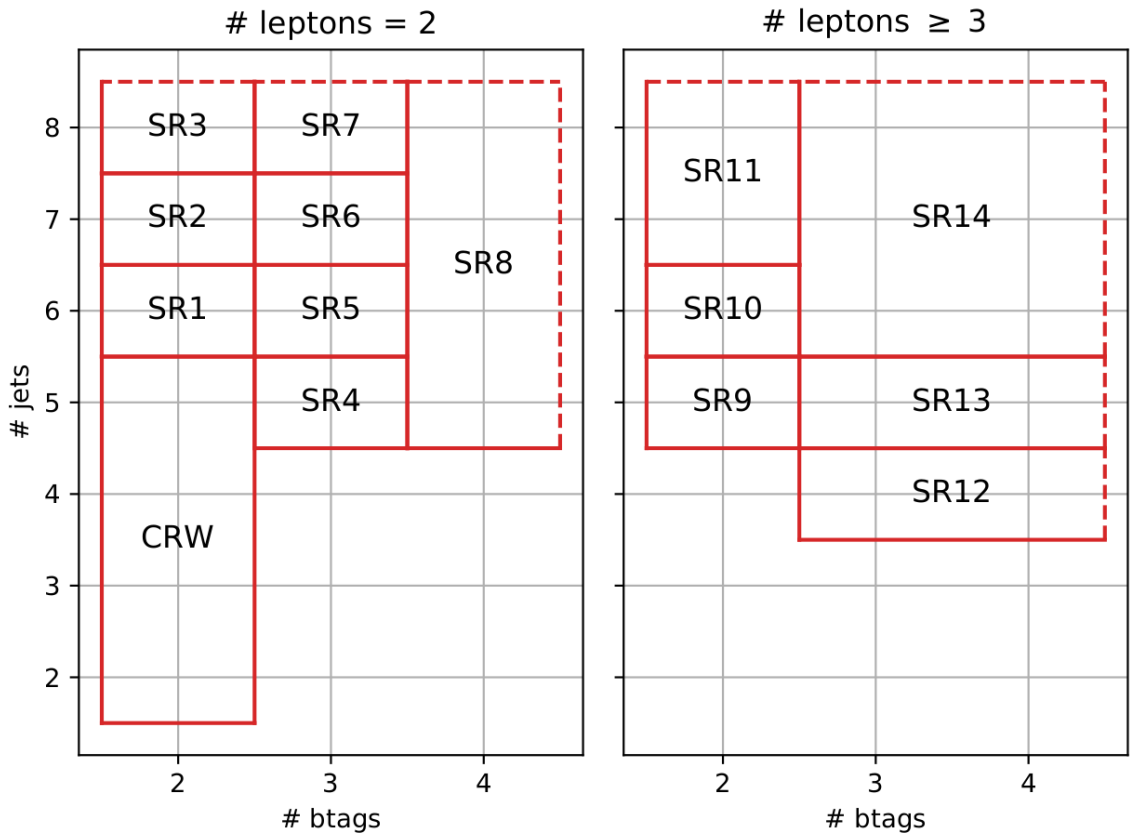

Figure 5.4: Signal and control region definitions for the cut-based analysis.

The other approach for defining the signal regions is to use an MVA. In this analysis, a boosted decision tree (BDT) was used. This BDT used an expanded set of event information, relative to the cut-based classification, to construct a discriminator that would separate signal, i.e. $t\bar{t}t\bar{t}$, events from all background events. This continuous discriminator value is then discretized into several bins which will each contain events with a discriminator value that lies within the bounds of that bin.

Before the BDT can be used, it must be trained. Due to BDT training being susceptible to overtraining unless a large number of training events are available, a relaxed baseline selection was created to provide additional events for the BDT to

train with. The relaxed selection is:

- $p_{T,\ell_1} > 15$ GeV
- $p_{T,\ell_2} > 15$ GeV
- $H_T > 250$ GeV
- $\not{E}_T > 30$ GeV
- $N_{\text{jets}} \geq 2$
- $N_{\text{bjets}} \geq 1$

Signal events were taken from $t\bar{t}t\bar{t}$ simulated samples and background events were taken to be a mixture of simulated SM background processes scaled to their cross sections as listed in table 5.1. Over 40 event-level variables were considered for the BDT inputs. These included the multiplicities of leptons, jets, and b-jets passing the tight or loose selection criteria, H_T, $\not{E}$, transverse momenta of individual leptons and jets, invariant masses and angular separations of pairings of leading and sub-leading leptons and jets, and the number of W boson candidates defined by jet pairs with invariant mass within 30 GeV of the W boson mass.

Of these, the 19 that were determined to have the most discriminating power by the training routine of TMVA[70] were chosen for further optimization. Additional variables provided no significant increase in discriminating power. This discriminating power is quantified by examining the Receiver Operating Characteristic (ROC) curve. The ROC curve is formed by calculating the signal efficiency and background rejection for different cuts on the discriminator value. Different working points can be defined along this curve, but the discriminator's overall performance can be quantified by calculating the area under the ROC curve (AUC). Of the variables listed above, 19 were chosen to continue optimization.

- (a) $N_{\text{bjets}}

- (b) N_{jets}
- (c) N_b^{loose}
- (d) $\not{E}_T$
- (e) N_b^{tight}
- (f) p_{T,ℓ_2}
- (g) $m_{\ell_1\ell_2}$
- (h) p_{T,j_1}
- (i) p_{T,j_7}
- (j) $\Delta\phi_{l_1 l_2}$
- (k) p_{T,j_6}
- (l) $\max\left(m(j)/p_T(j)\right)$
- (m) N_{leps}
- (n) p_{T,ℓ_1}
- (o) $\Delta\eta_{\ell_1\ell_2}$
- (p) p_{T,j_8}
- (q) H_T^b
- (r) p_{T,ℓ_3}, if present
- (s) q_{ℓ_1}

Numeric subscripts indicate ranking in the p_T ordering of the object. For example, p_{T,j_7} is the transverse momentum of the jet with the seventh highest p_T. The distributions of these input variables for signal and background processes are shown in fig. 5.5.

In addition to the input variables, a BDT is described by several parameters internal to the algorithm. These parameters are referred to as *hyperparameters*. These change across different MVA algorithms and even between different implementations of the same algorithm. In the case of BDTs in TMVA, the following hyperparameters were chosen and are listed with their optimized values.

- NTrees=500
- nEventsMin=150
- MaxDepth=5
- BoostType=AdaBoost
- AdaBoostBeta=0.25
- SeparationType=GiniIndex
- nCuts=20
- PruneMethod=NoPruning

An alternative library called `xgboost`[71] was tested for comparison. Optimization of its BDT implementation resulted in the following hyperparameters. Note how this set of hyperparameters is different from those in the TMVA algorithm.

- n_estimators=500
- eta=0.07
- max_depth=5
- subsample=0.6

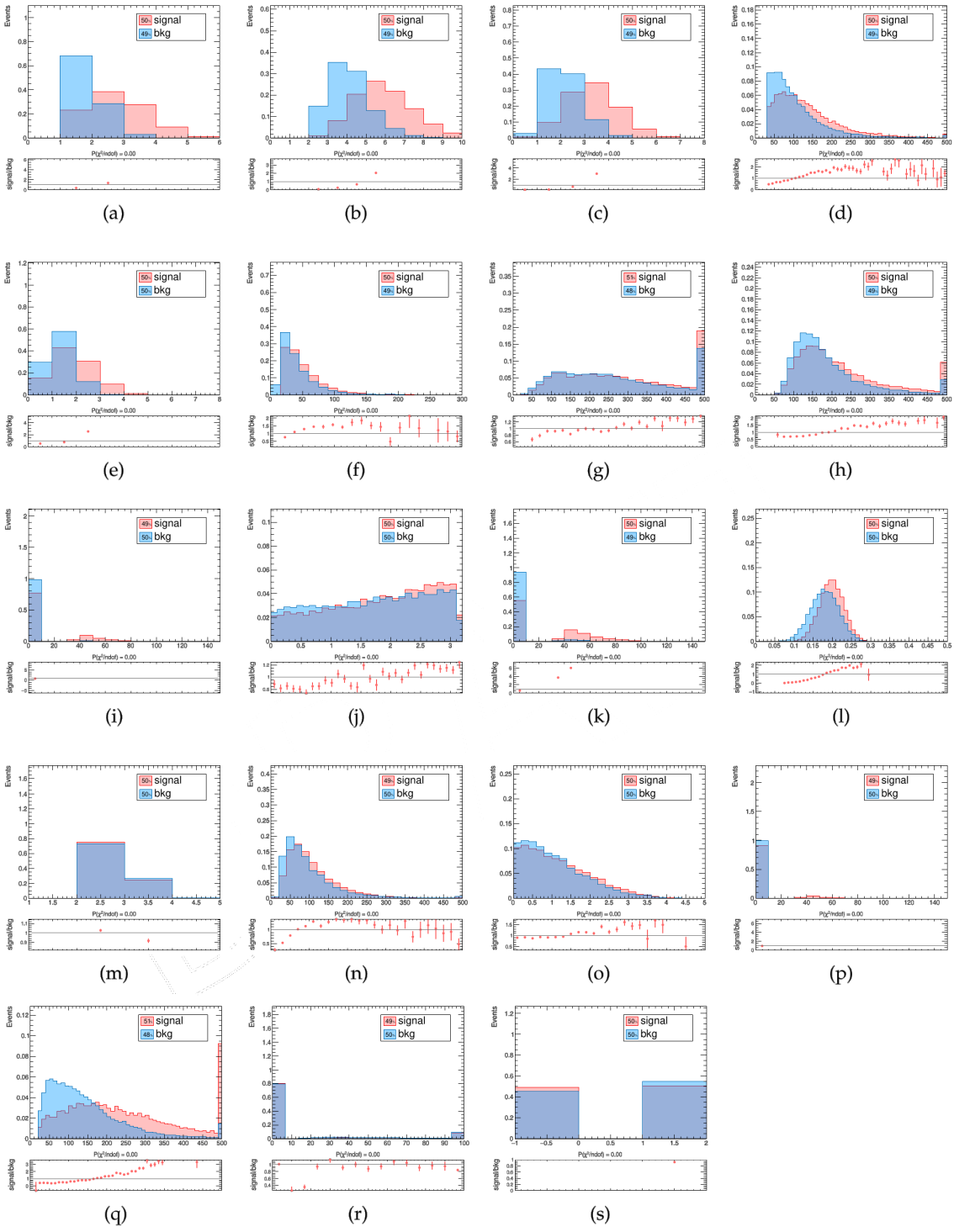

Figure 5.5: Distributions of the input variables to the BDT. All distributions have been normalized to highlight differences in shape.

- alpha=8.0
- gamma=2.0
- lambda=1.0
- min_child_weight=1.0
- colsample_bytree=1.0

Fig. 5.6 shows a comparison between these two optimized BDTs, and fig. 5.7 demonstrates the signal separation achieved by the BDT. The `xgboost` implementation demonstrates clearly superior performance and was therefore selected for use in this analysis.

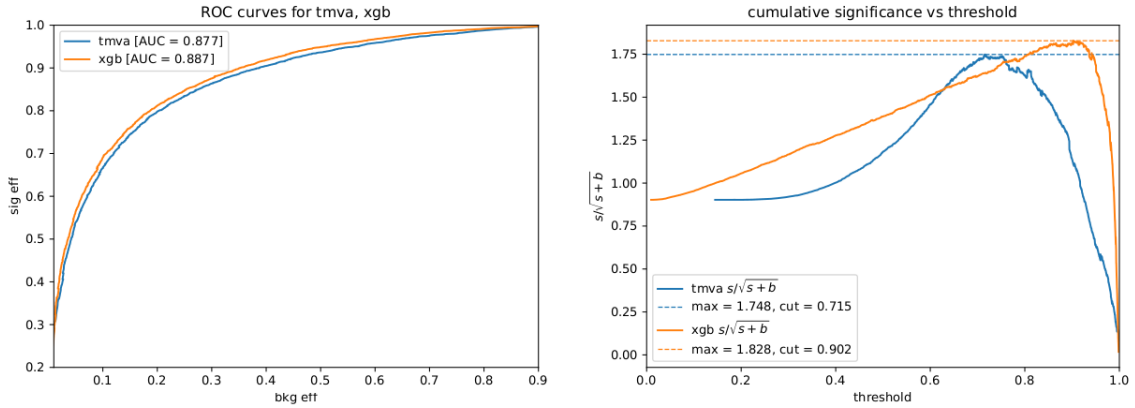

Figure 5.6: Left: ROC curve for TMVA and xgboost optimized BDTs. Right: Cumulative significance vs threshold for both BDTs. Cumulative significance is here defined as $\mathrm{sig}/\sqrt{\mathrm{sig}+\mathrm{bg}}$ for all events with discriminant *higher* than the threshold. This metric is a useful estimator of the statistical significance that can be achieved with the BDT.

The analysis that incorporates the BDT discriminant into the signal region definitions is here referred to as the BDT-based analysis. The BDT-based signal regions contain all of the same events as the cut-based signal regions. However, they are distributed into 17 bins based upon the event's discriminant value. The edges of these

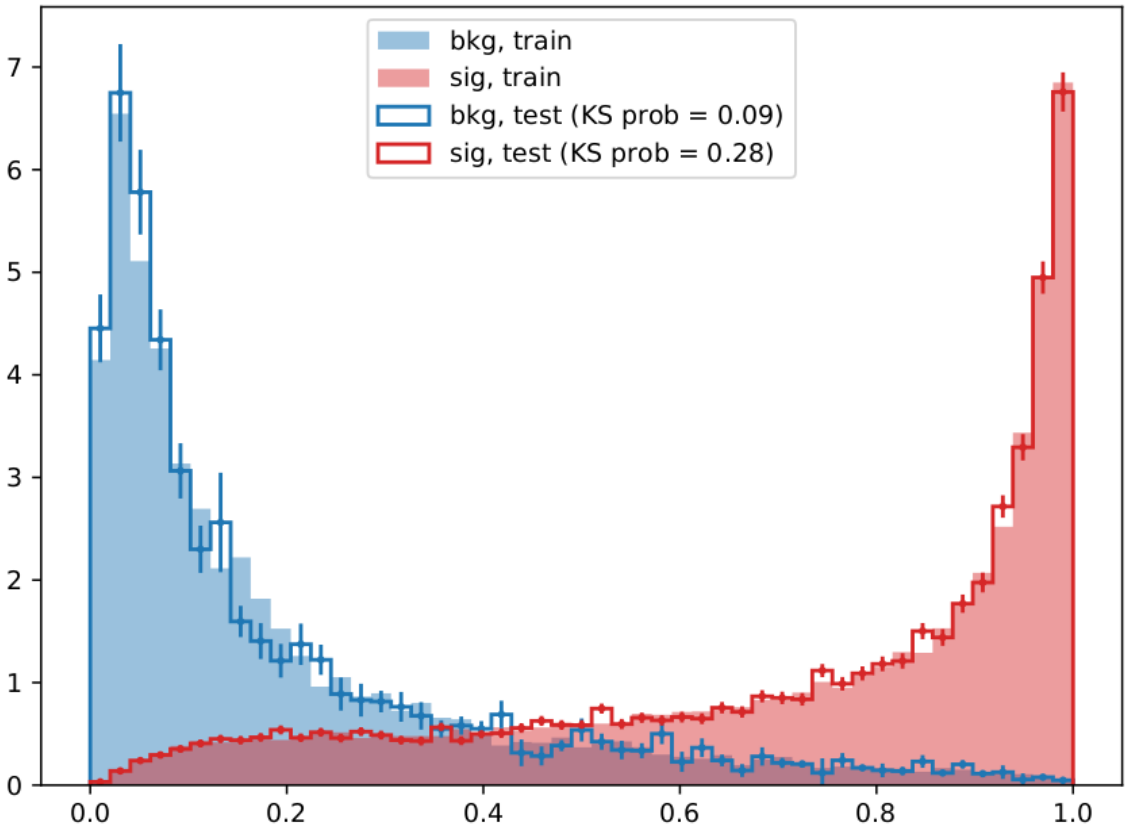

Figure 5.7: Raw discriminant distribution for signal and background for the xgboost optimized BDT. Significant discrepencies between the distributions of the training and testing samples would indicate overtraining.

bins are:

$$[0.0000, 0.0362, 0.0659, 0.1055, 0.1573, 0.2190, 0.2905, 0.3704, 0.4741,$$

$$0.6054, 0.7260, 0.8357, 0.9076, 0.9506, 0.9749, .9884, 0.9956, 1.0000]$$

In addition, there is 1 bin for events in CRZ, giving 18 bins in total. In contrast with the cut-based signal regions, there is no CRW control region in the BDT analysis. In this case, $t\bar{t}W$ is expected to be constrained in the overall fit, as will be discussed in section 5.9.

5.7 Background Estimation

An essential ingredient to making an accurate measurement of any cross section is good estimation of background processes. The backgrounds for this analysis can be divided into two main categories: backgrounds with prompt same-sign lepton pairs, and backgrounds with fake same-sign lepton pairs. Of the backgrounds with genuine same-sign prompt leptons, $t\bar{t}W$ and $t\bar{t}Z$ are estimated from simulation and scaled to data with dedicated control regions. For the BDT-based analysis, only $t\bar{t}Z$ has a dedicated control region. Other processes that produce genuine prompt same-same leptons are taken directly from simulation. Data-driven methods are used to construct the contribution of processes producing fake same-sign lepton pairs in the signal and control regions.

5.7.1 Genuine Same-sign Backgrounds

Of the backgrounds that contain authentic same-sign lepton pairs, the most prominent are events from $t\bar{t}W$, $t\bar{t}Z$, and $t\bar{t}H$. Events from these processes are obtained from simulation and scaled to their theoretical cross sections. For $t\bar{t}W$ and $t\bar{t}Z$ a 40% uncertainty on their cross sections is applied, while for $t\bar{t}H$ a smaller 25% normalization uncertainty is taken due to more constraining measurements on the $t\bar{t}H$ cross section[72].

In addition to the normalization uncertainties, the shape of the distributions of analysis qualities such as H_T, $\not{E}$, and jet multiplicity are studied under different choices of simulation parameters. Considered first was the influence of varying the PDFs used in the event generation within their uncertainty bands. The changes in the resulting observable distributions were consistently smaller than the statistical uncertainty from the limited number of MC events. Based on this, no additional uncertainty is assigned

for PDF variations. Furthermore, the difference between samples produced using LO and NLO calculations were considered as well as the variation in renormalization and factorization scales. The distributions of events generated at LO and NLO are consistent within their renormalization and refactorization uncertainties, indicating the these uncertainties are sufficient to account for missing contributions from higher-order Feynman diagrams. Fig. 5.8 shows a comparison between LO and NLO for $t\bar{t}Z$.

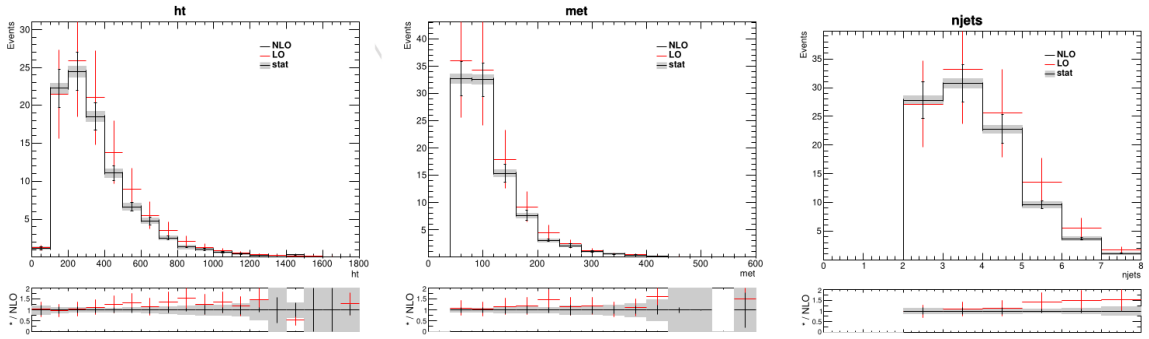

Figure 5.8: Comparison of the LO and NLO kinematics for $t\bar{t}Z$. The error bars on the NLO (black) and LO (red) are the corresponding scale uncertainties. The grey band shows the NLO statistical uncertainty.

Other background processes with smaller contributions include pairs (WZ, ZZ) and triplets (WWW, WWZ, WZZ, ZZZ) of vector bosons, vector boson(s) produced in association with a Higgs boson (HZZ, VH), same-sign W pairs from both single and double parton scattering, and other rare top quark processes (tZq, $t\bar{t}tW$, $t\bar{t}tq$). The contributions from these processes are grouped together into the "Rare" category. Processes that can produce leptons from an unrecognized photon conversion in addition to other prompt leptons are grouped into a category called "$X + \gamma$". These include $W\gamma$, $Z\gamma$, $t\bar{t}\gamma$, and $t\gamma$. Both the "Rare" and "$X + \gamma$" categories are assigned a large (50%) uncertainty on their normalization due to theoretical uncertainties on their respective cross sections. Fig. 5.9 shows the expected contributions of the processes in the Rare category to the signal regions.

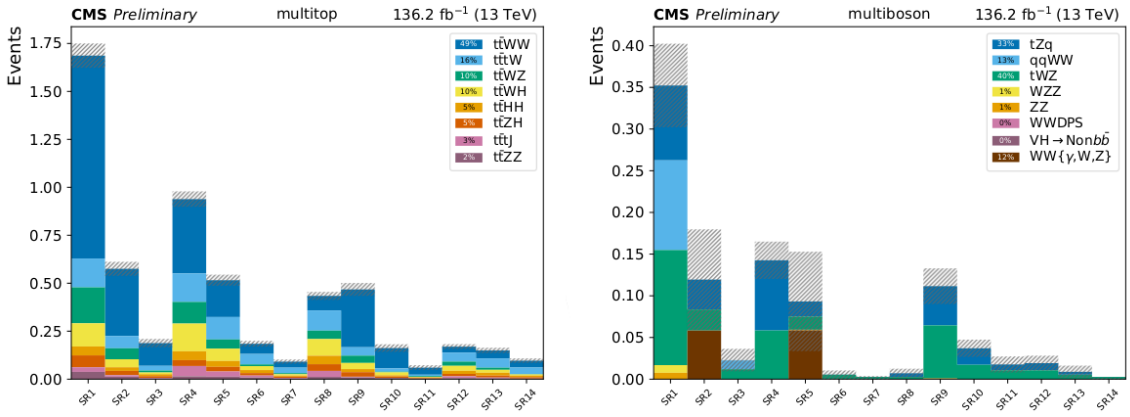

Figure 5.9: Expected yields of rare multi-top (left) and multi-boson (right) processes in the cut-based signal regions.

5.7.2 Fake Same-sign Backgrounds

A same-sign lepton pair can be faked in two ways. The first way is for the charge of a lepton to be mis-measured which flips an opposite-sign lepton pair to a same-sign lepton pair. This rate is quite small, but the large number of SM background events that produce opposite-sign lepton pairs makes it important to consider. The second is the production of "non-prompt" leptons. These non-prompt leptons are called such because they are not produced promptly in the initial parton-parton interaction (at the Feynman diagram level), but rather from the decays of longer-lived particles such as charm and bottom flavored hadrons or from lepton pair-production from energetic photons. The definition of non-prompt leptons also includes charged hadrons misidentified as leptons. Leptons that *are* produced in the initial interaction are called prompt leptons.

The charge misidentification background is estimated by first selecting events in recorded data that pass all signal region selection requirements except for the requirement to have two leading leptons of the same charge. Dimuon events are not considered because the charge misidentification rate for muons is negligible. Selected

opposite-sign events are weighted by the probability for each of the electrons with its specific p_T and η to have its charge misidentified.

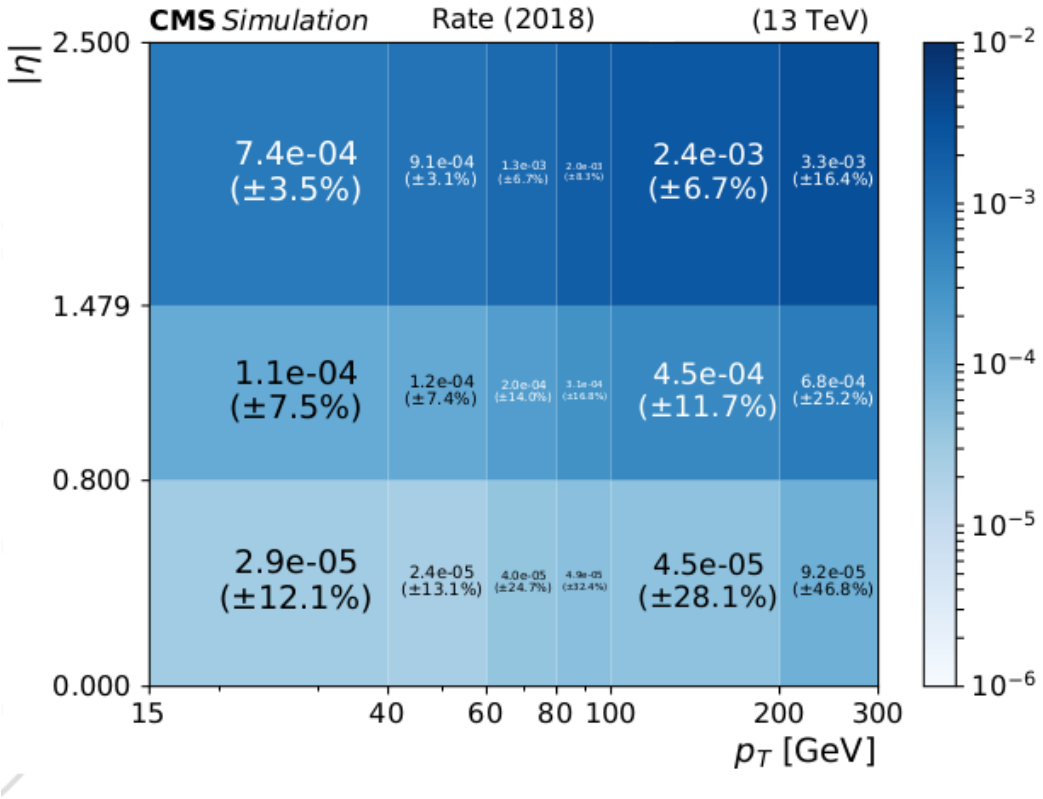

Figure 5.10: Charge misidentification probability for electrons, measured in simulation using 2018 conditions. For electrons with p_T greater than 300 GeV the value shown in th 200-300 GeV bin is applied. The values in 2017 are similar to 2018. These are smaller relative to 2016 due to the installation of the Phase-I tracker upgrade.

This probability, shown in fig. 5.10, is measured in simulated events of $t\bar{t}$ production and the Drell-Yan process. It is then validated by selecting recorded events with tight opposite-sign electron pairs with invariant mass near the Z boson mass and $\not{E} < 50$ GeV. These events are weighted by the charge flip probability to make a prediction of the number of same-sign events. This prediction is compared to recorded events satisfying the same selection except instead requiring a same-sign electron pair. Further, the same-sign selection is applied to the simulated samples used to measure

the flip rate. This is shown in fig. 5.11. The ratio of the number of events in the same-sign region in simulation and data is used as a scale factor to adjust the flip rates. The scale factor is measured to be 1.01, 1.44, and 1.41 for 2016, 2017, and 2018, respectively.

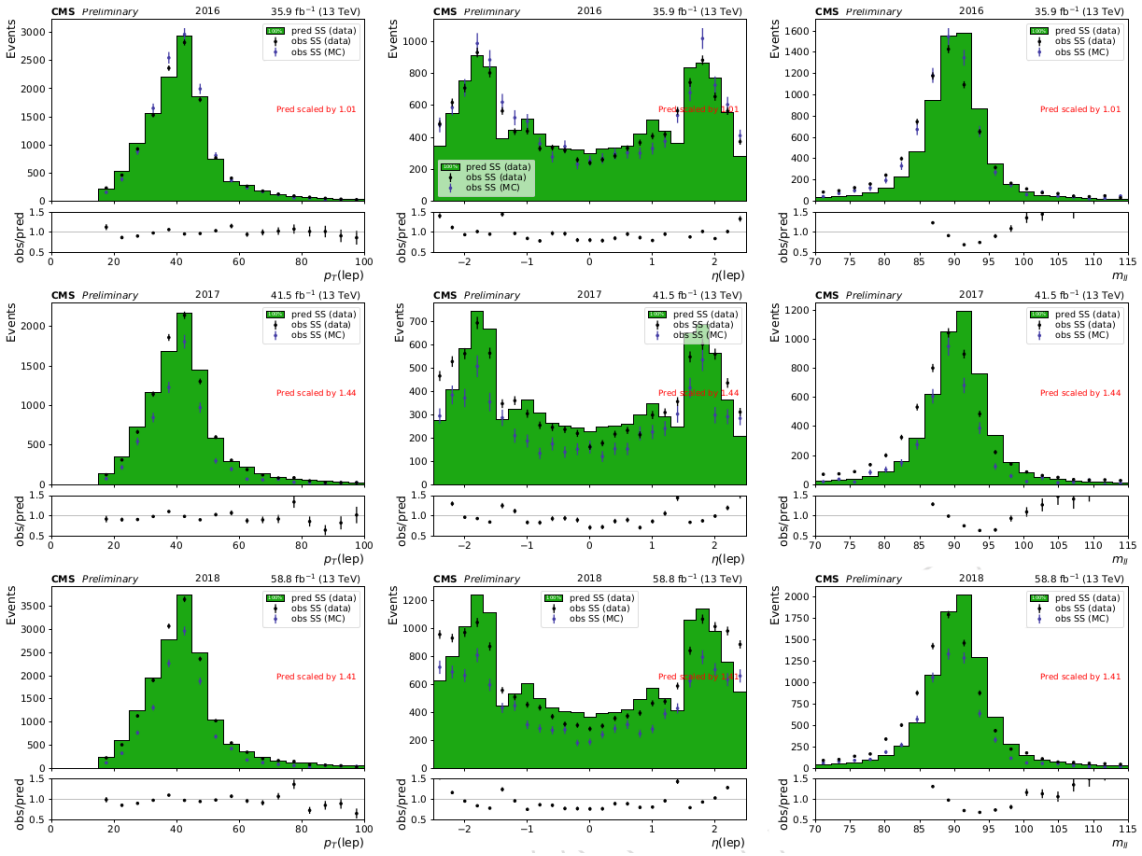

Figure 5.11: Validation of the charge-misidentified lepton estimation. The prediction (green) is obtained by weighting opposite-sign events by the measured flip-rate. The black dots are the observed same-sign yields in data, and the blue dots are the observed same-sign yields in simulation.

The non-prompt background estimation is similar to the charge misidentification background estimation except that the "fake rate", i.e. an estimate of the probability of a non-prompt lepton to pass the tight ID requirements, is measured not in simulation, but in recorded data.

This method utilizes leptons that pass the loose identification criteria listed in

table 5.4. The fake rate is then defined as the probability that a lepton that passes the loose set of requirements also passes the tight set of requirements. The fake rate is measured as a function of lepton flavor, p_T, and η. In order to reduce the fake rate's dependence on the p_T of the lepton's mother parton, the p_T used in the fake rate calculation is adjusted[73] as

$$p_T^{\text{cc}} = \begin{cases} p_T \cdot (1 + \max(0, I_{\text{mini}} - I_1)), & p_T^{\text{rel}} > I_3 \\ \max(p_T, p_T(\text{jet}) \cdot I_2), & \text{otherwise} \end{cases}$$

where p_T^{cc} is called the "cone-corrected" p_T. This can be understood by considering how a lepton's isolation will change with the mother parton's momentum. As the mother parton's momentum increases, the resulting jet becomes more collimated, decreasing the isolation of the lepton. Adjusting the p_T of the lepton to the cone-corrected p_T provides an estimate of the p_T of the mother parton.

The fake rate is measured with a sample of events enriched in non-prompt leptons. The sample consists of events that have a single lepton that passes the loose requirements, at least one jet with $\Delta R(\text{jet}, \ell) > 1$, $\not{E}_T < 20$ GeV, and $M_T < 20$ GeV. The transverse mass, $M_T = \sqrt{2 p_{T,\ell} \not{E}_T \left(1 - \cos\left(\phi_\ell - \phi_{\not{p}_T}\right)\right)}$, is calculated using the transverse momentum of the lepton and the missing transverse momentum of the event. The requirements on $\not{E}_T$ and M_T are intended to suppress the contribution of prompt leptons from Z and W boson decays. Despite this, some events with prompt leptons make it into the selection. This "prompt contamination" of the measurement selection is accounted for by making the same selection on simulated Drell-Yan, W+Jets, and $t\bar{t}$ samples and then subtracting the number of these simulated events from the number of events in the measurement region. The simulated samples are normalized to data using events that satisfy $\not{E}_T > 20$ GeV and M_T between 70 GeV and 120 GeV. Half of the

normalization scale factor is propagated to the fake rate as a systematic uncertainty. After subtracting the prompt lepton contamination, only non-prompt leptons remain. The measurement of the fake rate can then be made using these leptons. Fig. 5.12 shows the fake rate vs cone-corrected p_T for muons and electrons.

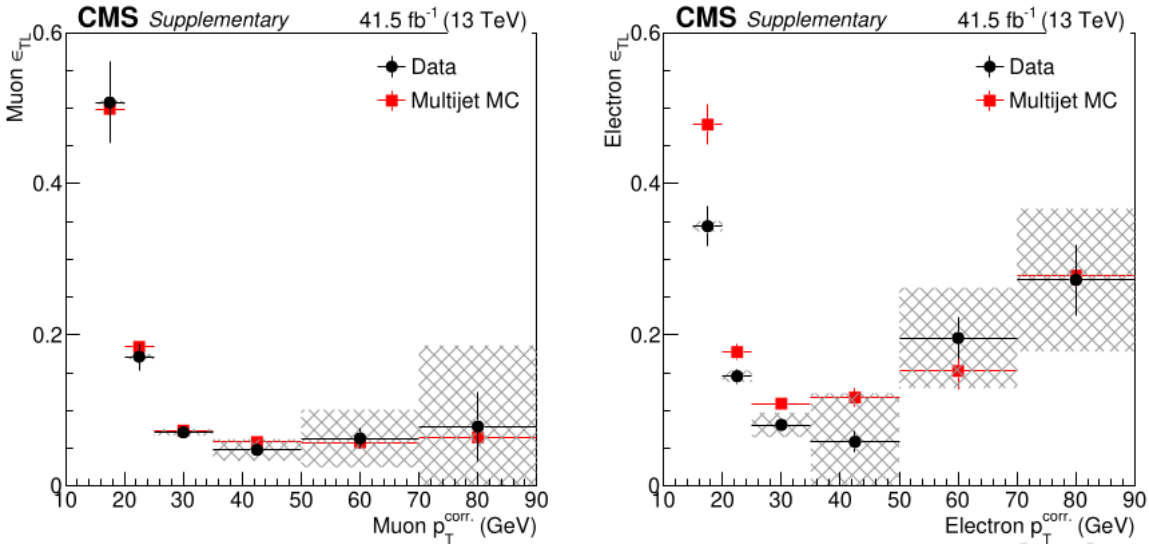

Figure 5.12: Prompt-subtracted fake rates (shown as ϵ_{TL}) versus cone-corrected p_T using 2017 data (black) and 2017 QCD simulation (red) for muons (left) and electrons (right). The shaded band is the systematic uncertainty resulting from the prompt lepton subtraction. This disagreement, especially at low transverse momentum between the prediction and simulation highlights why a data-driven method is necessary.

The prediction of events with non-prompt leptons in the signal region is computed by selecting events that pass the signal region selection except that of the three highest p_T leptons, at most one passes the tight selection while the others pass the loose selection. These events are then weighted multiplicatively by a transfer factor, $\mathrm{tf} = \mathrm{fr}(p_T^{\mathrm{cc}}, \eta, \mathrm{flav})/(1 - \mathrm{fr}(p_T^{\mathrm{cc}}, \eta, \mathrm{flav}))$ for each loose lepton. The transfer factor is

derived as follows:

$$\begin{aligned} \text{fr} &= \frac{N_\text{t}}{N_\text{l}} \\ \text{fr} &= \frac{N_\text{t}}{N_\text{t} + N_\text{l!t}} \\ N_\text{t} &= N_\text{l!t}\frac{\text{fr}}{1-\text{fr}} \end{aligned}$$

where N_t, N_l, $N_\text{l!t}$ are the number of tight, loose, and loose-not-tight leptons, respectively.

The prediction can then be compared with simulation in the application region to validate the method. This is done by comparing the quantity and analysis quantity distributions of the data-driven prediction to simulated events from processes that are most likely to enter the signal region through fake leptons, $t\bar{t}$ and W+Jets. Fig. 5.13 shows a comparison between the prediction from simulation and from the fake rate method. The predictions from the data-driven and simulated estimates are generally within 30% agreement of each other.

5.8 Systematic Uncertainties

Systematic uncertainties originate from experimental or theoretical sources and generally cannot be reduced simply by collecting more data, but can be reduced with refined analysis techniques, precision measurements of the underlying processes, or upgraded detecting equipment. The main experimental uncertainties are:

- **Integrated luminosity**: The integrated luminosity is measured using the pixel counting method and is calibrated via the use of van der Meer scans [74]. Over Run 2, the total integrated luminosity has an associated uncertainty of 2.3-2.5%.

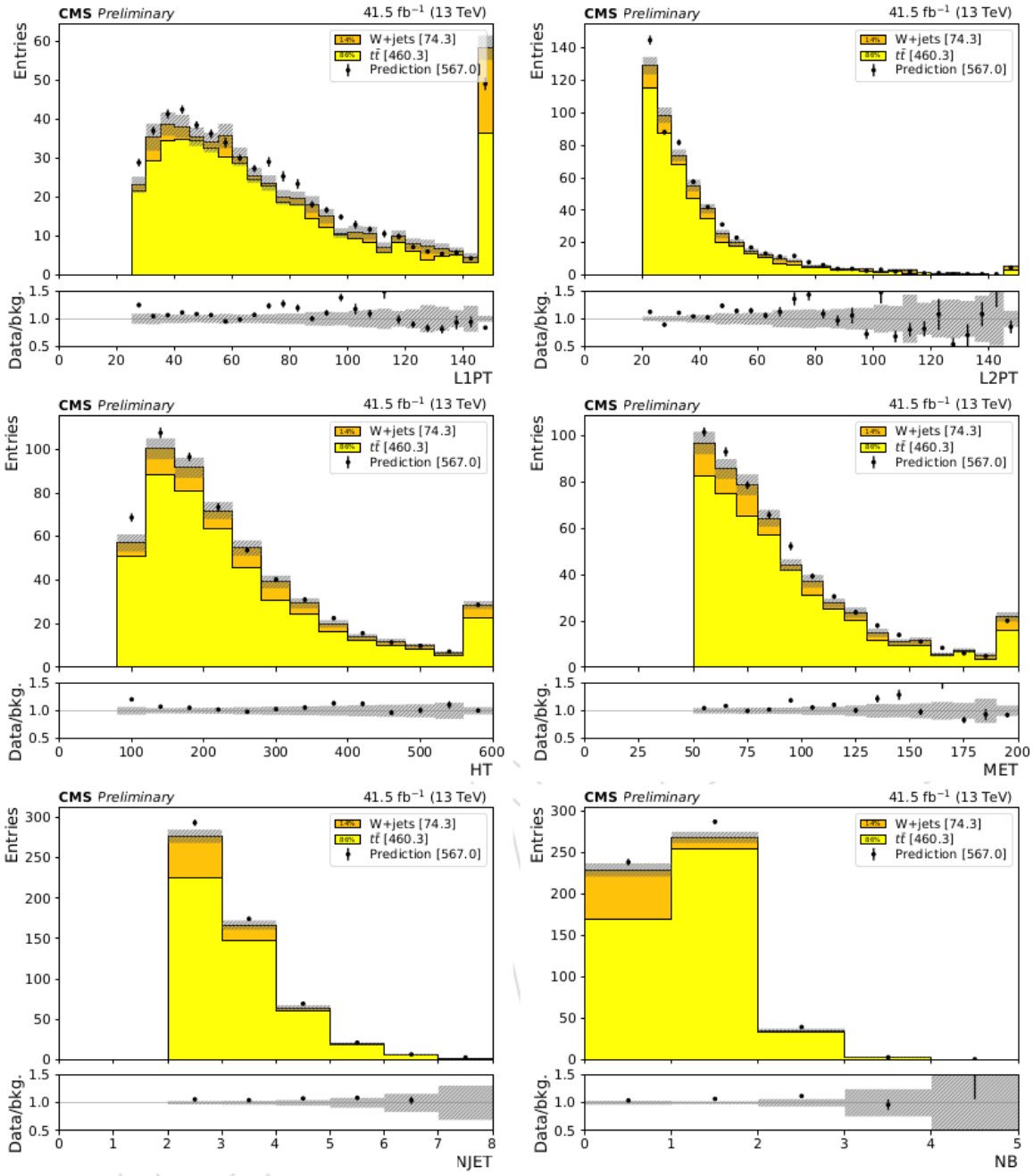

Figure 5.13: Fake rate validation comparing the data-driven fake estimate to an estimate from simulation using 2017 data. Rightmost bins also contain overflow.

- **Jet Energy**: Jet energy is subject to a series of corrections to adjust the raw energy readings from the detector to values that more accurately represent the jet's energy[75]. One of these corrections, the jet energy scale (JES) a has an associated uncertainty from 1-8% depending on the transverse momentum and pseudorapidity of the jet. The impact of this uncertainty is assessed by shifting the jet energy correction for each jet up and down by one standard deviation before the calculation of all dependent kinematic quantities, N_{jet}, H_T, N_{bjet}, and $\not{E}_T$. These uncertainties are propagated into these dependent quantities. Most signal regions show yield variations of 8% when the JES is varied by one standard deviation. The jet energy resolution (JER) is considered as well for the simulated backgrounds and signals. The effect of varying jet energy within their resolution on the event counts in the signal region bins is assessed in the same manner as the JES uncertainty.
- **B-tagging**: The efficiency of identifying jets from bottom quarks is different between simulation and data. A scale factor proportional to is applied to simulated events to account for this. The scale factor has an associated systematic uncertainty The varying the scale factor within this uncertainty results in a change in the $t\bar{t}W$ and $t\bar{t}H$ yields in the baseline selection of roughly 8%, and about 6% for $t\bar{t}Z$.
- **Lepton Efficiency**: Lepton efficiency scale factors [76], which account for differences in the efficiency of the reconstruction algorithm for recorded data and simulation, are applied to all simulated events. They result in event weight uncertainties of approximately 2-3% per muon in event and 3-5% per electron in event.
- **ISR/FSR Reweighting** As previously discussed, $t\bar{t}W$ and $t\bar{t}Z$ events are reweighted to correct the distribution of ISR/FSR jets in simulated $t\bar{t}W$ and

$t\bar{t}Z$ events to the measured distribution in data. An uncertainty equivalent to 50% of the reweighting factor is associated with this procedure. For 2016 data, the reweighting factor was found to be as low as 0.77, resulting in an uncertainty of 15% on the background prediction in the highest N_{jets} signal regions. In 2017 and 2018, the reweighting factor is as large as 1.4, resulting in a similar uncertainty to 2016.

- **Data-driven background estimations**: The non-prompt and charge-misidentification backgrounds estimates have an associated Poisson uncertainty based on the number of application region events used to create the estimate, and this number of events varies dramatically across the individual signal regions. Together with the uncertainties on the fake rate and charge-misidentification rate, this Poisson uncertainty compose the systematic uncertainty on the background estimate. In addition, there is an overall normalization uncertainty applied to the non-prompt background estimate of 30% based on a comparison between the fake estimation described here and an alternative method where the measurement of the fake rate is done "in-situ" in the baseline region[67]. This uncertainty is increased to 60% for electrons with $p_T > 50$ GeV to account for discrepancies in the closure test for those electrons observed in both methods.

Systematic uncertainty also arises from the finite size of simulated data sets. This is handled using the Barlow-Beeston method[77] within the framework of the Higgs Combine tool. The method accounts for the finite precision and associated uncertainties that arise when making estimations with Monte Carlo methods, and is used to handle both the simulated data and the data driven background estimates' statistical uncertainty.

5.9 Signal Extraction and Results

The purpose of this analysis is to search for the presence of $t\bar{t}t\bar{t}$ events within recorded events that fall within the signal regions. To that end, a binned maximum likelihood fit is performed over the signal and control regions using the Higgs Combine tool[78]. The input to the fitting procedure are the number of predicted signal and background events in the control and signal regions as well as the observed number of events. The predicted and measured number of events is shown in the top row of fig. 5.15. The maximum likelihood is found by varying the total number of events from each process where the variation is constrained by the normalization uncertainty on that process. The fit also allows bin-to-bin migration of events constrained by the shape uncertainties for each bin. Additional details on how the fit is performed can be found in [78] and more information on the specifics of the fit for this analysis and checks that were done to ensure the fit behaves properly can be found in the analysis documentation[57]. The post-fit distributions are shown in the bottom row of fig. 5.15. Normalization and shape parameters are changed from their a priori values by the fit. These changes are referred to as pulls and are shown in fig. 5.14.

Using the cut-based signal and control region definitions, the expected (observed) significance is 1.7 (2.5) standard deviations in excess of the background prediction, and for the BDT-based regions it is 2.6 (2.7) standard deviations. The observed (expected) 95% confidence level upper limit on the $t\bar{t}t\bar{t}$ production cross section is 20.04 ($9.35^{+4.29}_{-2.88}$) fb for the cut-based analysis and 22.51 ($8.46^{+3.91}_{-2.57}$) fb for the BDT-based analysis. This is computed using the modified CL_S criterion [79][80], with the profile likelihood ratio test statistic and asymptotic approximation[81]. Adding the $t\bar{t}t\bar{t}$ prediction into the fit allows for a measurement of its cross section. This is found to be $9.4^{+6.2}_{-5.6}$ fb for the cut based analysis and $12.6^{+5.8}_{-5.2}$ fb for the BDT-based analysis. Both measurements are

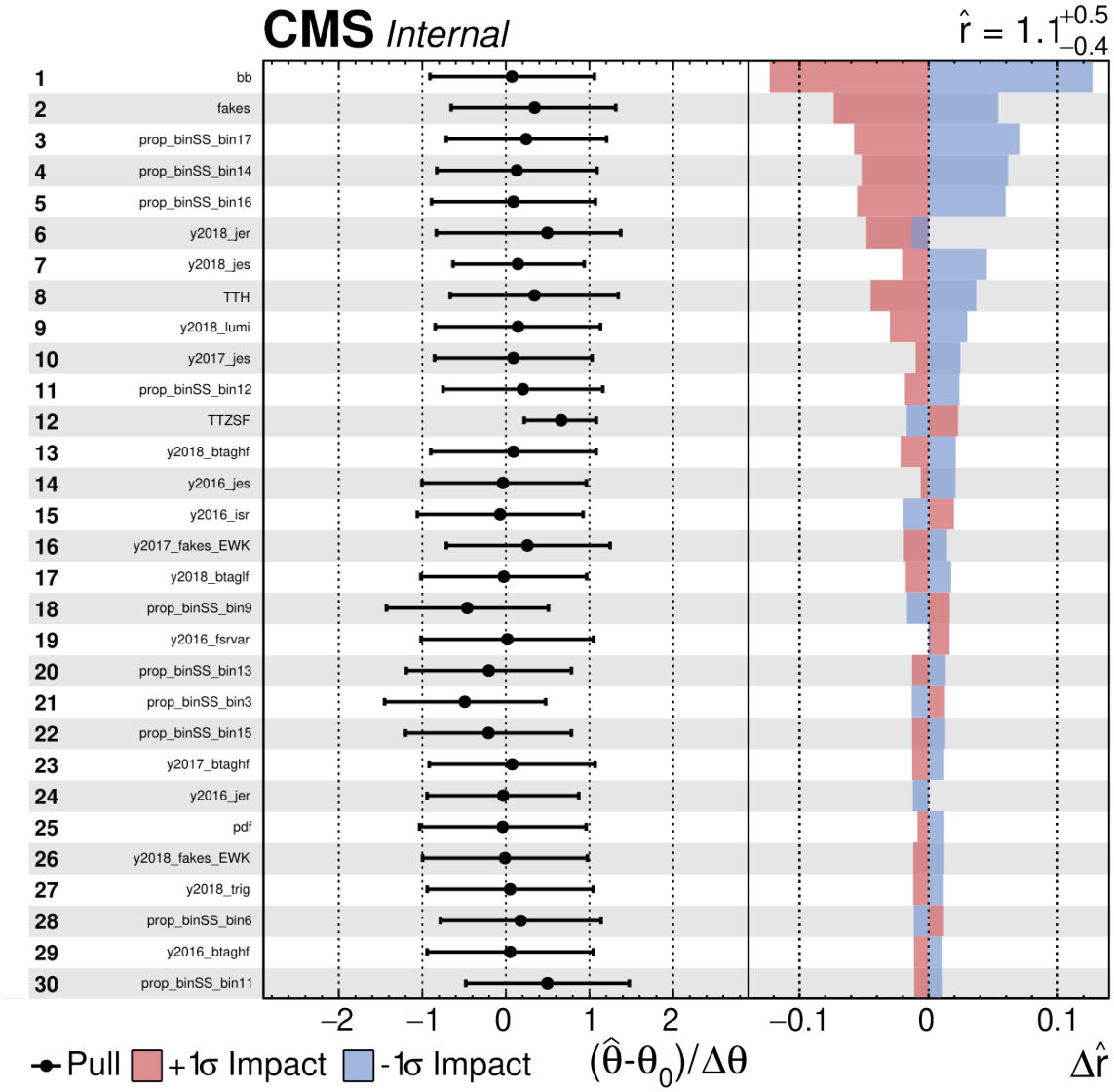

Figure 5.14: Pulls (left) for the top 30 nuisance parameters ranked by the impact (right) of varying them by one standard deviation on the signal strength. Signal strength, $\hat{r}$, is the ratio of the measured four top cross section to its expected value. Rows with names of the form prop_binSS* are the Monte Carlo simulation statistical uncertainty.

consistent with the SM prediction of $12.0^{+2.2}_{-2.5}$ fb at NLO. Due to its superior sensitivity, the BDT-based result is taken as the primary measurement of this analysis and is what is used in the interpretations of the result.

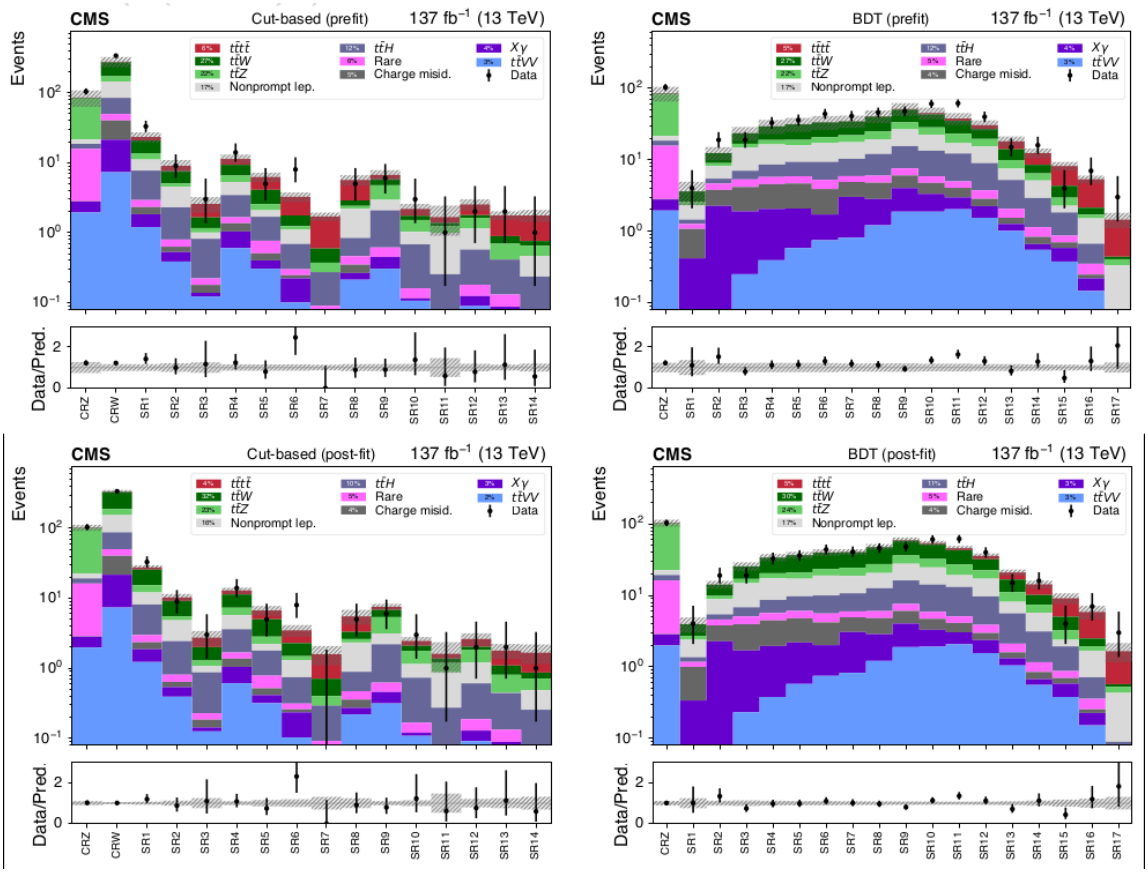

Figure 5.15: Background and signal yields in the control and signal regions before and after performing the maximum likelihood fit.

5.10 Interpretations

The results of this analysis can be interpreted as constraints on other interesting aspects of physics. Considered here are the top quark's Yukawa coupling to the SM Higgs boson, and the Type-II Two Higgs Doublet Model(2HDM).

5.10.1 Top Yukawa Coupling

Standard Model production of four top quarks includes Feynman diagrams with an off-shell Higgs boson mediating the interaction (rightmost diagram of fig. 5.1). The amplitude of these diagrams is proportional to y_t^2. This contributions of these diagrams are added to those of diagrams with no Higgs bosons and squared to give the four top quark production cross section the following dependence on y_t[82].

$$\sigma\left(t\bar{t}t\bar{t}\right) = \sigma_{g+Z/\gamma} + k_t^4\sigma_H + k_t^2\sigma_{\text{int}}$$

where k_t is the ratio of the top quark Yukawa coupling to its SM value. The three terms correspond to the no-Higgs contribution ($\sigma_{g+Z/\gamma}$), the Higgs contribution (σ_H), and the interference between the two processes (σ_{int}). These terms have been calculated at LO. They are:

$$\begin{aligned}\sigma_{g+Z/\gamma} &= 9.997\\ \sigma_H &= 1.167\\ \sigma_{\text{int}} &= -1.547\end{aligned}$$

These terms are calculated at LO, but because the NLO correction to the $t\bar{t}t\bar{t}$ cross section is significant, a correction factor $\sigma^{\text{NLO}}_{t\bar{t}t\bar{t}}/\sigma^{\text{LO}}_{t\bar{t}t\bar{t}}$ is applied to scale the factors to NLO. This results in an NLO cross section of $12.2^{+5.0}_{-4.4}$ fb at $k_t = 1$, consistent with the full NLO calculation of $11.97^{+2.15}_{-2.51}$ fb. This procedure yields the cross section's dependence upon k_t that includes NLO corrections. Another consideration is that $t\bar{t}H$ (H on shell) is a non-negligible background that also scales with y_t, since $\sigma_{t\bar{t}H} \propto \left(y_t/y_t^{\text{SM}}\right)^2$. Therefore, the limit on the $t\bar{t}t\bar{t}$ cross section decreases as y_t/y_t^{SM} grows since the larger

$t\bar{t}H$ contribution accounts for a larger proportion of the observed excess. Fig. 5.16 shows the measured $t\bar{t}t\bar{t}$ cross section as well as its 95% confidence level upper limit and the theoretical prediction of the cross section versus k_t. Comparing the observed upper limit with the central value of the theoretical prediction, we claim a limit of $|y_t/y_t^{\mathrm{SM}}| < 1.7$.

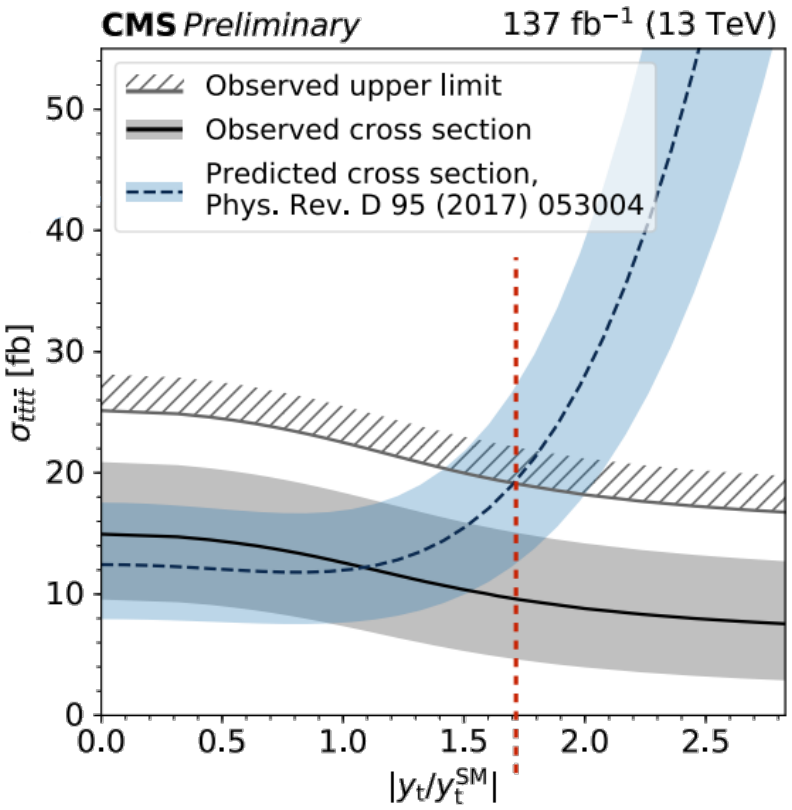

Figure 5.16: Limit on the top quark's Yukawa coupling to the Higgs boson. The blue band is the SM prediction at LO scaled to NLO. The black line is the measured cross section with associated uncertainty bands, taking into account the decreasing cross section measurement as $t\bar{t}H$ grows with increasing y_t as discussed in the text.

5.10.2 Type-II Two Higgs Doublet

As discussed in chapter 2, the Higgs field is introduced as a doublet of complex scalar fields. An interesting Beyond the Standard Model (BSM) theory involves adding an

additional doublet. Theories based on this addition are called Two Higgs Doublet Models (2HDM)[83, 84]. This increases the number of "Higgs" particles from one to five. These include two neutral scalar CP-even particles, h and H, where conventionally h is taken as the lighter of the two. There is also a neutral pseudoscalar, A, and a charged scalar, $H^{\pm}$. This following discussion examines how this analyses can be used to set constraints on the new neutral Higgs particles. Keep in mind that notation has changed slightly. Previously, H was the SM Higgs boson, but in this section h is the SM Higgs boson and H is the additional scalar in the 2HDM model.

The 2HDM model contains two parameters that will be used in this interpretation: α which is the angle that diagonalizes the mass-squared matrix of the scalar particles, and β which is the angle that diagonalizes the mass-squared matrix of the charged scalars and the pseudoscalar[84]. The two parameters, α and β then determine the interactions between the various Higgs particles and the vector bosons as well as the fermions, given the fermions' masses. For this interpretation, 2HDM models of Type II are considered, in which the additional Higgs particles couple strongly to the top quark. In this case, one can impose the "alignment limit", $\sin(\beta - \alpha) \to 0$, forcing the lighter of the two CP even Higgs bosons, h, to have couplings exactly like the SM Higgs boson, while the couplings of H and A to the SM vector bosons vanish. In this limit, production of H and A is predominantly through gluon fusion.

The strategy of this interpretation is to use the same-sign lepton pair final state of the processes shown in fig. 5.17 to place limits on their cumulative cross section, treating $t\bar{t}t\bar{t}$ as a background with its SM predicted cross section. This is done by simulating events and calculating cross sections for the 2HDM processes using the `2HDMtII_NLO` MadGraph model[85] on a grid of points made by varying the mediating particles' masses and $\tan\beta$. The resulting cross section predictions are shown in fig. 5.18.

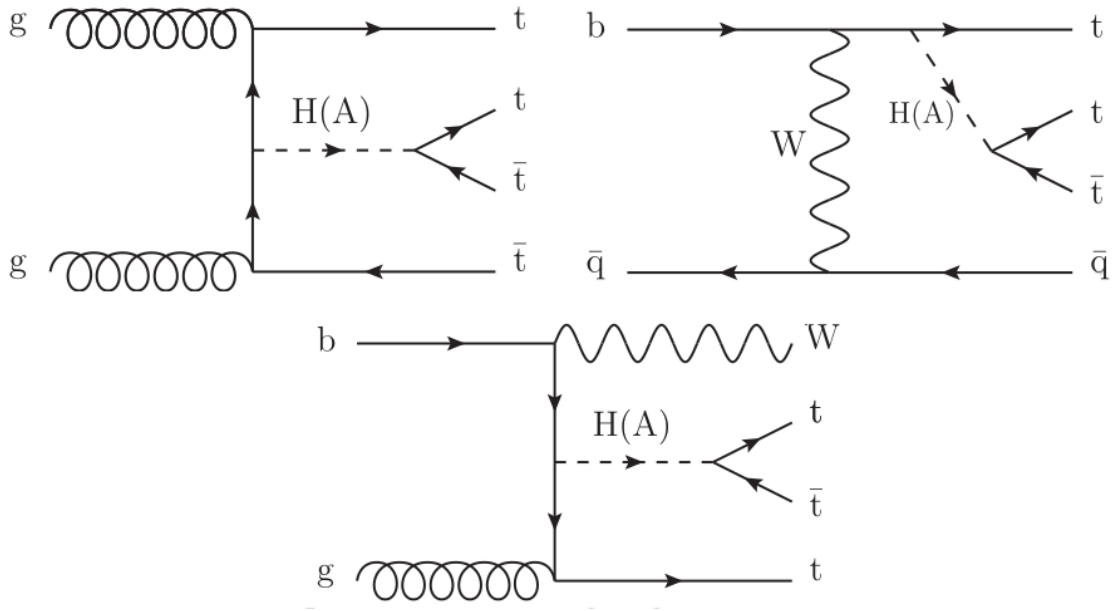

Figure 5.17: Diagrams for heavy scalar (H) and pseudoscalar (A) mediated production of three and four top quark final states. These processes will be referred to as $t\bar{t}H/t\bar{t}A$ (top left), tHq/tAq (top right), and tHW/tAW (bottom)

In general, the kinematic distributions of events originating from a scalar or pseudoscalar mediator will be different. This means that the acceptance, or proportion of events that lie within the signal regions, will be different between the two processes. This would need to be accounted for when placing limits. However, Fig. 5.19 shows a comparison of analysis level observables for the two processes, and the two distributions are similar. In particular, the BDT discriminant distribution has a Kolmogovor-Smirnov test metric of 0.8, indicating consistency within statistical limits. This implies that the acceptance difference between the two processes is small enough to be ignored. For this reason, only scalar samples are used for both processes, and the pseudoscalar results are obtained by scaling the cross section appropriately.

Limits are calculated by placing simulated events from either the H-mediated processes or the A-mediated diagrams into the BDT-based signal regions as previously defined. A fit is performed similarly to the $t\bar{t}t\bar{t}$ measurement except for that the

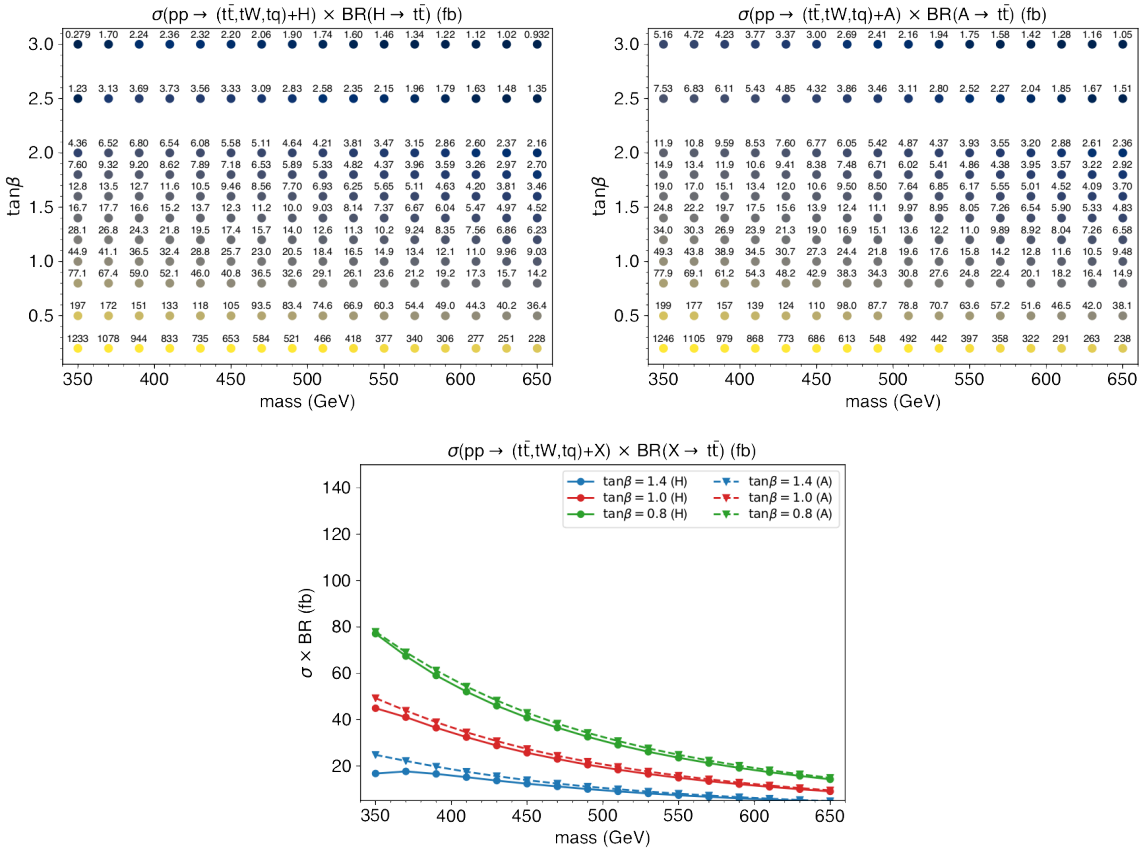

Figure 5.18: Cross sections in units of fb in the plane of $\tan\beta$ vs mediator mass for a heavy scalar boson (top left) and heavy pseudoscalar boson (top right). The bottom plot cotains 1-D projections for both mediators for a few values of $\tan\beta$.

Standard Model four top quark production is treated as a background and it's cross section is treated as a nuisance parameter. This is done for each combination of mediator mass and $\tan\beta$. Points where the 95% CL limit on the cross section is smaller than the predicted cross section are considered excluded. Fig. 5.20 shows the resulting exclusions. At $\tan\beta = 1$, scalar (pseudoscalar) heavy bosons are excluded up to 470 (550) GeV (fig. 5.21).

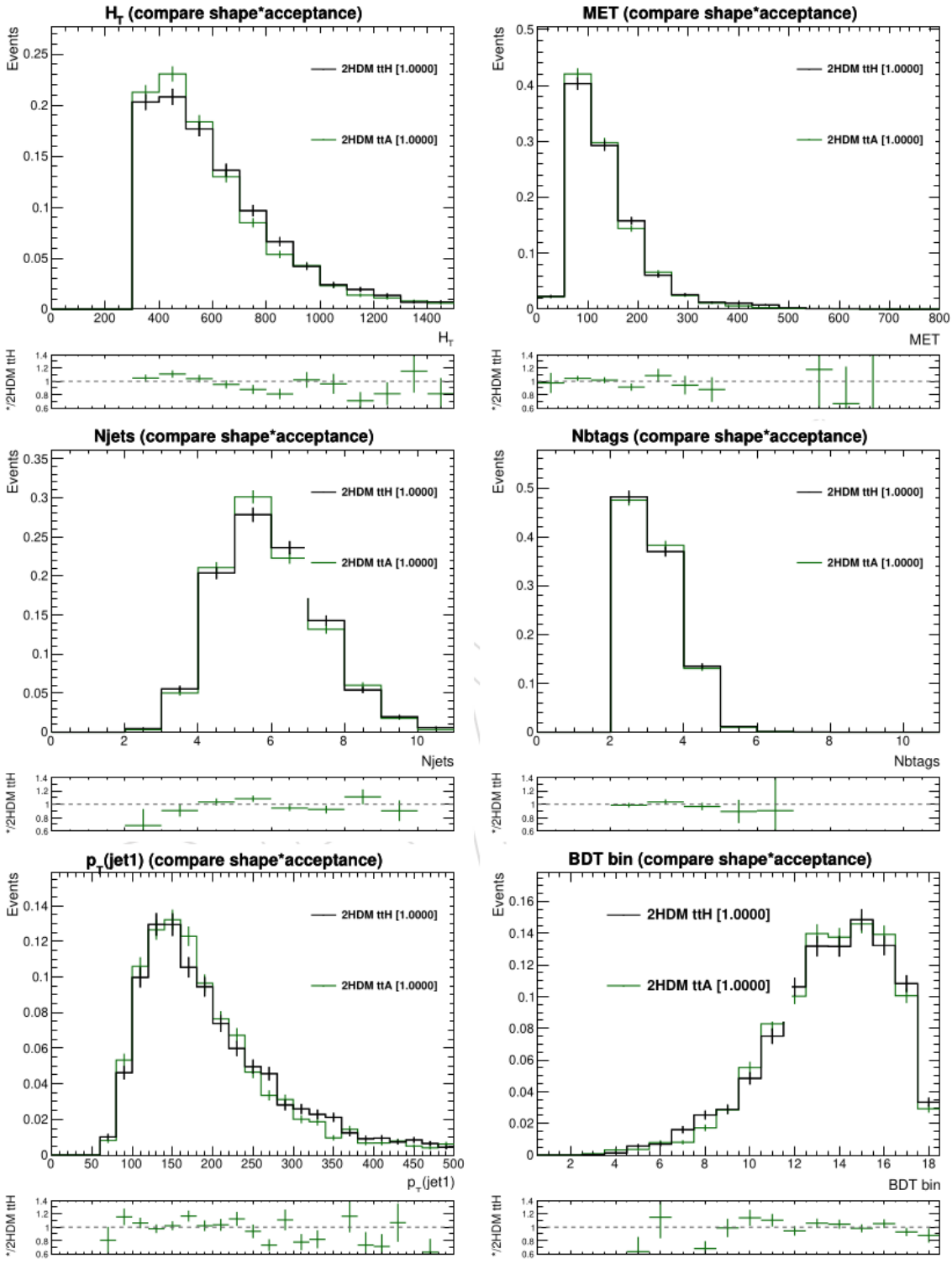

Figure 5.19: Distributions comparing analysis-level observables for the scalar and pseudoscalar processes with both masses set to 450 GeV at $\tan\beta = 1$. The distributions have been divided by their corresponding cross section so both the shape and acceptance of the distributions are comparable.

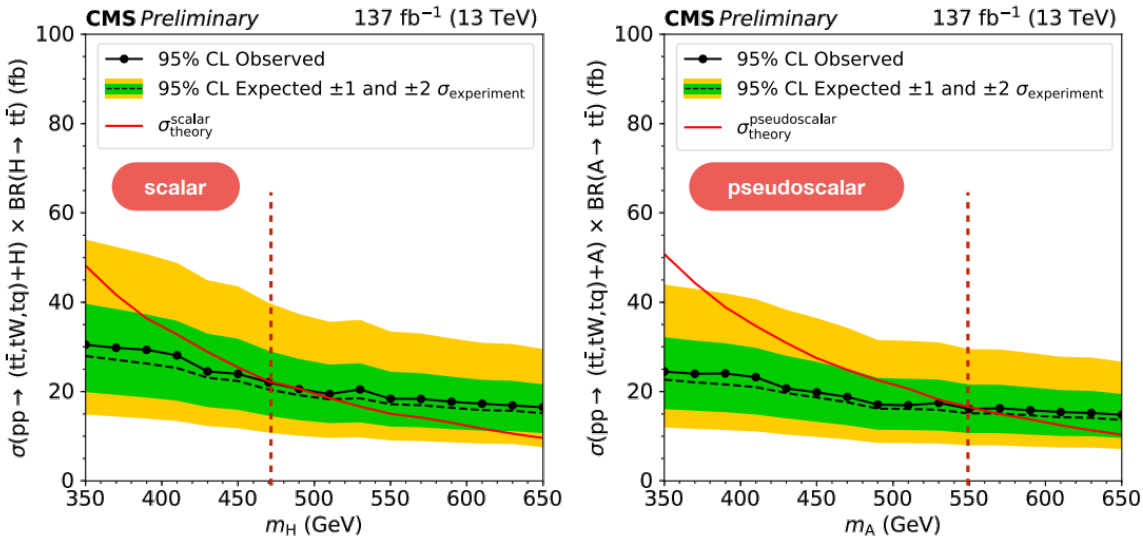

Figure 5.20: Two-dimensional observed and expected exclusions of heavy scalar only (left), pseudoscalar only (right) as a function of the mediator mass and $\tan\beta$.

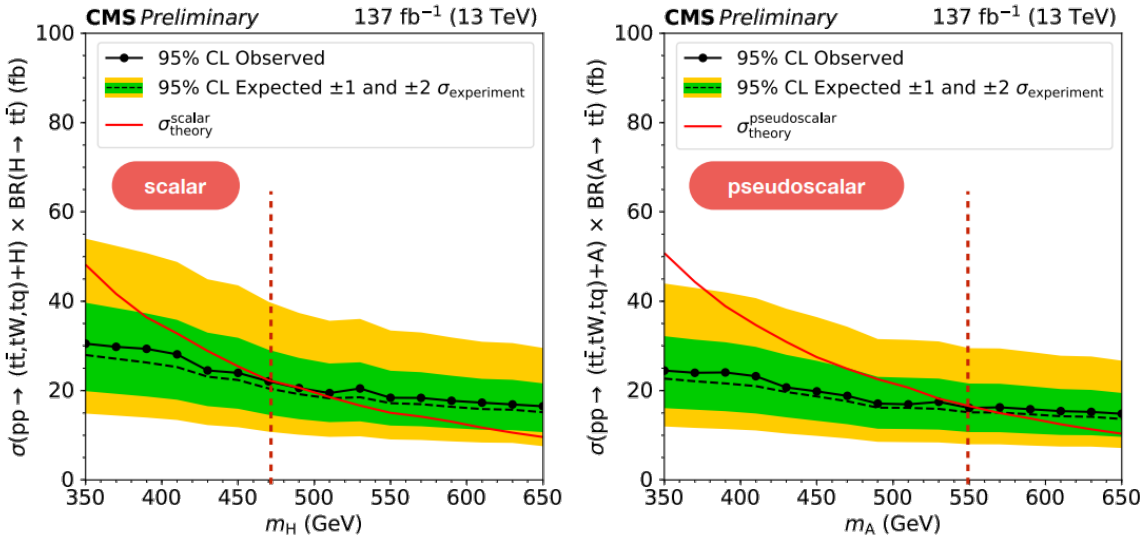

Figure 5.21: Observed and expected limits on heavy scalar (left) and pseudoscalar (right) processes as a function of their respective masses. Here, $\tan\beta = 1$.

Chapter 6

Phase I Silicon Detector Assembly

The CMS Phase I Upgrade project was a successful effort to design and construct an improved detector for Run 2 of the LHC. In particular, both the forward and barrel sections of the pixel detector were replaced with a redesigned and upgraded version to effectively handle the higher instantaneous luminosity conditions of Run 2. The upgraded pixel detector was installed in early 2017 and has operated well for data taking in 2017 and 2018. This chapter will describe contributions made by the team at UNL to the design, testing, and assembly of modules for the forward section of the pixel detector upgrade. The author of this work contributed significantly to the design and construction of the assembly tooling, and wrote the software that controlled that tooling. In addition, the author designed and partially implemented a high performance telescope for future test beam studies.

6.1 CMS Pixel Detector Upgrade

The original CMS pixel detector was designed to record three 3D positions of charged particles as they leave the luminous region as long as they are within $|\eta| < 2.5$. It could do this reliably for bunch crossings coming every 25 ns with an average number of pileup interactions of up to 25, equivalent to an instantaneous luminosity

of 1×10^{34} cm^{-2}s^{-1}. However, increasing the instantaneous luminosity higher than this dramatically reduces the efficiency of the detector due to buffer overruns and sensor degradation from more radiation exposure. Fig. 6.1 demonstrates how the performance suffers as the number of pileup interactions grows.

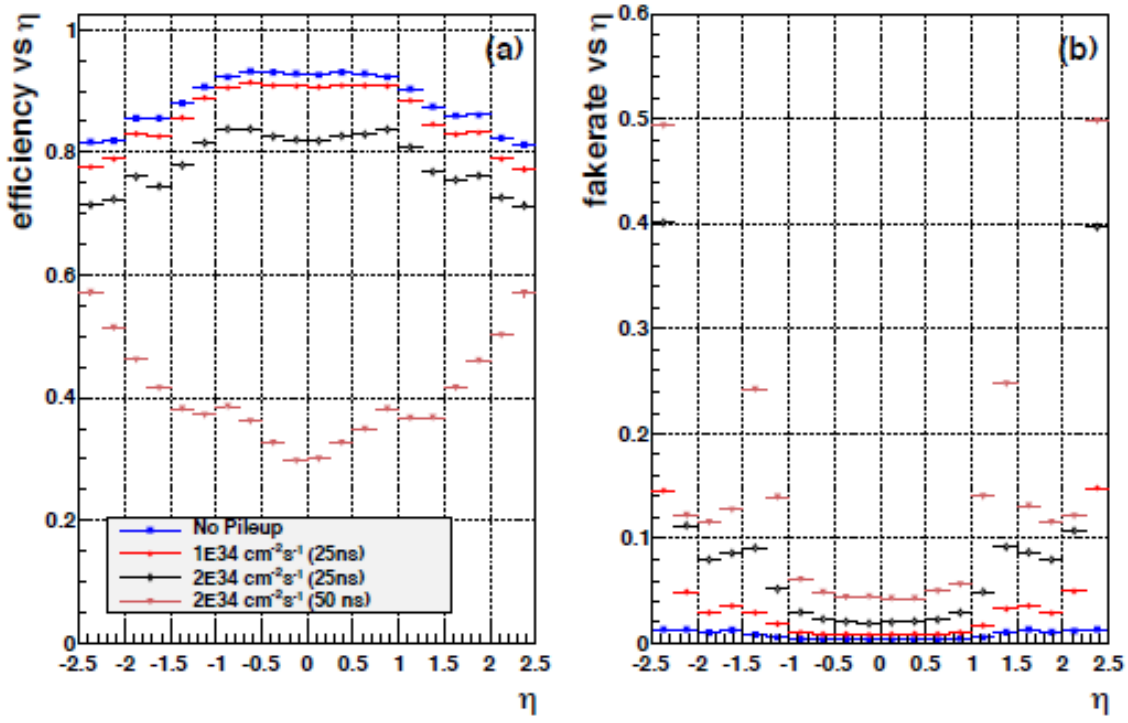

Figure 6.1: Expected performance of the original pixel detector for different beam conditions. The left plots shows the tracking efficiency as a function of pseudorapidity. Note the dramatic loss in efficiency that occurs when moving to 50 ns bunch-crossings while keeping the instantaneous luminosity constant (ie doubling the number of interactions per bunch-crossing). The right plot shows a similar loss of performance as the fake-rate increases as the number of simultaneous interactions increases, especially in the transistion region between the barrel and forward sections of the pixel detector.[86]

To address this problem, a new pixel detector was designed. The new design incremented the number of barrel layers from three to four and the number of forward layers from two to three. It also utilized the new PSI46 readout chip with digital readout, and very low mass construction, important for minimizing the number of radiation lengths in the tracker. Like the original detector, it uses 100μm by 150μm

pixels. Fig. 6.2 shows a comparison between the geometries of the original and upgraded pixel detector.

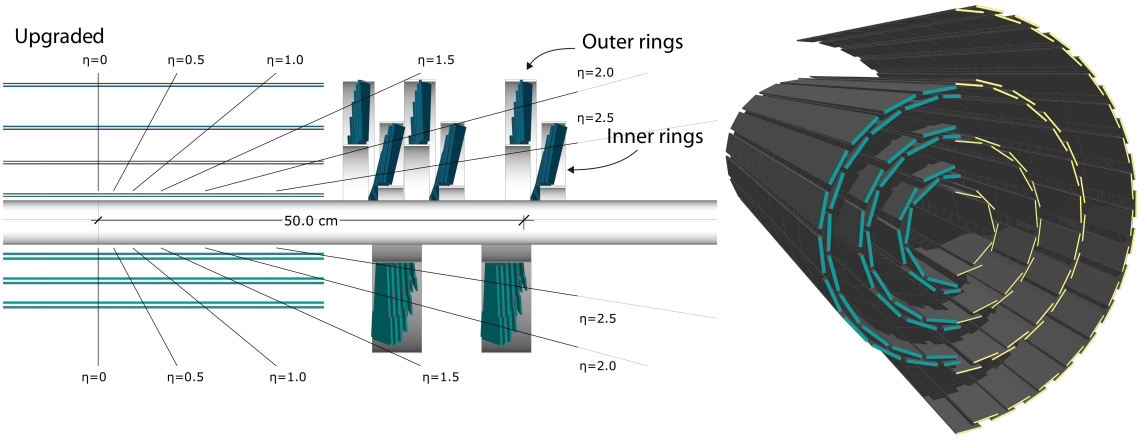

Figure 6.2: Comparison between the original and upgraded pixel detector. Left: Cutout showing the original detector on the bottom and upgraded detector on top. Right: 3D rendering of just the BPIX for the original and upgraded detectors.

The construction of the barrel and endcap sections of the upgraded pixel detector was split into separate projects. UNL collaborated with several other US institutes to build the forward section. The task of module assembly was divided between the two construction sites: UNL and Purdue University. Module testing was done at the University of Kansas and at FNAL, and the integration facility was also at FNAL. Fig. 6.3 shows the total number of modules assembled over time for both assembly sites, and for UNL only. In total 1224 were assembled and shipped to the integration site, 555 of them from UNL.

The FPIX module consists of several discrete parts, shown in fig. 6.4. These are the silicon sensor, sixteen readout chips (ROCs), a high-density interconnect (HDI) flex circuit, and the token-bit manager (TBM). The sensor and ROCs are electrically and mechanically connected via a grid of indium bump-bonds that allow for charge liberated in the sensor to be collected by the pixels on the ROCs. This process is done by a specialized vendor, so the sensor and ROCs come to the assembly sites as

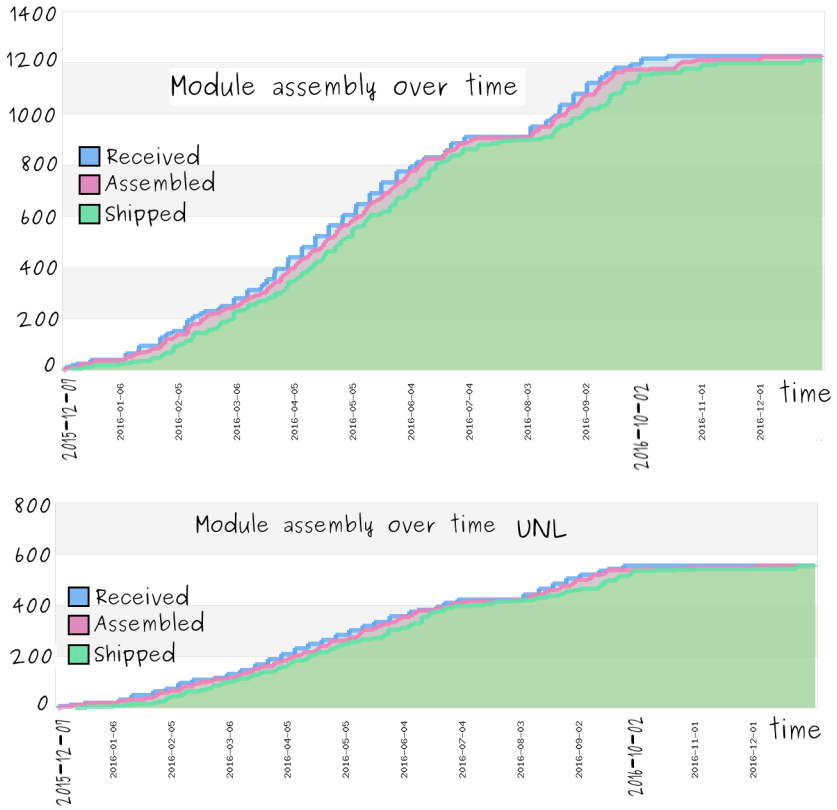

Figure 6.3: The number of modules produced over time at UNL (bottom) and over both assembly sites (top).

a single unit called a bump-bonded module (BBM). The high density interconnect (HDI) circuit also arrives to the assembly site preassembled with the token bit manager (TBM) chip and several passive elements already attached. The TBM coordinates the readout of the 16 ROCs into a single digital readout signal. Having these two parts, the necessary steps to produce a finished module are:

1. Glue the HDI to the sensor side of the BBM.
2. Wirebond the HDI to the ROCs, the TBM to the HDI, and the bias voltage on the HDI to the silicon sensor. Fig. 6.5 shows wirebonds representative of those used in module construction.
3. Encapsulate the wirebonds made in step 2. The encapsulation process helps

protect the wirebonds from electric shorts and dampen oscillations resulting from transient currents in CMS's strong magnetic field.

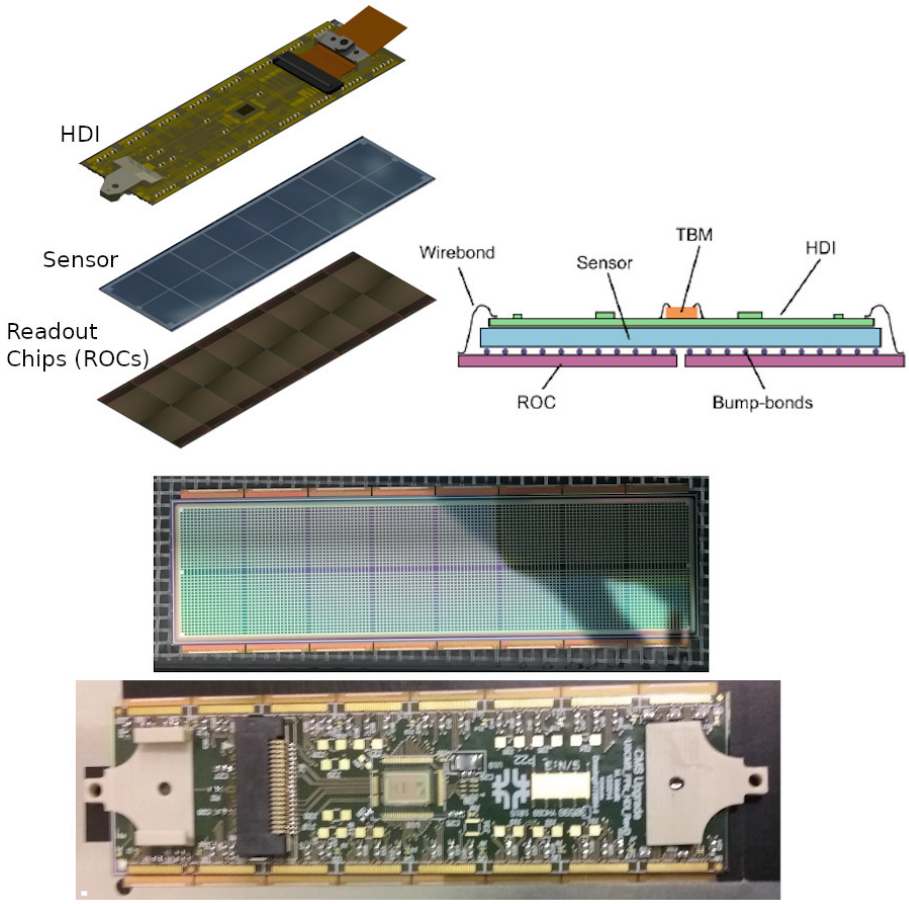

Figure 6.4: The Phase I FPIX module. Top Left: Exploded view showing the three layers that makeup a module. Top Right: Profile view showing the components, including the wirebonds and bump-bonds. Bottom: Photographs of a BBM (top) and full module (bottom).

After a module has been assembled, functional testing is done to ensure that the ROCs are all operational and the sensor has adequate performance. The flow of these steps is described in fig. 6.6. The assembly flow was designed to be a pipeline where multiple batches of modules can be flowing through the process simultaneously; e.g. a

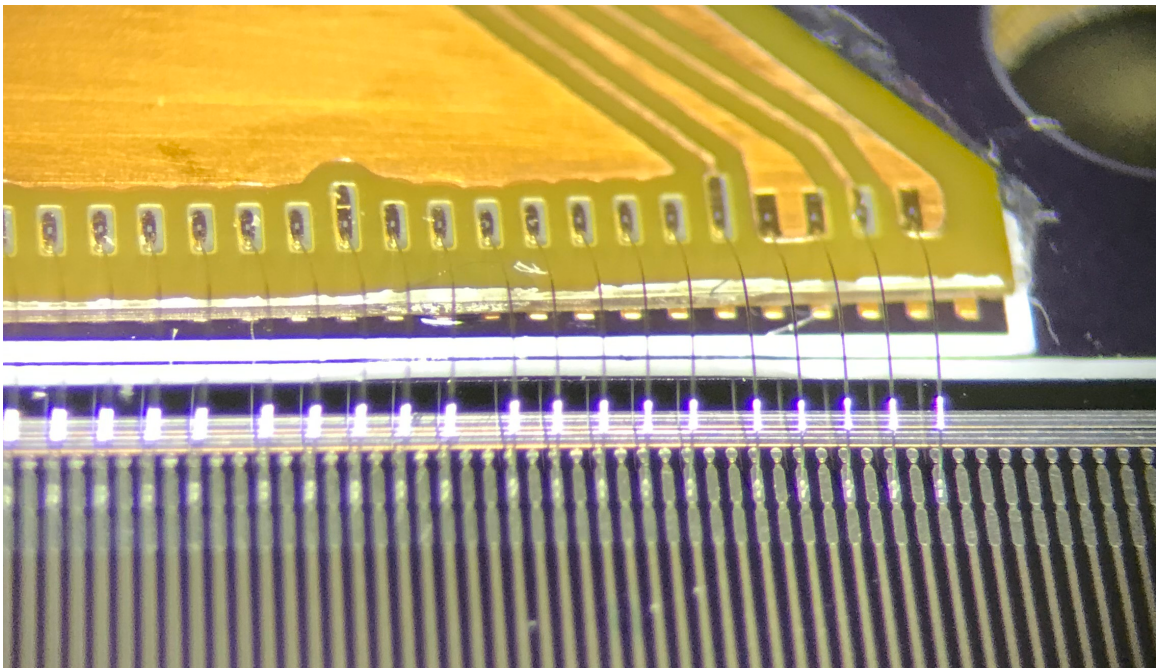

Figure 6.5: Wirebonds between electronic components.

batch of modules can be being glued at the same time that a previous batch is being wirebonded.

The gluing and encapsulation steps employed a high-precision robotic gantry, shown with tooling in fig. 6.7. The gantry was controlled by a custom LabVIEW application, discussed in more detail in the next section.

The gantry table has an arrangement of eight "chucks" (fig. 6.8). These are identical except for the HDI chuck and one of the BBM chucks which have four individually controlled vacuum lines each, as opposed to the rest which have a single vacuum line for the entire chuck. Each chuck holds one of several types of "plates". Each plate has four positions that serve to align parts used in assembly. The vacuum on the chucks serves two purposes. First, it serves to hold the plate fixed during the assembly process, and second, for the HDI and BBM plates, it supplies vacuum to hold the HDI or BBM fixed on the plate. The HDI and BBM plates have thin precision-cut pieces

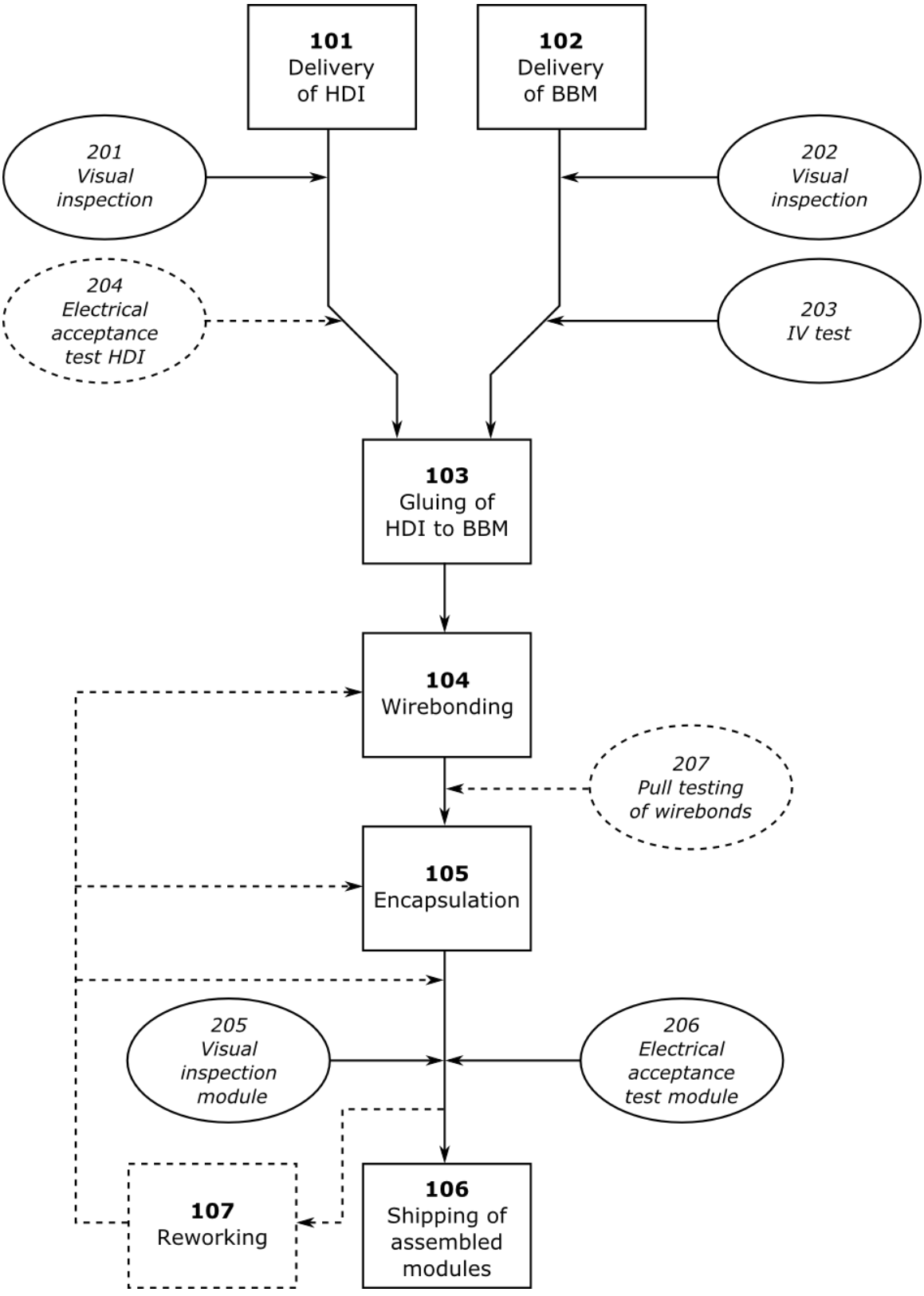

Figure 6.6: The steps involved in module assembly. The numbers correspond to a standard operating procedure document that describes in detail how each step is to be performed[87]. Dashed lines represent operations performed occasionally for quality control or repair.

of metal called stencils glued to their top face. These stencils are used to consistently position the HDI or BBM on the plates.

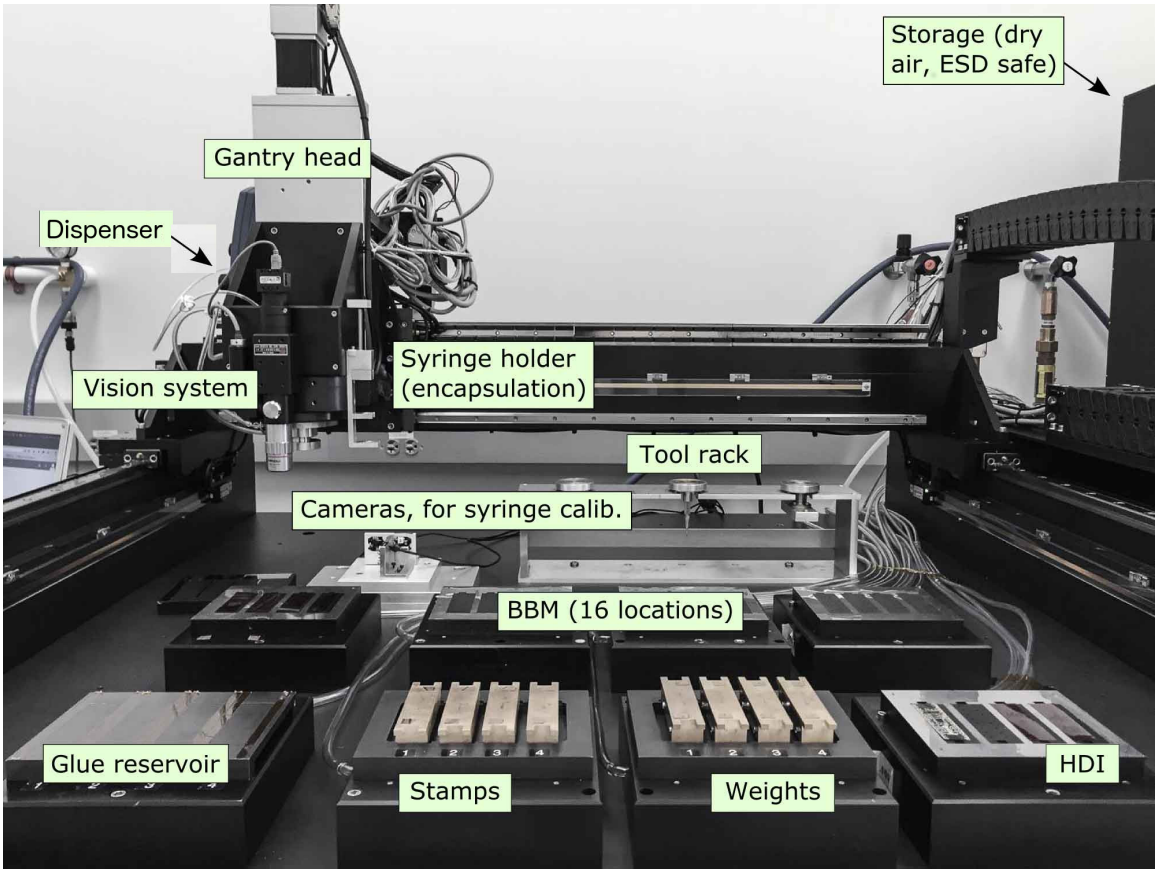

Figure 6.7: The gantry, shown equipped with the tooling used in module assembly.

The gantry head has an adapter plate which allows it to interface with and pickup various tools that are stored on the tool rack. There are two tools used in the gluing procedure: the "picker tool" and the "grabber tool". The grabber tool has metal fingers that fit underneath the tabs on the stamps and weights to lift them and move them around the gantry table. The picker tool has two small suction cups that can be supplied with vacuum to pick up the HDI so it can be placed on a BBM.

The gluing procedure is as follows:

1. Place up to four BBMs on a designated BBM chuck; for example the top left

chuck in fig. 6.7.

2. Place a matching number of HDI on the designated HDI chuck.
3. Place the stamps and weights onto their appropriate chucks, as shown in fig. 6.7.
4. Turn on the vacuum supply to all chucks.
5. Use the camera on the gantry head to acquire the position of the fiducial markings on the HDI and BBM. Perform a fit based on those measurements to acquire the exact center and orientation of the parts in gantry coordinates.
6. Prepare the Araldite 2011 epoxy and deposit enough into the glue reservoir to create an even layer level with the top of the reservoir.
7. Acquire the grabber tool from the tool rack, use it to lift a stamp, and dip it in glue. Place the stamp onto the BBM, using the weight of the stamp itself to apply the glue. Return the stamp to the stamp chuck.
8. Return the grabber tool and acquire the picker tool. Use it to lift the HDI and place it on the BBM, using the precision measurements from step 5 to ensure that there is no offset or rotation between the two parts.
9. Return the picker tool and get the grabber tool again. Use it to lift a weight and place it onto the BBM-HDI assembly.
10. Return the grabber tool to the tool rack. Repeat steps 7-9 for the remaining modules.

The encapsulation routine is in many ways simpler than the gluing one. It is performed by filling a syringe with a silicone elastomer called Sylgard. The needle on the syringe is mounted on the gantry head which brings it to just slightly above the wirebonds. A precision fluid dispenser unit then applies pressurized air to the syringe, forcing the Sylgard out of the needle tip. The gantry simultaneously moves slowly across a group of wirebonds to deposit the desired amount of Sylgard. When

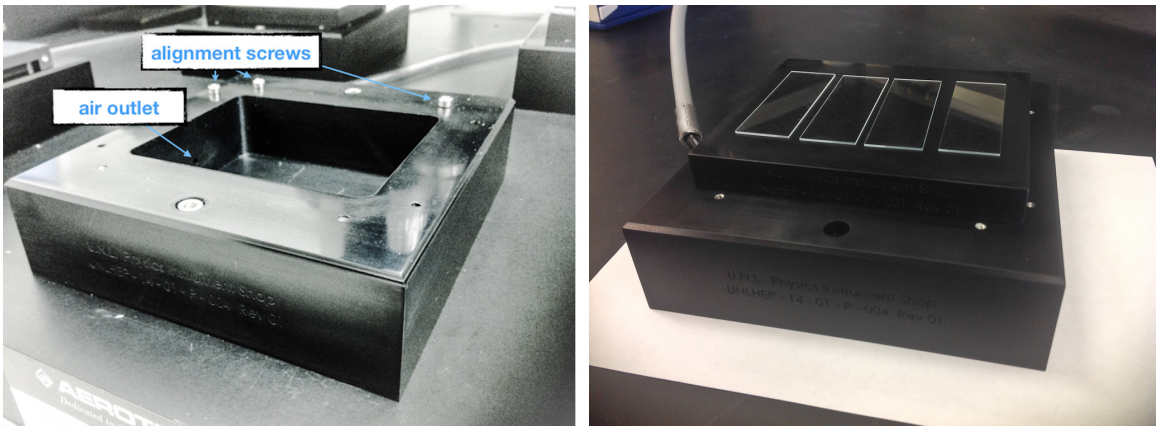

Figure 6.8: Left: One of the eight chucks arranged on the gantry table. Right: A chuck with a "plate" held to the top with vacuum. The chuck is bolted to the gantry table, and the positioning of the plate is controled by three alignmnent screws.

freshly mixed, the Sylgard has viscosity similar to room temperature honey. However, as time pases the Sylgard begins to cure and its viscosity increases. To compensate for this, the speed as which the needle moves is decreased as time-since-mixing grows.

One challenge to encapsulation is the need for precise knowledge of the needle-tip offset. Specifically, one needs to know the vector offset between the point in focus directly underneath the gantry-head camera and the tip of the encapsulation needle, and this offset needs to be recalibrated each time a new needle is loaded due to slight bends and small manufacturing defects in the needles. To acquire the offset, a duel-camera setup was deployed. It consisted of two cameras placed at right angles with an inverted needle placed where their two focal planes intersect (fig. 6.9). This is used by first bringing the gantry head camera to the setup, then centering and focusing on the tip of the inverted needle. The gantry coordinates at this position are recorded. Next, the encapsulation needle on the gantry head is brought to close proximity with the inverted needle. The two cameras on the setup are used to guide the operator to align the two needle tips so they are just touching. The difference between this position and the previous recorded position is the vector offset needed

for needle-tip calibration.

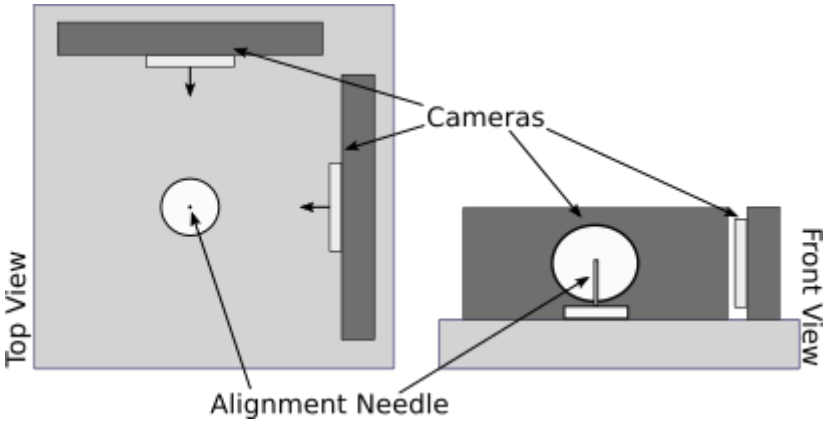

Figure 6.9: Sketch of the needle-tip calibration setup.

6.2 Automated Assembly of FPIX Modules

During module pre-production the first version of the LabVIEW gantry control application was written. As an R&D platform, the initial software served to develop the procedures and tooling for module assembly outlined in the previous section. However, as the project moved into production, serious flaws in the design of the software became apparent. Specifically, a memory leak in the encapsulation routine rendered the software unable to encapsulate batches of more than 1 module. This resulted in each module taking roughly an hour to encapsulate, straining the limited manpower available at UNL. The operation of the software also required significant training, further taxing the team. These issues motivated a complete rewrite of the software, following LabVIEW development best practices. The software is divided into a reusable library that contains common functions such as gantry movement, vacuum control, access to the cameras, and so on. Applications are built on top of this core library to perform specific tasks such as gluing and encapsulation. This author was the sole developer of the core library and encapsulation routine. The gluing routine

was written by another developer, using the core library and following the template of the encapsulation routine.

LabVIEW is a proprietary programming language and development environment by National Instruments. The language is unusual in that it is not text-based, but instead programming is done by dragging graphical wires to connect the inputs and outputs of various functions, or in LabVIEW terminology "virtual instruments" (VIs). Familiar programming constructs such as loops, case structures, if statements and so on are implemented as visual boxes which contain the code within the structure. Every VI has two parts: a block diagram (the code), and a front panel. The front panel has visual representations of variables used in the function. For example, a boolean variable may have a switch in the front panel if it is an input, or a light if it is an output. A string variable would similarly have a text entry field or a text display. Building up a front panel for an application VI is the standard way to build GUIs in LabVIEW. LabVIEW also supports object-oriented programming, a feature used extensively in the gantry software rewrite.

The core of the gantry software[88] is the `Gantry` class. This is the interface that any application uses to interact with the gantry hardware. It also owns a `Worktable` object that keeps track of the state of the gantry table. For example, if the `Worktable` is configured for gluing, it will keep track of which positions have BBM, HDI, assembled modules, and so on. This helps prevent programming errors that would result in attempting to place an HDI on an already assembled module, for example. Having all hardware access happen through a single interface also assists in application development as it provides a single clear set of functions to the programmer, as opposed to having several different APIs to reference for the different hardware on the gantry. The hardware controllable by the `Gantry` class includes:

- The robotic gantry itself
- The vacuum to the chucks and gantry head
- The cameras, both on the gantry head and on the needle-tip calibration setup
- The fluid dispenser

An important feature of the software to aid automation is to automatically extract fiducial locations from images taken by the gantry head camera. An algorithm[89] was designed and implemented with the OpenCV[90] computer vision library. Fig. 6.10 shows the important steps in the algorithm for some representative fiducials. Because this algorithm is implemented in C++, it and its LabVIEW wrappers are bundled separately from the rest of the gantry software[89].

1. Acquire an image from the gantry head camera. The algorithm works best if the fiducial is completely within the camera's field-of-view. Because of this, it is important to have parts placed consistently on the gantry table at least to the 100μm level to be reliably within the roughly 1 mm by 1 mm field-of-view of the camera.
2. Apply the K-means clustering algorithm to group pixels based on their brightness. For the BBM fiducials, the fiducial appears bright white on a generally gray background with black flecks. This implies that the K-means clustering should attempt to find three groups where the brightest group of pixels is the fiducial while the other two are background. For the HDI fiducials, there are really only two color groups: black and gray. Therefore, in this case K-means is instructed to only attempt to make two groups. Again, the brighter of the two groups is the fiducial and the other group is background. In both cases, the end result is a binary image with only black and white pixels.

3. It is important to have closed shapes. To help with this a "dilate" operation is performed. This operation takes each white pixel and make its neighbors within a certain radius white as well. This acts to close small holes in the foreground resulting from the texture of the fiducial.
4. After step 3, there are potentially several blobs of white on a black background, only one of which is the fiducial. To pick out the fiducial, the area and aspect ratio of each blob is calculated and if either lies outside of a prescribed range it is discarded. These ranges are tuned to consistently select only the fiducial and no other random blobs in the image. To provide tolerance to rotated fiducials, the aspect ratio is calculated from a minimum-bounding-box (the white rectangle).
5. Finally, the centroid of the remaining blob is calculated and returned as the position of the fiducial in the image.

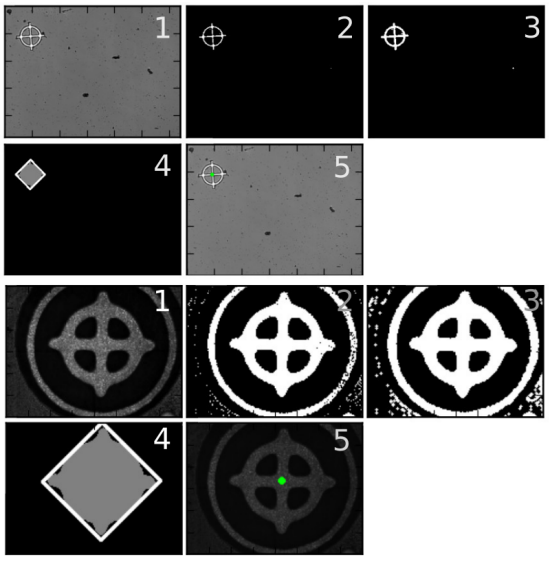

Figure 6.10: Demonstration of the fiducial recognition algorithm. The top series of images shows a BBM fiducial while the bottom images show a HDI fiducial.

Another necessary function of the software is to calculate from the fiducial position the center and orientation of the parts in the gantry coordinate system. The problem

can be phrased like so: given a set of coordinates of reference points in a local Cartesian coordinate system and a corresponding set of measurements of these reference points in the global Cartesian coordinate system, find a coordinate system transformation, $\mathbf{x}' = \mathbf{A} + R\mathbf{x}$, such that the distance between the local coordinate system points and the transformed global points is minimized. In two dimensions, a simple linear regression can be done to find the offet, $\mathbf{A}$, and the rotation matrix, R, but in three dimensions such an approach suffers from numerical instability near the poles of the spherical coordinate system. Therefore a more sophisticated algorithm is needed. There are many algorithms that solve this problem[91], but Horn's method[92] was chosen due to its simplicity and available reference implementations.

Because the encapsulation routine of the original software was causing issues in production, it was the first candidate for a rewrite using the library of functionality outlined here. Further implementation details of this new application are outside the scope of this document, but figs. 6.11, 6.12, 6.13, 6.14, 6.15 follow a walkthrough of an encapsulation session as it would appear to the operator.

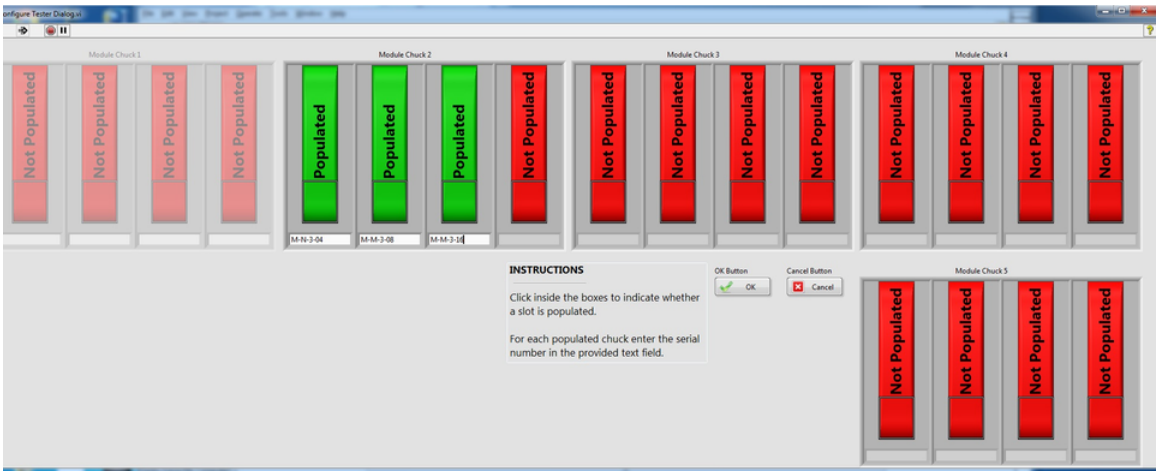

Figure 6.11: The operator must first tell the application which positions on the gantry contain modules to be encapsulated as well as the serial numbers of those modules. This information is used when generating the report and logfile.

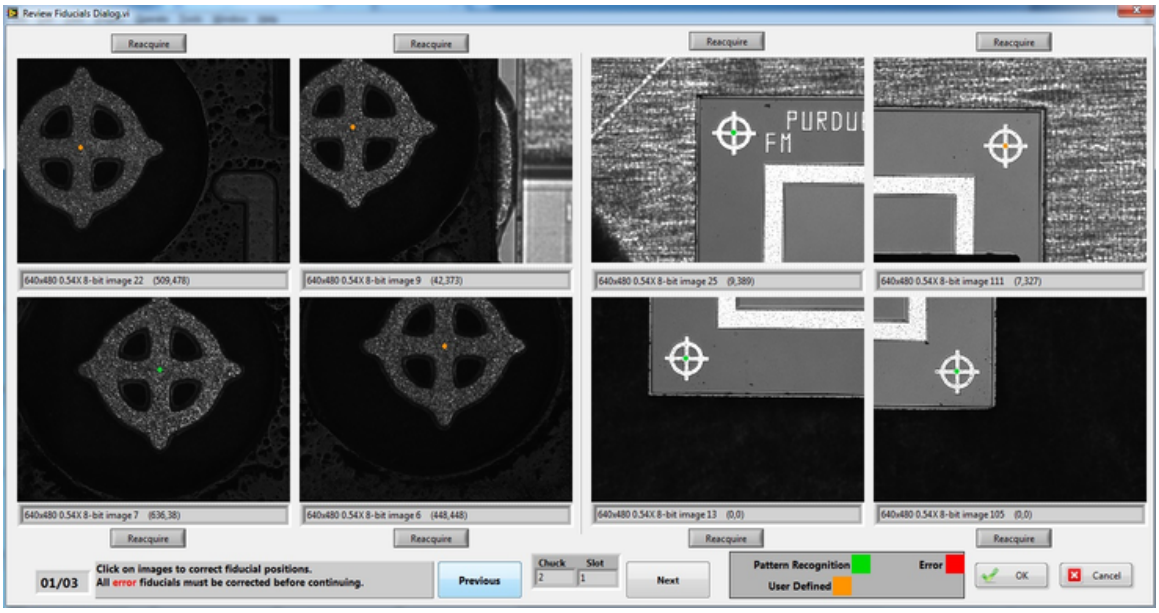

Figure 6.12: Once the application knows which slots contain modules, it proceeds to acquire fiducial images on the HDI and BBM and run the pattern recognition to find the fiducials in the images. The operator can then review the results of the pattern recognition and make corrections as necessary.

After roughly two months of development, the new encapsulation routine was deployed in production and immediately improved throughput and reliability of encapsulation. It went on to successfully encapsulate modules for the rest of production and served as a useful pattern upon which to develop a new gluing routine. This same framework is currently being iterated upon for deployment at several assembly sites for the Phase II upgrade of CMS.

6.3 Quality Control

An important feature of the encapsulation application is that it keeps a log file containing information such as the serial numbers of modules that were encapsulated, their measured positions, the sections to be encapsulated, and so on. A utility was written to extract information from these log files to measure the quality of alignment

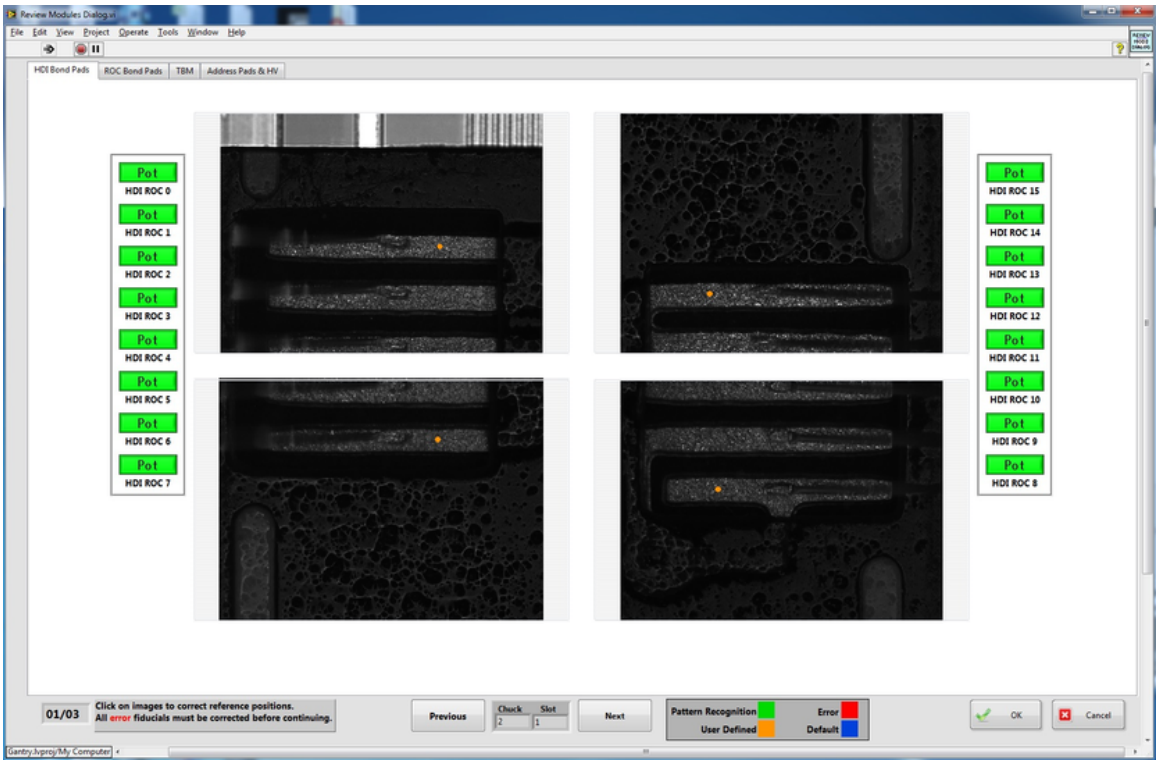

Figure 6.13: After the fiducials are found and the precise position of the module in space has been calculated, the application will instruct the gantry to get reference images to help define where the encapsulation lines will go. Here, the user is presented with the wirebond pads on the corners of the HDI. They then select a position as seen in the image (orange dot) from which the application calculates the lines of encapsulant to go along each side of the HDI. The user may also select a subset of wirebond groups to encapsulate. This is useful if the module is returning after being reworked and only a subset of it needs to be encapsulated. Similar UI exists for the ROC bond pads, the TBM bond pads, the address pads, and the bias voltage wirebonds.

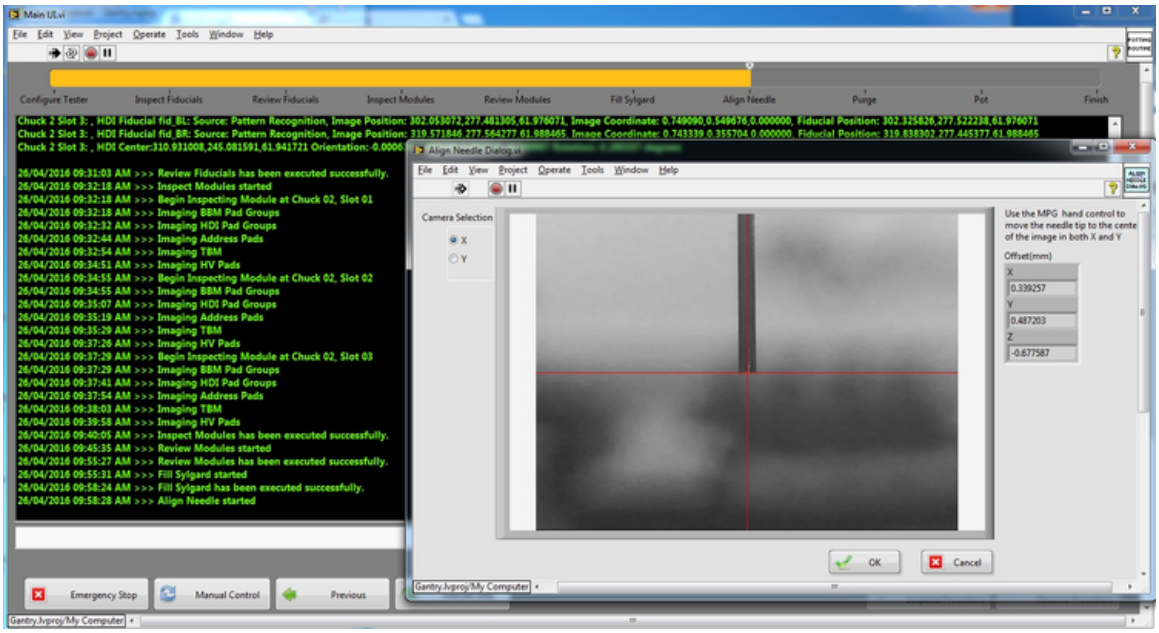

Figure 6.14: After the encapsulant lines have been defined, the operator is instructed to mix Sylgard and load the encapsulation needle on the gantry head. After doing this, the application brings the gantry to the needle-tip calibration station. Shown here is the view from one of the cameras on the station. During this step, a hand-controller is enabled for the operator to align the needle with the crosshairs. (Note that the inverted needle is missing in this image, but would normally be visible in the bottom part of the screen.)

during the gluing routine. Fig. 6.16 shows one of these quality metrics. This is for modules that were assembled by the initial gluing routine, before the rewrite of the gluing routine was finished. It shows a pattern consistent with an incorrect rotation correction, meaning that when the HDI is rotated to match the rotation of the BBM during gluing, that rotation is incorrect. Indeed, upon further investigation it was found that there was a sign error in the rotation correction, leading to the rotation actually being worsened by the "correction". This went unnoticed previously because the correction is normally so small, it is imperceptible to a casual observer.

Another example of information that could be gleaned from the encapsulation log files is discovering changes in raw materials. For example, by plotting the post-fit

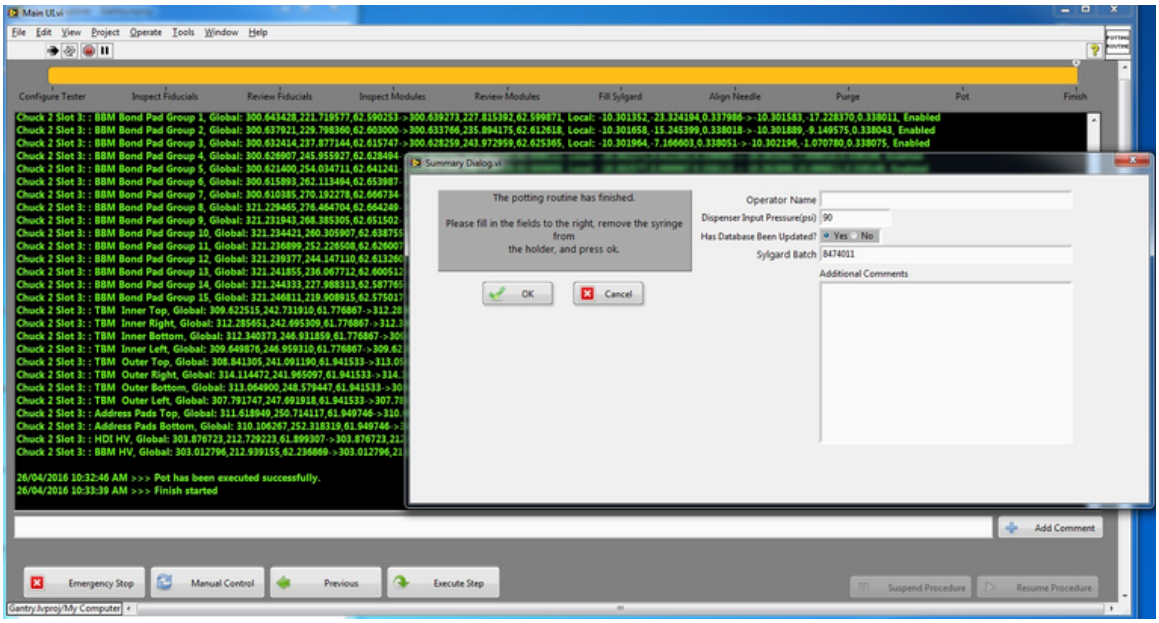

Figure 6.15: After needle-tip calibration, the gantry will encapsulate the modules with no further operator intervention. When it finishes, it presents the operator with a summary window where the operator will fill in some information about the encapsulation session and any notes. This information gets added to the log file.

positions of fiducial markings on HDI and separating them by vendor, we found that the HDI produced by Compunetix were out-of-spec by roughly 70 μm as shown in fig. 6.17.

The assembly precision that was ultimately achieved using the gantry and associated tooling and software are shown in figs. 6.18, 6.19.

6.4 The Phase II telescope

In anticipation of test beams to commission detector elements of the Phase II Upgrade of the CMS detector, a telescope was designed by this author to precisely measure the trajectories of particles in the test beam to serve as a reference when evaluating the performance of a device under test (DUT). The design of the telescope is centered around several layers of silicon strip sensors placed fore and aft of the DUT. Hits

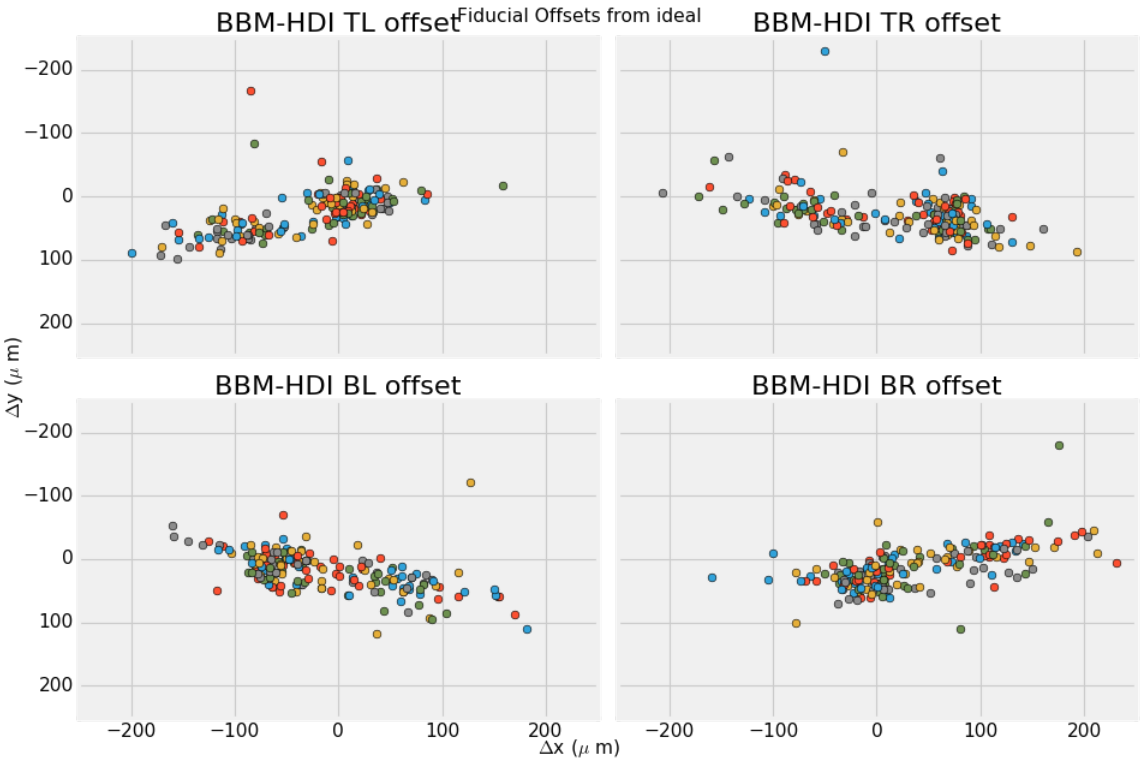

Figure 6.16: Position of the HDI fiducial in the BBM's coordinate system relative to where it would be with perfect alignment.

in the strips are correlated to construct a track. This track is then projected onto the DUT, and the distance between the impact position of the projected track and the position reading from the DUT form a residual that can characterize the DUT. Fig. 6.20 shows a block diagram of the operation of the telescope.

6.4.1 Detector and Readout Chip

The telescope's several layers of sensing material consist of silicon micro-strip sensors. These particular sensors are composed of 512 strips with 25 μm pitch. The metalization that defines the strips has readout pads on alternating sides of the chip leading to 50 μm pitch on the pads along either side. Fig. 6.21 illustrates this pattern.

The sensor is read out with an integrated circuit called the Analog Pipeline Chip -

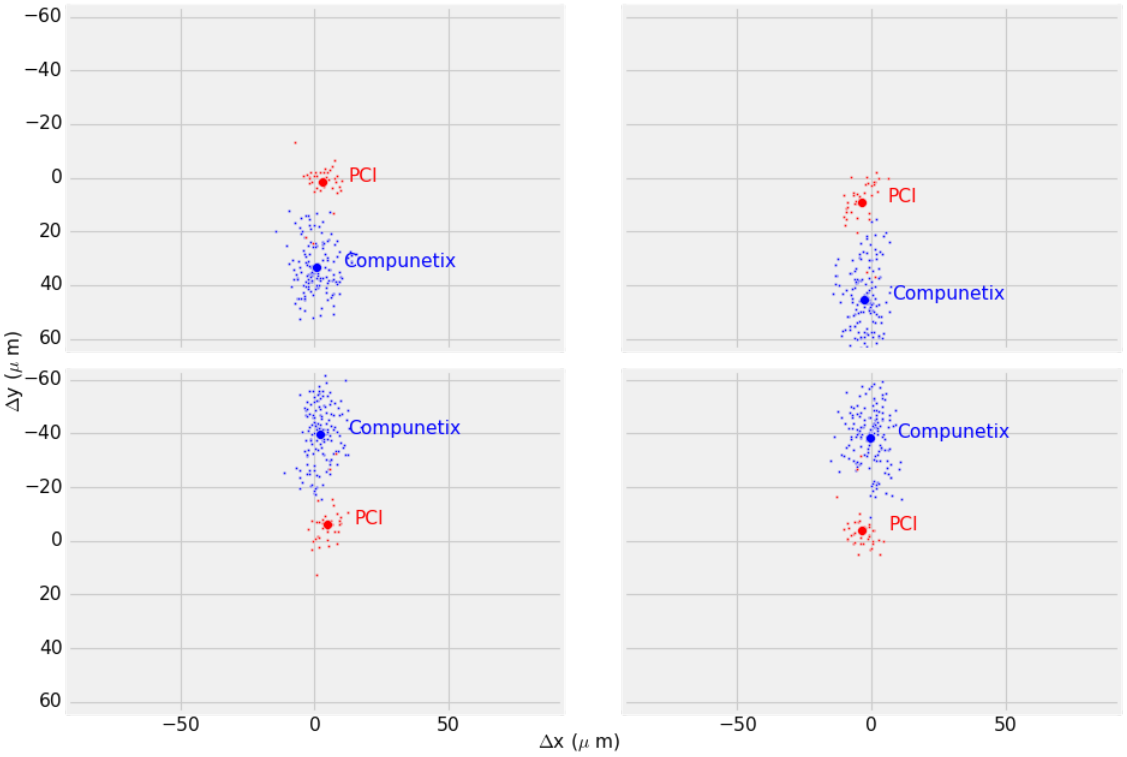

Figure 6.17: The measured positions of HDI fiducials in the HDI coordinate system. Ideal values are (0,0). The Compunetix HDI are clearly out of spec (the HDI are too short) while the PCI parts are much closer to the design values.

128 (APC128). Each APC128 is has a 128 channels which correspond to reading out 128 strips of a silicon micro-strip sensor. Fig. 6.22 shows an operational schematic detailing one of these channels. Going from left to right, the circuit consists of a pre-amplifier, the sampling capacitors, and readout pipeline.

When the APC128 is in sampling mode SR is high, meaning that the switches labeled SR are closed and the switches labeled $\bar{SR}$ are open, and IS is high. We also assume that $Reset$, $R12$, and CS are low. In this configuration any current originating from `In` flows onto C_1. The pre-amplifier will sink the charge that was removed from the right "plate" of C_1 to keep it electrically neutral. In the end, the pre-amplifier now has a voltage to maintain on its output that is proportional to the charge read from the sensor. If the $R12$ signal is pulled high by external control circuitry, some of the

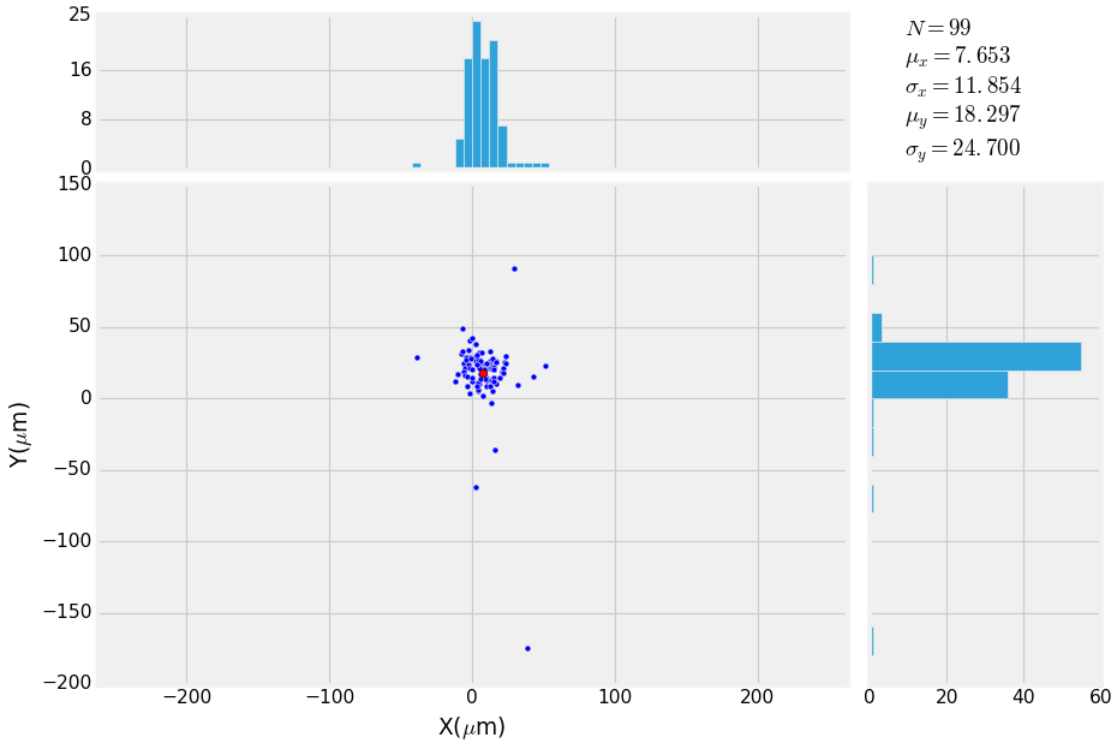

Figure 6.18: Distribution of planar misalignment between BBM and HDI parts based on measurements taken during encapsulation. Alignment is generally better than 50 microns.

charge from C_1 is allowed to bleed off over time so the voltage of the pre-amplifier will spike with input current and slowly return to its original value. $R12$ also keeps leakage current from saturating the pre-amplifier. On the other hand, if *Reset* goes high, all of the charge is quickly removed and the pre-amplifier immediately returns to its original state. In a testing environment with bunched particles, the *Reset* signal may be timed with the beam crossing to clear out the channel between bunches. However, if there is ambiguity when particles could potentially arrive, it is useful to keep a series of periodic samples of the input signal and then read out the correct one when a trigger is received.

Each channel has 32 sampling capacitors, labeled C_p in the schematic. A bit is shifted through the "Pipeline shift register" which connects the output of the pre-

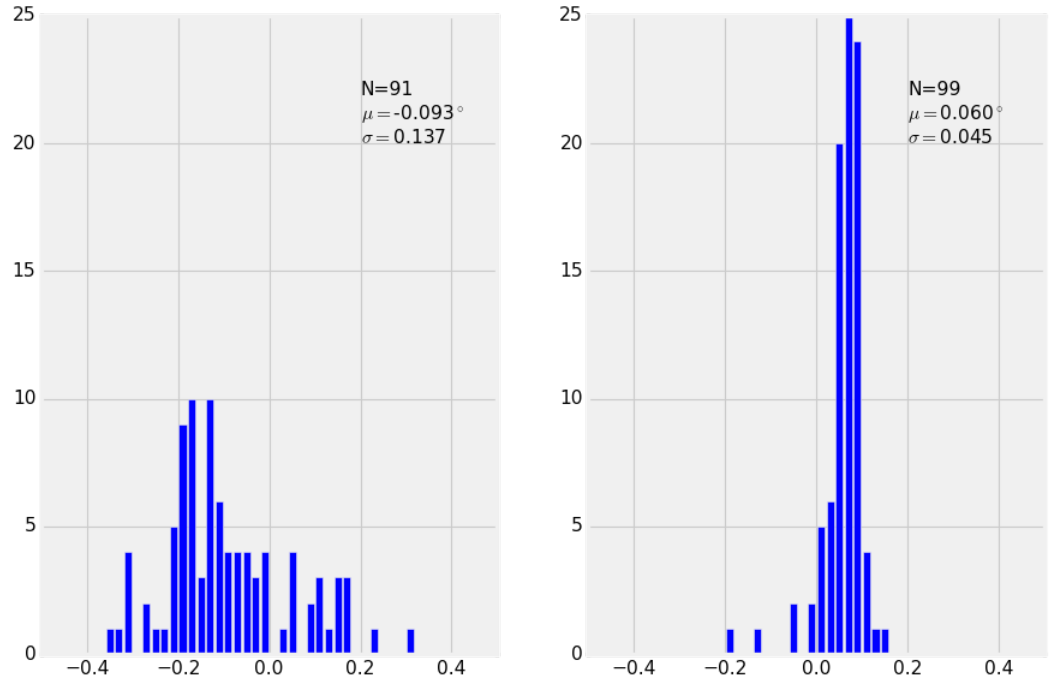

Figure 6.19: Distribution of the relative rotation between the assembled HDI and BBM before (left) and after (right) fixing the reverse rotation bug.

amplifier to one C_p at a time. When the pre-amplifier is connected to a particular C_p, that capacitor gets charged to a voltage proportional to the input signal at that time. As the bit moves through the shift register, it takes a series of 32 samples of the input signal. Having a time series of samples is important because there is generally a time delay between when the signal from the sensor arrives and when a trigger makes its way through the trigger system to the chip. Without a history of samples, the pulse height information will be lost by the time a trigger arrives.

When a trigger arrives, sampling of the input stops. A specific C_p is selected with the pipeline shift register based on a pre-calibrated trigger delay, and the SR and IS signals go low. This hooks up the C_p capacitor back to the input of the pre-amplifier. A bit is shifted into the "Readout shift register" which connects each of the 128

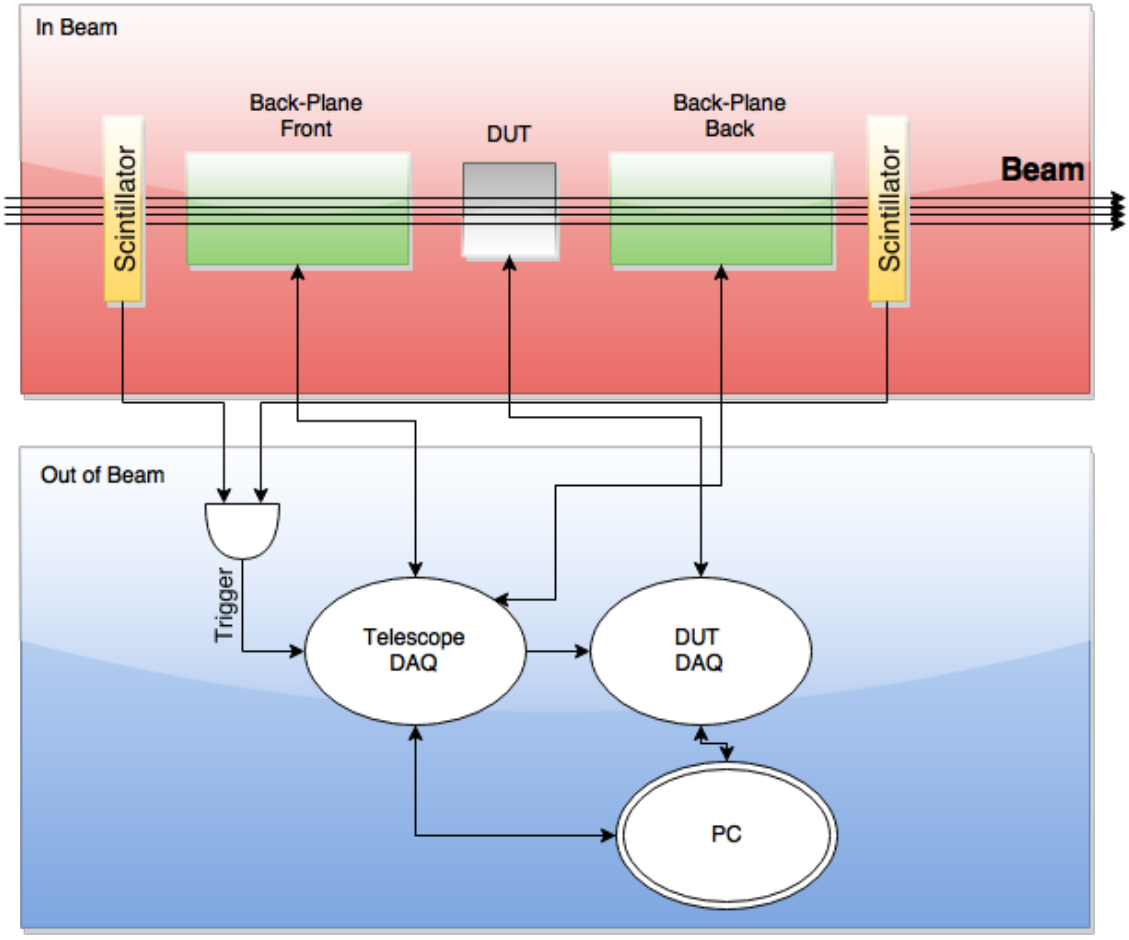

Figure 6.20: Block diagram of the telescope. The lines represent signal flow. Two scintillation detectors are used to trigger the readout of the system. The trigger is handled first by the Telescope DAQ, and then passed on to the DUT's DAQ. Collection of data from the telescope and DUT then occurs in parallel.

channels sequentially to the output stage. When a particular channel is connected to the output stage, the pre-amplifier charges the C_L capacitor which in turn places a voltage across C_{fb} and causes the output amplifier to supply an analog voltage that is proportional to the magnitude of the original pulse from the silicon micro-strip sensor. As the bit in the readout shift register works its way through the channels, a series of analog voltages are supplied to the output which ultimately represent the charge deposits on each of the 128 strips the particular chip is connected to.

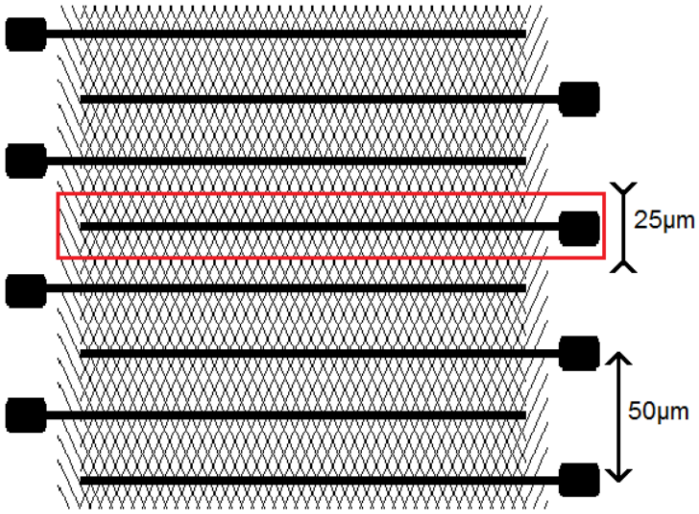

Figure 6.21: Schematic representation of the silicon micro-strip detector to be used with the telescope. The solid lines indicate metalization that collects charge liberated by the traversal of an energetic charged particle.

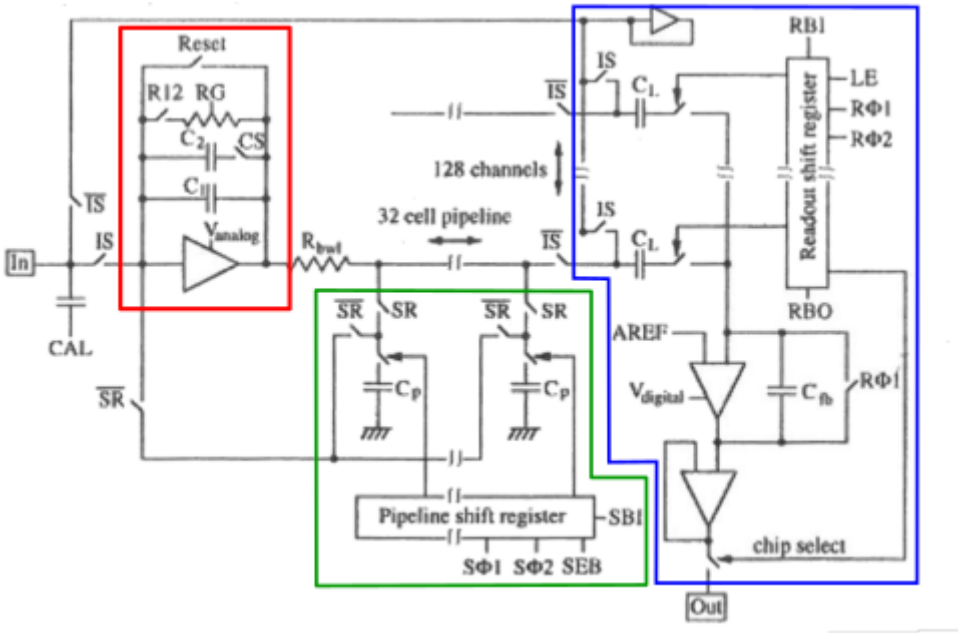

Figure 6.22: Operational diagram of the APC128. Note the main features: a charge sensitive pre-amplifier(red), a sampling pipeline(green), and the readout stage(blue).

For calibration and testing, the input of the pre-amplifier is given a charge through the CAL input. There is a separate CAL capacitor for each channel with values that cycle starting with C, then 2C, 3C, 4C, and back to C. The different capacitor values give different charge inputs to the pre-amplifiers for a shared calibration voltage. As the different channels are read out, the analog output voltage will step through four discrete values corresponding to the four different capacitor values. Fig. 6.23 shows a typical example of this "step curve".

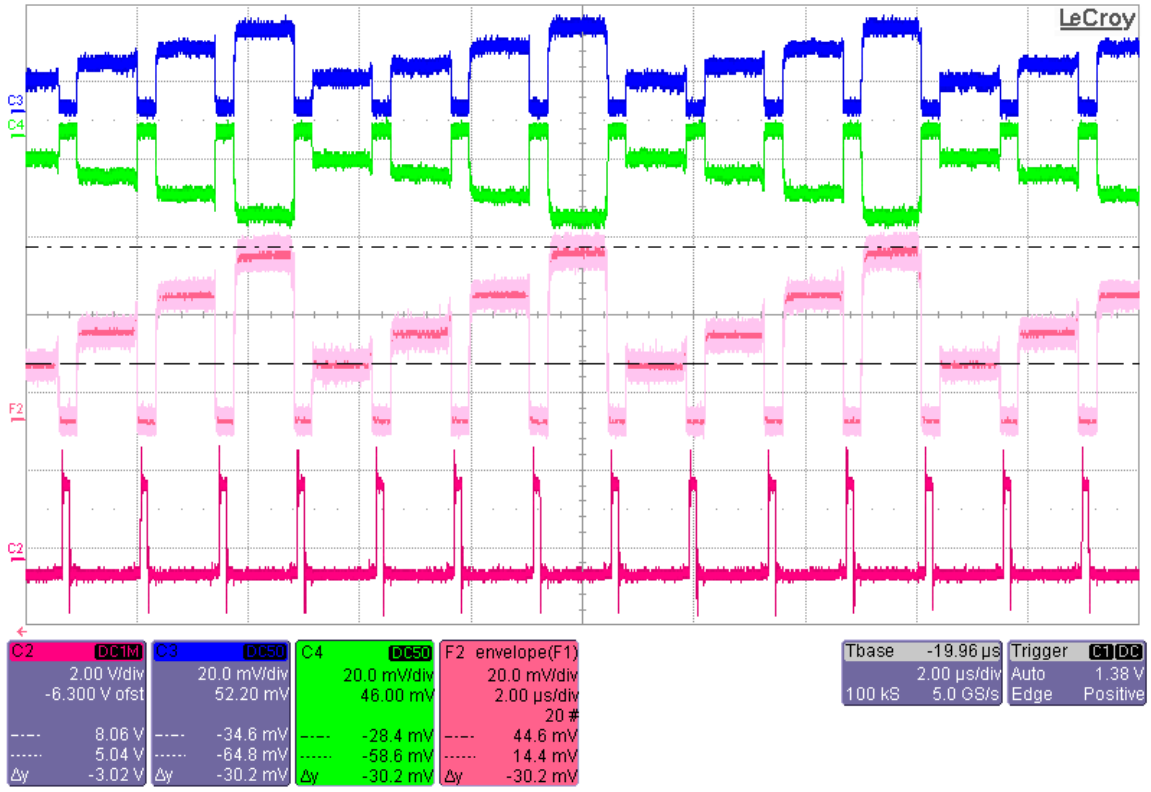

Figure 6.23: The calibration "step curve" for an APC128 chip. In this oscilloscope trace the signal has been routed through a differential amplifier, thus the inverted blue and green traces. The pink envelope shows the subtraction of the differential signals and clearly demonstrates the "step" nature of the signal. The dark pink curve shows the $R\Phi1$ signal which, together with $R\Phi2$, steps the channel selection bit through the readout shift register.

The APC128 was originally developed for the HERA experiment at DESY[93] in the

1990s. In the decades since, much expertise on the operation and performance of the chip has been lost, and very little technical documentation is available. Therefore, in order to better understand the operation of the chip, this author designed a dedicated testboard as part of the telescope R&D. Fig. 6.23 was acquired with the aid of this test board, an image of which is shown in fig. 6.24.

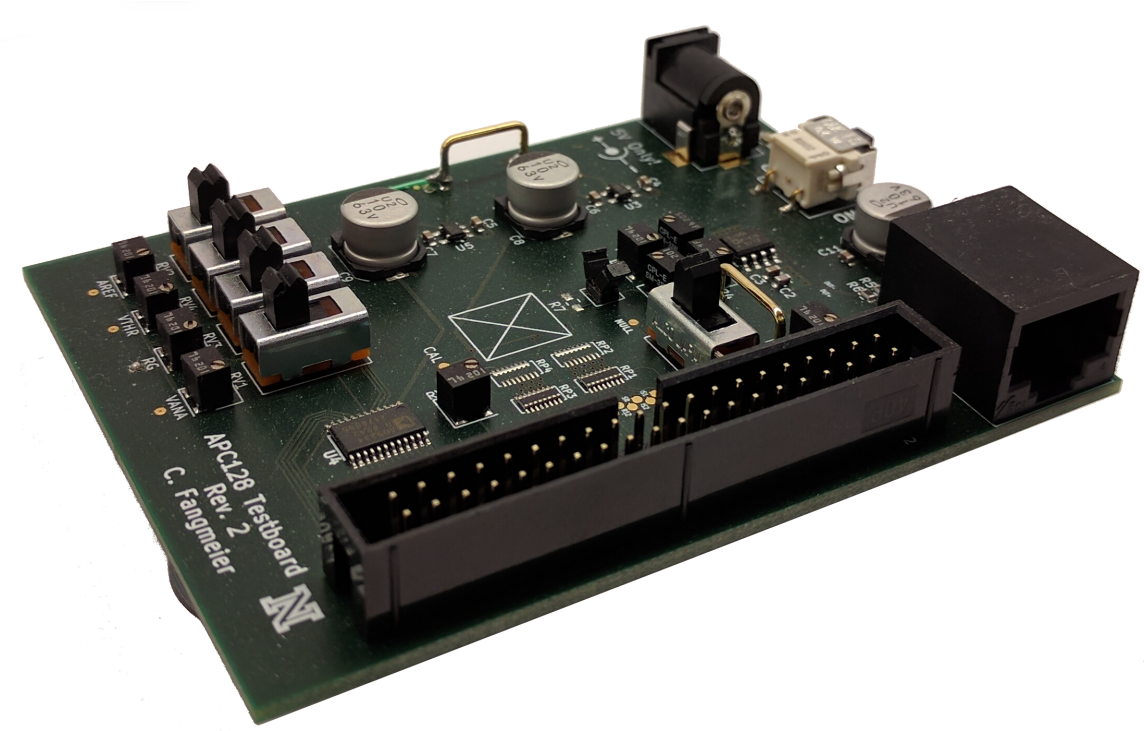

Figure 6.24: The testboard for characterizing the APC128 chip and developing the correct control sequences to generate the step curve shown in fig. 6.23. The APC128 is mounted on the reverse side of the board. The board features switchable potentiometer and DAC analog supply voltage sources, an integrated adjustable gain differential amplifier with twisted pair output, and parallel digital control signal supply via a 40-pin parallel cable. The control signals are generated off-board by an Altera Cyclone-IV FPGA running custom firmware. Schematics of this board are available at [94]

Developing the signal patterns that correctly operate the chip to produce the step curve was a significant achievement. This is because even a small error in the pattern can result in erroneous output, with little indication of exactly which signal was wrong and at which clock cycle. To assist in the development of the control signal patterns,

software was developed by the author to convert a simple text-based representation of the pattern to FPGA firmware that would actually generate those patterns. Fig. 6.25 shows an excerpt from one of these patterns. A "-" indicates that the digital signal is high during a clock cycle while a "_" indicates it is low. This excerpt shows the pipeline selection bit being shifted through the pipeline shift register of the APC128 while at some point the `CAL` signal goes from high to low, injecting some charge into the pre-amplifier. The pre-amplifier will then charge up the currently selected pipeline capacitor. A following section of the pattern will select this capacitor for readout and shift through all 128 channels, producing the step curve.

```
stage CAL_INJECT 1
CAL   : ------------------------_------------------------
SBI   : _--_------------------------------------------------
SPHI1 : _-___-___-___-___-___-___-___-___-___-___-___-___-___
SPHI2 : ___-___-___-___-___-___-___-___-___-___-___-___-___-_
SEB   : ------------------------------------------------------
ISSR  : ------------------------------------------------------
RESET : ------------------------------------------------------
R12   : ------------------------------------------------------
RBI   : ------------------------------------------------------
RPHI1 : ------------------------------------------------------
RPHI2 : ------------------------------------------------------
LE    : ------------------------------------------------------
```

Figure 6.25: An excerpt from the APC128 control signal pattern for producing the step curve. Note that here the IS and SR signals are tied together and represented by ISSR. The full pattern as well as the tooling to convert such a text pattern to FPGA firmware can be found at [95].

Studies were also done to observe the shape of the pulse when charge is injected into the pre-amplifier via the calibration capacitor. This is shown in fig. 6.26. The plot clearly shows the increasing magnitude of the output signal with increasing calibration capacitance, as well as the decay of the signal when the feedback resistor is enabled.

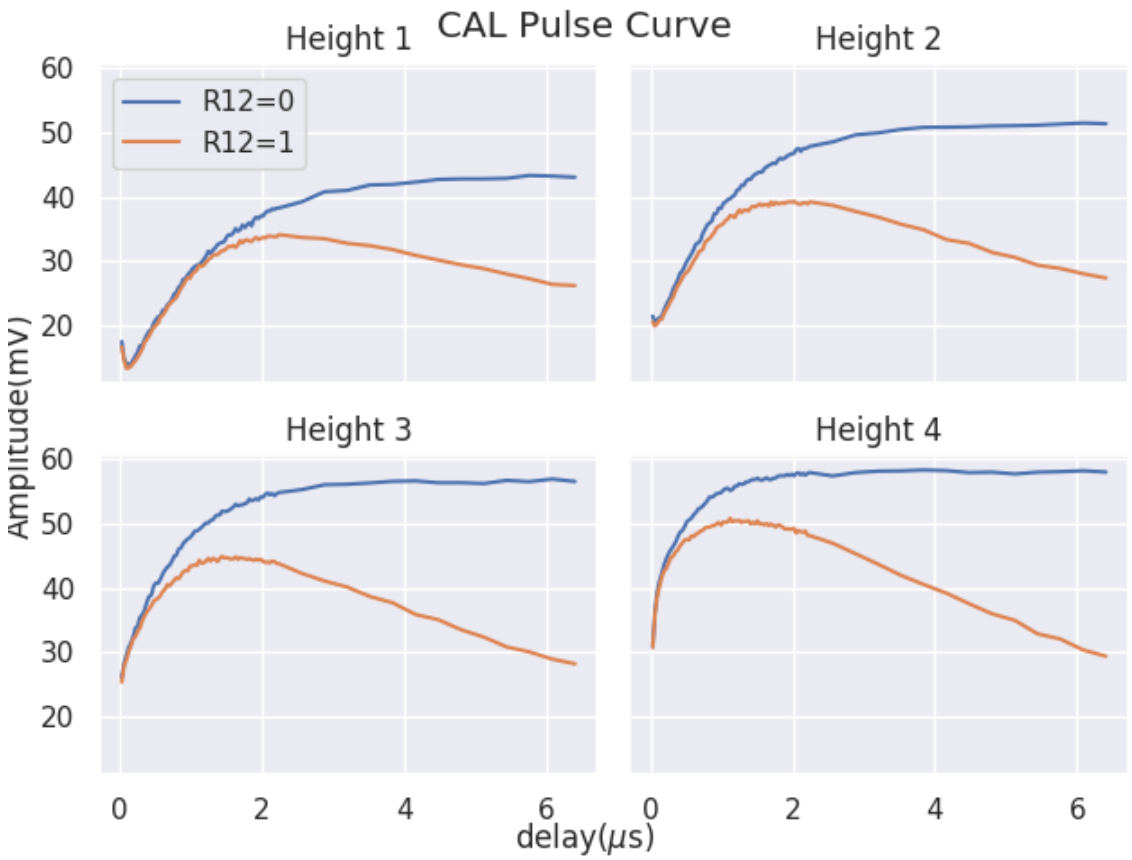

Figure 6.26: The relationship between the output voltage and the time delay between when the calibration charge is injected and when the pre-amplifier is sampled. Height 1-4 correspond to the four calibration capacitor values. The value of `R12` indicates whether or not the switch enabling the feedback resistor is open(0) or closed(1).

The design of the telescope calls for four layers of detector on each side of the DUT. Each layer will contain one silicon micro-strip detector with four APC128 chips to read out all 512 strips. The analog output of the APC128 has relatively high impedance[96] which implies the need for a nearby amplifier to drive the signal through the connections that lead out of the beam area to the data acquisition board (DAQ). This may be a distance of up to several meters, depending upon the beam site. Based on these requirements, the AD8138ARZ differential amplifier was chosen to drive the signal and twisted pairs in a CAT-5 (i.e. Ethernet) cable were chosen

to carry the signal. The board that carries the micro-strip detector, APC128, and amplifiers is referred to as a sensor card. There are four sensor cards mounted onto each of two identical back-plane boards as shown in fig. 6.27.

The back-plane board would be physically mounted to supports to hold the sensors in the beam path. It has four RJ-45 ports for the CAT-5 cables that route the differential analog signals to the DAQ and a 2x20 parallel connector for the DAQ to supply the APC128 control signals, bias voltage, and other miscellaneous signals required by the sensor cards.

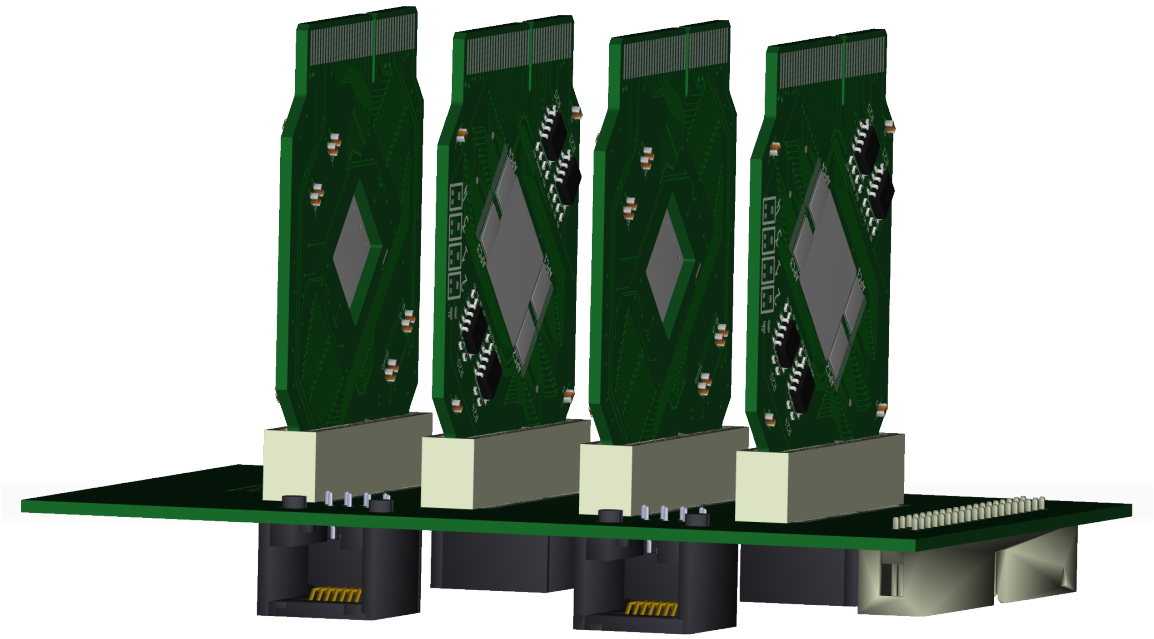

Figure 6.27: One of the two identical back-plane boards that make up the in-beam part of the telescope. The silicon micro-strip detectors are mounted at a 45 degree angle relative to the back-plane board, and each of the cards has board-edge connectors on both the top and bottom. This means that the cards can be rotated 180 degrees to change the relative orientation of the strips. They can be alternating horizontal-vertical (as shown), all vertical, all horizontal or any combination accoring to the operator's needs.

6.4.2 Data Acquisition Board

The DAQ has four main functions:

- Generate the control patterns for the APC128. This includes the pattern to continuously sample the pre-amplifier and the pattern to select the correct sample from each channel and readout the samples.
- Digitize the analog signals coming from the 32 APC128 chips. To minimize downtime during readout, all 32 are digitized in parallel.
- Pre-process the readings to suppress noise and identify hits.
- Transmit the collected hit data to a connected PC for further processing and storage.

To accomplish these goals, a DAQ board, shown in fig. 6.28, was designed and built. Not shown in the figure is the brains of the board: an Opal Kelly ZEM4310 FPGA integration board. The ZEM4310 plugs into the two central HSMC connectors which connect the FPGA to power, the ADCs, the APC128 control pattern lines, and other utility circuits. The ZEM4310 was chosen for its high amount of I/O, USB3 connectivity, and, importantly, its use of an Altera FPGA, a part that the DAQ designer already had experience programming.

6.4.3 Software

An FPGA is a dynamic and programmable piece of hardware. Unlike devices like micro-controllers, however, an FPGA is able to directly emulate bare-metal logic circuits. This means that specialized digital circuits can be designed to handle specific tasks quickly, efficiently, and in parallel. The downside of this, however, is that FPGAs cannot be programmed with a typical programming language like C or Python, but instead use a special *hardware* design language. There are two popular language

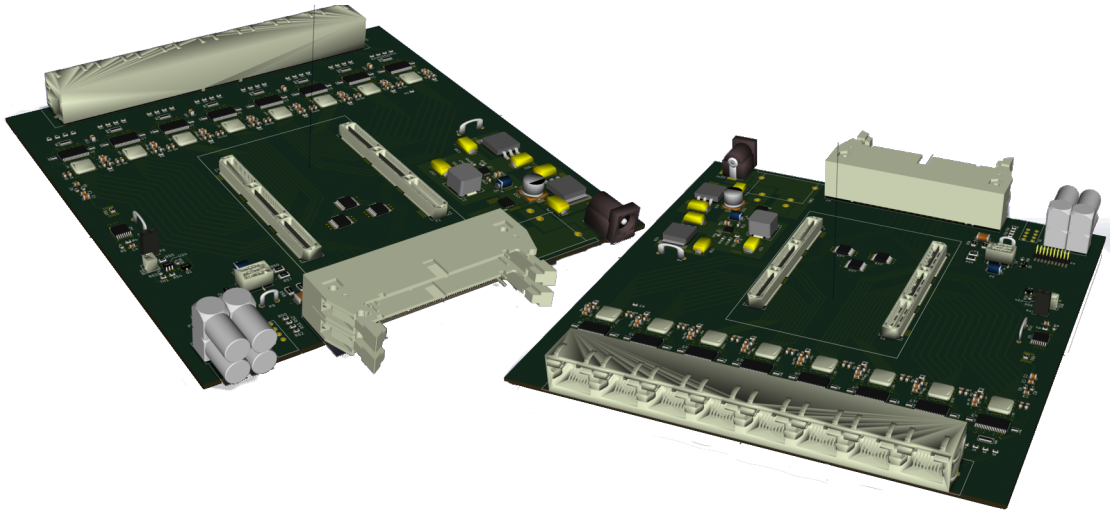

Figure 6.28: Front (left) and rear (right) 3D rendering of the Telescope DAQ. In the foreground of the front image are the LEMO connectors for supplying external clock and trigger as well as two programmable IO lines. The large center-front connector is a double 2x20 parallel port which is connected to matching connectors on the two backplane boards. Finally on the front right there is barrel jack for supplying power. The large connector in the foreground of the left image is an 8xRJ-45 jack for receiving the differential analog signals from the APC128 chips.

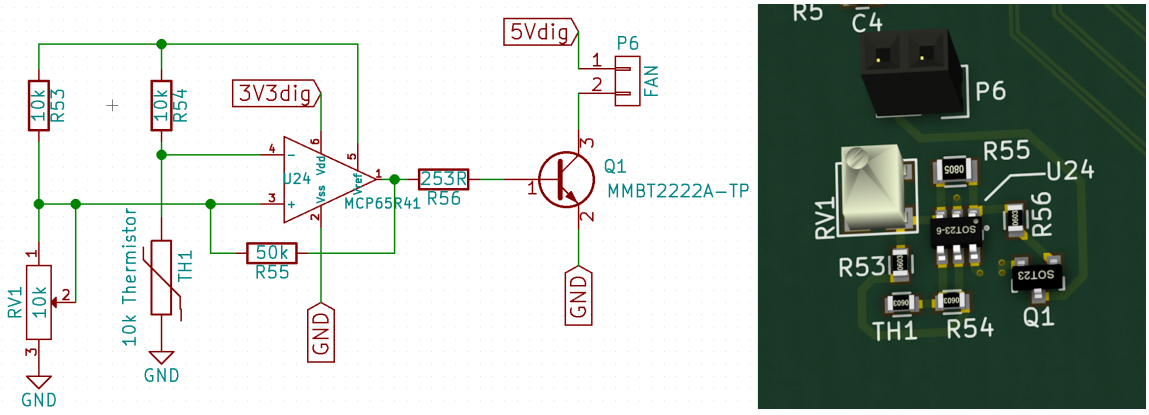

Figure 6.29: The fan control circuit. The FPGA, ADCs, and other electronics will potentially consume several watts of power. To allow for continuous operation within a case, it was decided to add a fan controller to the board. This would regulate the speed of a chassis mounted fan in accordance with a reading from a thermistor on the board.

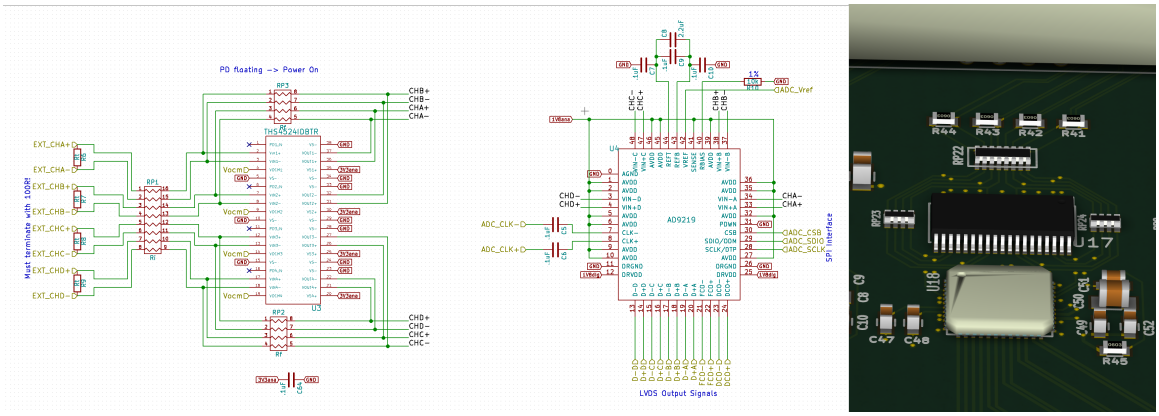

Figure 6.30: Single ADC assembly, capable of digitizing four APC128 signals. The design uses a Texas Instruments THS4524IDBTR four channel differential op amp to isolate the input lines from the ADC circuit and convert the differential signals to single-ended signal. This is paired with an Analog Devices AD9219 four-channel 10-bit ADC.

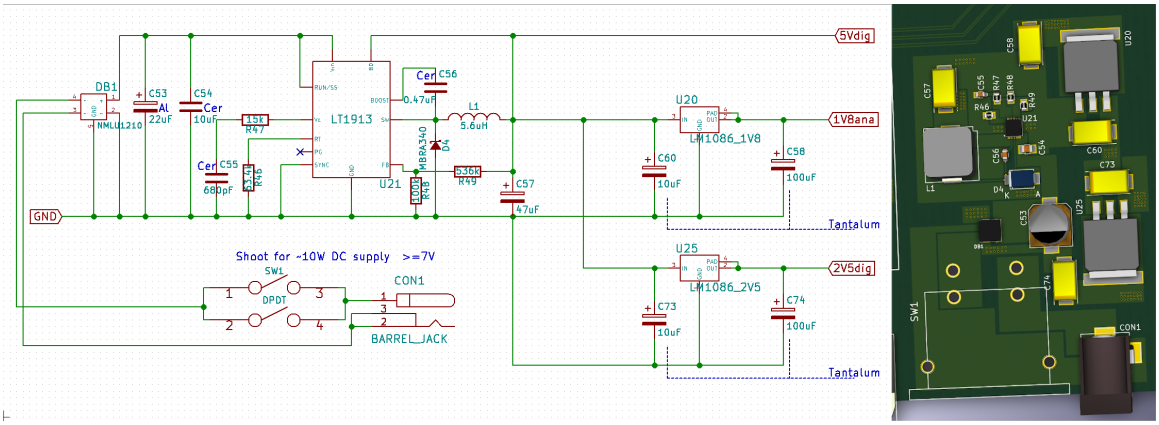

Figure 6.31: The power supply for the DAQ board. It uses a switching DC/DC converter to regulate a 7-25VDC supply down to 5V. It then employs two linear regulators to supply the 2.5V and 1.8V rails. There is a rocker switch (3D model missing) for turning the DAQ on and off, and a diode bridge between the plug and supply electronics to be tolerant to reverse polarity power sources.

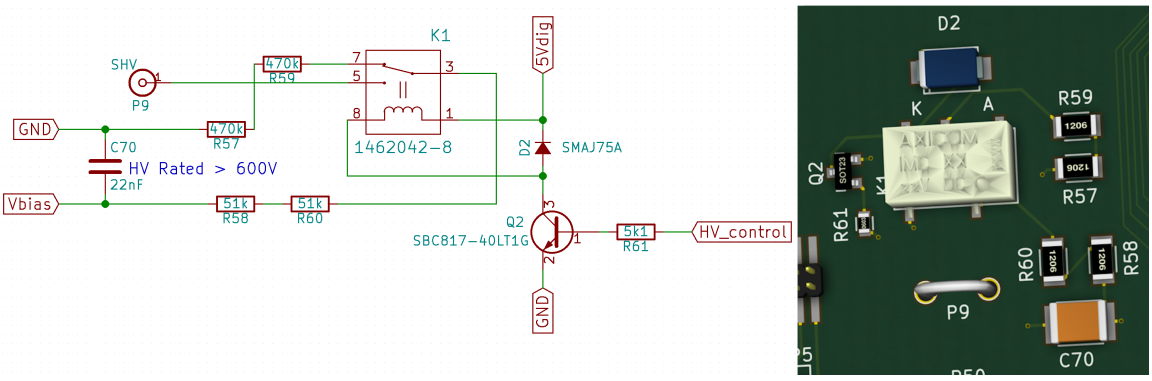

Figure 6.32: Bias voltage control. High voltage is supplied by an external source and connected to the board via a chassis mounted SHV connector. A mechanical relay, controled by a signal coming from the FPGA, controls whether bias voltage gets supplied to the micro-strip detectors. Large value serial resistors are used to limit any potential shock hazard.

choices for FPGA design: Verilog, and VHDL. There is also a "block diagram" visual style of programming that some IDEs support. For the DAQ software, Verilog was chosen due to its more "C-like" syntax over the more verbose VHDL. Fig. 6.33 shows a sample of some Verilog code.

Although one could, in principle, construct all of the necessary functionality of the DAQ firmware with Verilog logic circuits, it would be rather inflexible, requiring time-consuming recompilation and synthesis of the design upon any minor change. This motivates the need for "software" that can be loaded into the ZEM4310's RAM and then executed by logic on the FPGA. This is exactly what was done. A simple RISC (reduced instruction set computer) processor was implemented in Verilog. This processor implements a custom instruction set and uses memory mapped I/O to allow for access to the RAM, the ADCs, the lights on the RJ-45 connector, and so on. In this way, software could be developed that would orchestrate the operation of the DAQ. The software could also be changed on the fly during operation and testing by simply updating the content of a portion of the RAM and resetting the processor. An assembler was also written to convert human readable assembler code to the binary

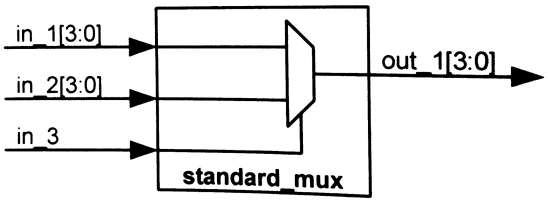


```
////////////////////////////////////////////////////
//
// Header information
// Standard Mux
//
////////////////////////////////////////////////////

module standard_mux
            (
               // Inputs
               in_1,
               in_2,
               in_3,
               // Outputs
               out_1,
            );

   // Port definitions

   input  [3:0]   in_1;
   input  [3:0]   in_2;
   input          in_3;

   output [3:0]   out_1;

   // ------------- Design implementation --------

   assign out_1 = in_3 ? in_2: in_1;

endmodule
```

Figure 6.33: A simple example of some Verilog code[97]. This shows how one may implement a 2-input 4-bit multiplexer. Note many of the C-like syntax features.

machine code used by the processor[98].

To facilitate communication between the FPGA and a connected computer, Opal Kelly provides a set of firmware blocks that can be incorporated into the FPGA design that interface with the USB3 controller to send and receive data from the host PC. Similarly, they have written PC software that couples to these signals and provides a simple programming interface in many popular programming languages, including Python. This interface will be used to develop the PC-side software to allow an operator to control the telescope.

6.4.4 Outlook

As of the time of this writing, the sensor layer cards, backplane board, and DAQ hardware[99] are finished. The DAQ firmware and software are developed as described in this document, however additional work is necessary to enable use in a test beam.

Chapter 7

Conclusions and Outlook

This thesis has covered many aspects of particle physics, starting from fundamental theories and detector design and operation through to the analysis of data collected with those detectors and measurement of a physical process. This measurement, in turn, will be used in the construction of more precise theories, and so the process will continue.

The measurement of the $t\bar{t}t\bar{t}$ cross section described here yielded the result of $12.6^{+5.8}_{-5.2}$ fb, in good agreement with the SM prediction of $12.0^{+2.2}_{-2.5}$ fb. This result allowed the author to set the limit on the top quarks Yukawa coupling of $y_t/y_t^{\mathrm{SM}} < 1.7$ as well as place limits on the masses of additional Higgs bosons in the framework of a Type-2 2HDM of 470(550) GeV/c^2 for the scalar(pseudoscalar) bosons.

In the future, this measurement will be conducted in the opposite-sign dilepton, single lepton, and fully hadronic decay modes of $t\bar{t}t\bar{t}$, and these results could potentially be combined with the same-sign dilepton result to yield a more precise measurement. It will also be improved in the future using data collected by the High Luminosity LHC (HL-LHC). Scheduled to begin operation in 2026, the HL-LHC is projected to deliver 3 ab^{-1} of integrated luminosity at $\sqrt{s} = 14$ TeV[100]. Projections using current analysis techniques to that energy and integrated luminosity predict that the four top cross section could be measured at roughly 20% accuracy. However, less than half of

this uncertainty is statistical, meaning that improved analysis techniques have the potential to increase the precision substantially.

The order of magnitude increase in instantaneous luminosity in the HL-LHC requires an upgraded detector. Lessons learned and tools developed during the Phase I upgrade are now being applied to the Phase II upgrade project where the UNL Silicon Lab is currently in collaboration with several other institutions to develop the manufacturing techniques that will be needed to reliably assemble modules for both the pixel detector and for a new detector for the Phase II upgrade, the timing detector. Both detectors will play a role in enabling physicists to study ever more closely the nature of the world around them.

Bibliography

[1] Wikimedia Commons. *Standard_Model_of_Elementary_Particle_dark.svg*. www.collegiate-advanced-electricity.com/single-post/2017/04/10/The-Standard-Model-of-Particle-Physics. June 2017.

[2] S. Tomonaga. "On a Relativistically Invariant Formulation of the Quantum Theory of Wave Fields". In: *Progress of Theoretical Physics* 1.2 (Aug. 1946), pp. 27–42. DOI: 10.1143/ptp.1.27. URL: https://doi.org/10.1143/ptp.1.27.

[3] Julian Schwinger. "Quantum Electrodynamics. I. A Covariant Formulation". In: *Physical Review* 74.10 (Nov. 1948), pp. 1439–1461. DOI: 10.1103/physrev.74.1439. URL: https://doi.org/10.1103/physrev.74.1439.

[4] R. P. Feynman. "Space-Time Approach to Quantum Electrodynamics". In: *Physical Review* 76.6 (Sept. 1949), pp. 769–789. DOI: 10.1103/physrev.76.769. URL: https://doi.org/10.1103/physrev.76.769.

[5] F. J. Dyson. "The Radiation Theories of Tomonaga, Schwinger, and Feynman". In: *Physical Review* 75.3 (Feb. 1949), pp. 486–502. DOI: 10.1103/physrev.75.486. URL: https://doi.org/10.1103/physrev.75.486.

[6] K.A. Olive. "Review of Particle Physics". In: *Chinese Physics C* 40.10 (Oct. 2016), p. 100001. DOI: 10.1088/1674-1137/40/10/100001. URL: https://doi.org/10.1088%2F1674-1137%2F40%2F10%2F100001.

[7] M. Gell-Mann. “A schematic model of baryons and mesons”. In: *Physics Letters* 8.3 (Feb. 1964), pp. 214–215. DOI: 10.1016/s0031-9163(64)92001-3. URL: https://doi.org/10.1016/s0031-9163(64)92001-3.

[8] G. Zweig. “An SU(3) model for strong interaction symmetry and its breaking. Version 2”. In: *Developments in the Quark Theory of Hadrons. Vol. 1. 1964 - 1978*. Ed. by D.B. Lichtenberg and Simon Peter Rosen. 1964, pp. 22–101.

[9] E. D. Bloom et al. “High-Energy Inelastic e-p Scattering at 6° and 10°”. In: *Physical Review Letters* 23.16 (Oct. 1969), pp. 930–934. DOI: 10.1103/physrevlett.23.930. URL: https://doi.org/10.1103/physrevlett.23.930.

[10] E. Fermi. “Versuch einer Theorie der β-Strahlen. I”. In: *Zeitschrift für Physik* 88.3-4 (Mar. 1934), pp. 161–177. DOI: 10.1007/bf01351864. URL: https://doi.org/10.1007/bf01351864.

[11] T. D. Lee and C. N. Yang. “Question of Parity Conservation in Weak Interactions”. In: *Physical Review* 104.1 (Oct. 1956), pp. 254–258. DOI: 10.1103/physrev.104.254. URL: https://doi.org/10.1103/physrev.104.254.

[12] C. S. Wu et al. “Experimental Test of Parity Conservation in Beta Decay”. In: *Physical Review* 105.4 (Feb. 1957), pp. 1413–1415. DOI: 10.1103/physrev.105.1413. URL: https://doi.org/10.1103/physrev.105.1413.

[13] Sheldon L. Glashow. “Partial-symmetries of weak interactions”. In: *Nuclear Physics* 22.4 (Feb. 1961), pp. 579–588. DOI: 10.1016/0029-5582(61)90469-2. URL: https://doi.org/10.1016/0029-5582(61)90469-2.

[14] A. Salam and J.C. Ward. “Electromagnetic and weak interactions”. In: *Physics Letters* 13.2 (Nov. 1964), pp. 168–171. DOI: 10.1016/0031-9163(64)90711-5. URL: https://doi.org/10.1016/0031-9163(64)90711-5.

[15] Steven Weinberg. “A Model of Leptons”. In: *Physical Review Letters* 19.21 (Nov. 1967), pp. 1264–1266. DOI: 10.1103/physrevlett.19.1264. URL: https://doi.org/10.1103/physrevlett.19.1264.

[16] H1 Collaboration. “Experimental observation of isolated large transverse energy electrons with associated missing energy at”. In: *Physics Letters B* 122.1 (Feb. 1983), pp. 103–116. DOI: 10.1016/0370-2693(83)91177-2. URL: https://doi.org/10.1016/0370-2693(83)91177-2.

[17] H2 Collaboration. “Observation of single isolated electrons of high transverse momentum in events with missing transverse energy at the CERN p collider”. In: *Physics Letters B* 122.5-6 (Mar. 1983), pp. 476–485. DOI: 10.1016/0370-2693(83)91605-2. URL: https://doi.org/10.1016/0370-2693(83)91605-2.

[18] M. Tanabashi et al. “Review of Particle Physics”. In: *Phys. Rev. D* 98.3 (Aug 2018), p. 030001. DOI: 10.1103/PhysRevD.98.030001. URL: %7Bhttps://link.aps.org/doi/10.1103/PhysRevD.98.030001%7D.

[19] I. Bigi et al. “Production and decay properties of ultra-heavy quarks”. In: *Physics Letters B* 181.1-2 (Nov. 1986), pp. 157–163. DOI: 10.1016/0370-2693(86)91275-x. URL: https://doi.org/10.1016/0370-2693(86)91275-x.

[20] H1 Collaboration. “Experimental observation of lepton pairs of invariant mass around 95 GeV/c2 at the CERN SPS collider”. In: *Physics Letters B* 126.5 (July 1983), pp. 398–410. DOI: 10.1016/0370-2693(83)90188-0. URL: https://doi.org/10.1016/0370-2693(83)90188-0.

[21] H2 Collaboration. “Evidence for Z0→e+e- at the CERN p collider”. In: *Physics Letters B* 129.1-2 (Sept. 1983), pp. 130–140. DOI: 10.1016/0370-2693(83)90744-x. URL: https://doi.org/10.1016/0370-2693(83)90744-x.

[22] Peter W. Higgs. "Broken Symmetries and the Masses of Gauge Bosons". In: *Physical Review Letters* 13.16 (Oct. 1964), pp. 508–509. DOI: 10.1103/physrevlett.13.508. URL: https://doi.org/10.1103/physrevlett.13.508.

[23] F. Englert and R. Brout. "Broken Symmetry and the Mass of Gauge Vector Mesons". In: *Physical Review Letters* 13.9 (Aug. 1964), pp. 321–323. DOI: 10.1103/physrevlett.13.321. URL: https://doi.org/10.1103/physrevlett.13.321.

[24] G. S. Guralnik, C. R. Hagen, and T. W. B. Kibble. "Global Conservation Laws and Massless Particles". In: *Physical Review Letters* 13.20 (Nov. 1964), pp. 585–587. DOI: 10.1103/physrevlett.13.585. URL: https://doi.org/10.1103/physrevlett.13.585.

[25] F. Bellaiche. *What's this Higgs boson anyway?* 2012. URL: https://www.quantum-bits.org/?p=233.

[26] CERN. "Interim Summary Report on the Analysis of the 19 September 2008 Incident at the LHC". In: *EDMS* (2008).

[27] The ATLAS Collaboration. "Observation of a new particle in the search for the Standard Model Higgs boson with the ATLAS detector at the LHC". In: (2012). DOI: 10.1016/j.physletb.2012.08.020. eprint: arXiv:1207.7214.

[28] The CMS Collaboration. "Observation of a new boson at a mass of 125 GeV with the CMS experiment at the LHC". In: (2012). DOI: 10.1016/j.physletb.2012.08.021. eprint: arXiv:1207.7235.

[29] Philippe Mouche. *Overall view of the LHC*. 2014.

[30] Fabienne Marcastel. *CERN's Accelerator Complex*. 2013.

[31] CERN Photographic Service. *Animation of CERN's accelerator network*. 2013. DOI: 10.17181.

[32] AC Collection. Legacy of AC. *Magnetic field induced by the LHC dipole's superconducting coils*. 2016.

[33] The CMS Collaboration. "CMS luminosity measurement for the 2018 data-taking period at $\sqrt{s} = 13$TeV". In: (2019).

[34] A Dominguez et al. *CMS Technical Design Report for the Pixel Detector Upgrade*. Tech. rep. CERN-LHCC-2012-016. CMS-TDR-11. Additional contacts: Jeffrey Spalding, Fermilab, Jeffrey.Spalding@cern.ch Didier Contardo, Universite Claude Bernard-Lyon I, didier.claude.contardo@cern.ch. Sept. 2012. URL: https://cds.cern.ch/record/1481838.

[35] The CMS Collaboration. "The CMS experiment at the CERN LHC". In: *JINST* 3 (2008).

[36] J. Fernandez. "The CMS silicon strip tracker". In: *Nuclear Instruments and Methods in Physics Research Section A: Accelerators, Spectrometers, Detectors and Associated Equipment* 573.1-2 (Apr. 2007), pp. 257–259. DOI: 10.1016/j.nima.2006.10.334. URL: https://doi.org/10.1016/j.nima.2006.10.334.

[37] The CMS Collaboration. "Description and performance of track and primary-vertex reconstruction with the CMS tracker". In: *Journal of Instrumentation* 9.10 (2014).

[38] CMS Collaboration and M Brice. "Images of the CMS Tracker Inner Barrel". CMS Collection. Nov. 2008. URL: https://cds.cern.ch/record/1431467.

[39] Bayatian, G L et al. *CMS Physics: Technical Design Report Volume 1: Detector Performance and Software*. Technical Design Report CMS. There is an error on cover due to a technical problem for some items. Geneva: CERN, 2006. URL: http://cds.cern.ch/record/922757.

[40] UC Davis Richard Breedon. "View through the CMS detector during the cooldown of the solenoid on February 2006". CMS Collection. Feb. 2006. URL: https://cds.cern.ch/record/930094.

[41] Jesus Puerta-Pelayo. "First DT+RPC chambers installation round in the UX5 cavern. Installation de chambres a muons dans la caverne UX5". CMS Collection. Jan. 2007. URL: https://cds.cern.ch/record/1019185.

[42] CMS Collaboration. *The Phase-2 Upgrade of the CMS Muon Detectors*. Tech. rep. CERN-LHCC-2017-012. CMS-TDR-016. This is the final version, approved by the LHCC. Geneva: CERN, Sept. 2017. URL: https://cds.cern.ch/record/2283189.

[43] X. Cid Vidal and R. Cid Manzano. *CMS Global Muon Trigger*. URL: https://www.lhc-closer.es/taking_a_closer_look_at_lhc/0.lhc_trigger.

[44] WLCG Project Offic3. *Documents and Reference - Tiers - Structure*. 2019. URL: http://wlcg.web.cern.ch/documents-reference.

[45] S. Agostinelli et al. "Geant4—a simulation toolkit". In: *Nuclear Instruments and Methods in Physics Research Section A: Accelerators, Spectrometers, Detectors and Associated Equipment* 506.3 (July 2003), pp. 250–303. DOI: 10.1016/s0168-9002(03)01368-8. URL: https://doi.org/10.1016/s0168-9002(03)01368-8.

[46] Arnulf Quadt. *Top Quark Physics at Hadron Colliders*. Springer Berlin Heidelberg, 2007. DOI: 10.1007/978-3-540-71060-8. URL: https://doi.org/10.1007/978-3-540-71060-8.

[47] A. M. Sirunyan et al. "Particle-flow reconstruction and global event description with the CMS detector". In: *JINST* 12 (2017), P10003. DOI: 10.1088/1748-0221/12/10/P10003. arXiv: 1706.04965 [physics.ins-det].

[48] P. Billoir and S. Qian. "Simultaneous pattern recognition and track fitting by the Kalman filtering method". In: *Nuclear Instruments and Methods in Physics Research Section A: Accelerators, Spectrometers, Detectors and Associated Equipment* 294.1-2 (Sept. 1990), pp. 219–228. DOI: 10.1016/0168-9002(90)91835-y. URL: https://doi.org/10.1016/0168-9002(90)91835-y.

[49] Matteo Cacciari, Gavin P Salam, and Gregory Soyez. "The anti-kt jet clustering algorithm". In: *Journal of High Energy Physics* 2008.04 (Apr. 2008), pp. 063–063. DOI: 10.1088/1126-6708/2008/04/063. URL: https://doi.org/10.1088/1126-6708/2008/04/063.

[50] CMS Collaboration. *Heavy flavor identification at CMS with deep neural networks*. CMS Detector Performance Summary CMS-DP-2017-005. 2017. URL: http://cds.cern.ch/record/2255736?ln=en.

[51] Rikkert Frederix, Davide Pagani, and Marco Zaro. "Large NLO corrections in $t\bar{t}W^{\pm}$ and $t\bar{t}t\bar{t}$ hadroproduction from supposedly subleading EW contributions". In: *Journal of High Energy Physics* 2018.2 (Feb. 2018). DOI: 10.1007/jhep02(2018)031. URL: https://doi.org/10.1007/jhep02(2018)031.

[52] The ATLAS Collaboration. "Search for new phenomena in events with same-charge leptons and b-jets in pp collisions at $\sqrt{s} = 13$ TeV with the ATLAS detector". In: *Journal of High Energy Physics* 2018.12 (Dec. 2018). DOI: 10.1007/jhep12(2018)039. URL: https://doi.org/10.1007/jhep12(2018)039.

[53] The ATLAS Collaboration. "Search for four-top-quark production in the single-lepton and opposite-sign dilepton final states in pp collisions at $\sqrt{s} = 13$TeV with the ATLAS detector". In: *Physical Review D* 99.5 (Mar. 2019). DOI: 10.1103/physrevd.99.052009. URL: https://doi.org/10.1103/physrevd.99.052009.

[54] The CMS Collaboration. "Search for physics beyond the standard model in events with two leptons of same sign, missing transverse momentum, and jets in proton-proton collisions at $\sqrt{s} = 13$ TeV". In: *The European Physical Journal C* 77.9 (Sept. 2017). DOI: 10.1140/epjc/s10052-017-5079-z. URL: https://doi.org/10.1140/epjc/s10052-017-5079-z.

[55] The CMS Collaboration. "Search for standard model production of four top quarks with same-sign and multilepton final states in proton–proton collisions at $\sqrt{s} = 13$ TeV". In: *The European Physical Journal C* 78.2 (Feb. 2018). DOI: 10.1140/epjc/s10052-018-5607-5. URL: https://doi.org/10.1140/epjc/s10052-018-5607-5.

[56] CMS Collaboration. *Search for the production of four top quarks in the single-lepton and opposite-sign dilepton final states in proton-proton collisions at $\sqrt{s} = 13$ TeV*. 2019. eprint: arXiv:1906.02805.

[57] "Search for production of four top quarks in final states with same-sign or multiple leptons in proton-proton collisions at $\sqrt{s} = 13$TeV". In: (2019).

[58] Albert M Sirunyan et al. "Measurements of $t\bar{t}$ cross sections in association with b jets and inclusive jets and their ratio using dilepton final states in pp collisions at $\sqrt{s} = 13$ TeV". In: *Phys. Lett. B* 776 (2018), p. 355. DOI: 10.1016/j.physletb.2017.11.043. arXiv: 1705.10141 [hep-ex].

[59] G. Zevi Della Porta. *Lepton ID for the full 2016 dataset*. https://indico.cern.ch/event/590228/contributions/2380031/attachments/1375541/2088587/EGMSUS_newIDs_17Nov16.pdf. Nov. 2016.

[60] P. Pigard. *Multivariate Electron ID in 8X*. https://indico.cern.ch/event/482674/contributions/2206032/attachments/1292177/1931287/20160621_EGM_cms_week_v5.pdf. June 2016.

[61] V. Hegde et al. *Electron MVA ID for SUSY*. https://indico.cern.ch/event/719317/contributions/2963816/attachments/1630110/2598062/MVAidSUSY_10Apr18_SUSYMeeting.pdf. Apr. 2017.

[62] Baffioni, S. and others. "Electron Charge Identification using 8 TeV data". In: *CMS Physics Analysis Note* AN-2014/164 (2015). URL: http://cms.cern.ch/iCMS/jsp/openfile.jsp?tp=draft&files=AN2014_164_v3.pdf.

[63] G. Abbiendi et al. *Baseline muon selections*. Oct. 2014. URL: https://twiki.cern.ch/twiki/bin/view/CMSPublic/SWGuideMuonId#Tight_Muon.

[64] G. Petrucciani and C. Botta. *Two step prompt muon identification*. Jan. 2015. URL: https://indico.cern.ch/event/368007/contribution/2/material/slides/0.pdf.

[65] RA5 group. "Search for SUSY in same-sign dilepton events at 13 TeV". In: *CMS Physics Analysis Note* AN-2015/031 (2016). URL: http://cms.cern.ch/iCMS/jsp/openfile.jsp?tp=draft%5C&files=AN2015_031_v10.pdf.

[66] Keith Rehermann and Brock Tweedie. "Efficient Identification of Boosted Semileptonic Top Quarks at the LHC". In: (2010). DOI: 10.1007/JHEP03(2011)059. eprint: arXiv:1007.2221.

[67] RA5 Group. "Search for SUSY in same-sign dilepton events at 13 TeV". In: AN-2015/031 (2016). URL: http://cms.cern.ch/iCMS/jsp/openfile.jsp?tp=draft&files=AN2015_031_v10.pdf.

[68] D. Ferencek et al. *b-Tagging Offline Guide*. https://twiki.cern.ch/twiki/bin/view/CMSPublic/SWGuideBTagging. Nov. 2014.

[69] Vardan Khachatryan et al. "Performance of the CMS missing transverse momentum reconstruction in pp data at $\sqrt{s} = 8$ TeV". In: *JINST* 10 (2015), P02006. DOI: 10.1088/1748-0221/10/02/P02006. arXiv: 1411.0511 [physics.ins-det].

[70] I. Antcheva et al. "ROOT - A C++ framework for petabyte data storage, statistical analysis and visualization". In: *Computer Physics Communications* 180.12 (Dec. 2009), pp. 2499–2512. DOI: 10.1016/j.cpc.2009.08.005. URL: https://doi.org/10.1016/j.cpc.2009.08.005.

[71] Tianqi Chen and Carlos Guestrin. "XGBoost: A Scalable Tree Boosting System". In: *Proceedings of the 22Nd ACM SIGKDD International Conference on Knowledge Discovery and Data Mining*. KDD '16. San Francisco, California, USA: ACM, 2016, pp. 785–794. ISBN: 978-1-4503-4232-2. DOI: 10.1145/2939672.2939785. URL: http://doi.acm.org/10.1145/2939672.2939785.

[72] Georgios Konstantinos Krintiras. *Associated production of top quarks with the Higgs boson at* $\sqrt{s} = 13$ *TeV*. 2017. eprint: arXiv:1712.06104.

[73] CMS SUSY fake-leptons working group. "Studies of methods to estimate the non-prompt lepton background to searches for new physics". In: *CMS Physics Analysis Note* AN-2014/261 (2015). URL: http://cms.cern.ch/iCMS/jsp/openfile.jsp?tp=draft&files=AN2014_261_v2.pdf.

[74] CMS Collaboration. *Public CMS Luminosity Information*. 2019. URL: https://twiki.cern.ch/twiki/bin/view/CMSPublic/LumiPublicResults.

[75] CMS Collaboration. "Jet energy scale and resolution in the CMS experiment in pp collisions at 8 TeV". In: (2016). DOI: 10.1088/1748-0221/12/02/P02014. eprint: arXiv:1607.03663.

[76] SUSY Lepton Scale Factor team. *Lepton Scale Factors*. https://twiki.cern.ch/twiki/bin/view/CMS/SUSLeptonSF. July 2016.

[77] Roger Barlow and Christine Beeston. "Fitting using finite Monte Carlo samples". In: *Computer Physics Communications* 77.2 (1993), pp. 219–228. ISSN: 0010-4655. DOI: https://doi.org/10.1016/0010-4655(93)90005-W. URL: http://www.sciencedirect.com/science/article/pii/001046559390005W.

[78] *The Higgs Combine Analysis Tool*. https://twiki.cern.ch/twiki/bin/view/CMS/SWGuideHiggsAnalysisCombinedLimit.

[79] Thomas Junk. "Confidence level computation for combining searches with small statistics". In: *Nuclear Instruments and Methods in Physics Research Section A: Accelerators, Spectrometers, Detectors and Associated Equipment* 434.2-3 (Sept. 1999), pp. 435–443. DOI: 10.1016/s0168-9002(99)00498-2. URL: https://doi.org/10.1016/s0168-9002(99)00498-2.

[80] A L Read. "Presentation of search results: theCLstechnique". In: *Journal of Physics G: Nuclear and Particle Physics* 28.10 (Sept. 2002), pp. 2693–2704. DOI: 10.1088/0954-3899/28/10/313. URL: https://doi.org/10.1088/0954-3899/28/10/313.

[81] Glen Cowan et al. "Asymptotic formulae for likelihood-based tests of new physics". In: *The European Physical Journal C* 71.2 (Feb. 2011). DOI: 10.1140/epjc/s10052-011-1554-0. URL: https://doi.org/10.1140/epjc/s10052-011-1554-0.

[82] Qing-Hong Cao, Shao-Long Chen, and Yandong Liu. "Probing Higgs width and top quark Yukawa coupling from $t\bar{t}H$ and $t\bar{t}t\bar{t}$ productions". In: *Phys. Rev. D* 95 (2017), p. 053004. DOI: 10.1103/PhysRevD.95.053004. arXiv: 1602.01934 [hep-ph].

[83] K. J. F. Gaemers and F. Hoogeveen. "Higgs production and decay into heavy flavors with the gluon fusion mechanism". In: *Phys. Lett. B* 146 (1984), p. 347. DOI: 10.1016/0370-2693(84)91711-8.

[84] G. C. Branco et al. “Theory and phenomenology of two-Higgs-doublet models”. In: *Phys. Rept.* 516 (2012), p. 1. DOI: 10.1016/j.physrep.2012.02.002. arXiv: 1106.0034 [hep-ph].

[85] Nathaniel Craig et al. “Heavy Higgs bosons at low $\tan\beta$: from the LHC to 100 TeV”. In: *JHEP* 01 (2017), p. 018. DOI: 10.1007/JHEP01(2017)018. arXiv: 1605.08744 [hep-ph].

[86] David Aaron Matzner Dominguez et al. “CMS Technical Design Report for the Pixel Detector Upgrade”. In: (2012). DOI: 10.2172/1151650.

[87] *UNL Phase I FPIX Assembly Standard Operating Procedures*. 2016. URL: https://github.com/psi46/unl-sop.

[88] *Gantry Control Software*. 2019. URL: https://github.com/CUASAS/pixel-gantry-control.

[89] *Gantry Fiducial Recognition Software*. 2019. URL: https://github.com/CUASAS/pixel-gantry-vision.

[90] G. Bradski. “The OpenCV Library”. In: *Dr. Dobb’s Journal of Software Tools* (2000).

[91] Anastasia Tegopoulou and Evangelos Papadopoulos. “Determination of Rigid-Body Pose from Imprecise Point Position Measurements”. In: *IEEE/RSJ International Conference on Intelligent Robots and Systems*. 2011.

[92] Berthold K. P. Horn. “Closed-form solution of absolute orientation using unit quaternions”. In: *J. Opt. Soc. Am. A* 4 (1987).

[93] Roland Horisberger and Michael Hilgers. “Development of a radiation hard version of the Analog Pipeline Chip APC128”. In: *Nuclear Instruments and Methods in Physics Research* (Apr. 2002), pp. 556–565.

[94] *APC128 Testboard Designs*. 2016. URL: https://github.com/cfangmeier/VFPIX-telescope-PCB/tree/master/APC128testboard.

[95] *APC128 Pattern Generrator*. 2016. URL: https://github.com/cfangmeier/VFPIX-telescope-Code/tree/master/utils/PatternGen.

[96] Adrian Ryser. "Semesterarbeit - Pixel Telescope". 2013.

[97] Blaine C. Readler. *Verilog by Example*. Full Arc Press, 2011.

[98] *Phase II Telescope Software*. 2016. URL: https://github.com/cfangmeier/VFPIX-telescope-Code.

[99] *Phase II Telescope Hardware Designs*. 2016. URL: https://github.com/cfangmeier/VFPIX-telescope-PCB.

[100] P. Azzi et al. *Standard Model Physics at the HL-LHC and HE-LHC*. 2019. eprint: arXiv:1902.04070.